



HAL
open science

Penalty methods for the simulation of fluid-solid interactions with various assemblies of resolved scale particles

Mohamed-Amine Chadil

► **To cite this version:**

Mohamed-Amine Chadil. Penalty methods for the simulation of fluid-solid interactions with various assemblies of resolved scale particles. Mechanics [physics]. Université de Bordeaux, 2018. English. NNT : 2018BORD0205 . tel-01968078

HAL Id: tel-01968078

<https://theses.hal.science/tel-01968078>

Submitted on 2 Jan 2019

HAL is a multi-disciplinary open access archive for the deposit and dissemination of scientific research documents, whether they are published or not. The documents may come from teaching and research institutions in France or abroad, or from public or private research centers.

L'archive ouverte pluridisciplinaire **HAL**, est destinée au dépôt et à la diffusion de documents scientifiques de niveau recherche, publiés ou non, émanant des établissements d'enseignement et de recherche français ou étrangers, des laboratoires publics ou privés.

THÈSE PRÉSENTÉE
POUR OBTENIR LE GRADE DE

**DOCTEUR DE
L'UNIVERSITÉ DE BORDEAUX**

ÉCOLE DOCTORALE DES SCIENCES PHYSIQUES ET DE L'INGÉNIEUR

SPÉCIALITÉ : MÉCANIQUE

par

Mohamed-Amine CHADIL

**Penalty methods for the simulation of fluid-solid interactions with
various assemblies of resolved scale particles**

Sous la direction de : Mejdî AZAIEZ
(co-directeurs : Stéphane VINCENT et Jean-Luc ESTIVALEZES)

Soutenue le 30 Octobre 2018

Membres du jury :

M. MASBERNAT, Olivier	Directeur de recherche, CNRS	Président
M. SIMONIN, Olivier	Professeur, INP Toulouse	Rapporteur
M. ANGOT, Philippe	Professeur, Aix-Marseille Université	Rapporteur
M. AZAIEZ, Mejdî	Professeur, Université de Bordeaux	Directeur
M. VINCENT, Stéphane	Professeur, Université Paris-Est UPEM	Co-directeur
M. ESTIVALEZES, Jean-Luc	Professeur, INP Toulouse	Co-directeur
M. FEDE, Pascal	Maître de conférences, UPS Toulouse	Invité

Méthodes de pénalisation pour la simulation des interactions fluide-solide avec des réseaux variés de particules résolues.

Résumé : Les simulations des écoulements diphasiques particulières à l'échelle réelle de l'application nécessitent des modèles pour les termes non fermés des équations macroscopiques. Des simulations numériques directes de particules résolues utilisant la méthode de pénalisation visqueuse ont été réalisées afin de mesurer les interactions entre des particules de différentes formes (sphérique et ellipsoïdale) et le fluide porteur à différents régimes d'écoulement (de stokes à l'inertiel). Deux méthodes ont été développées durant cette thèse afin d'extraire les forces hydrodynamiques ainsi que les transferts de chaleur sur les frontières immergées représentant les particules. Plusieurs validations ont été conduites pour différentes configurations de particules : de la simulation d'une particule isolée à un réseau aléatoire de sphères en passant par un réseau cubique face centrée de sphères. Une corrélation du nombre de Nusselt est proposée pour un sphéroïde allongé plongé dans un écoulement uniforme.

Mots clés : [Ecoulement diphasique, Modélisation numérique, Particules résolues, Forces hydrodynamiques, Transfert de chaleur, Particules non-sphériques]

Penalty methods for the simulation of fluid-solid interactions with various assemblies of resolved scale particles

Abstract : The simulations of multiphase flows at real application scale need models for unclosed terms in macroscopic equations. Particle-Resolved Direct Numerical Simulations using Viscous Penalty Method have been carried out to quantify the interactions between particles of different shapes (spheres, ellipsoids) and the carrier fluid at different regimes (from Stokes to inertial). Two methods have been developed to extract hydrodynamic forces and heat transfers on immersed boundaries representing the particles. Validations have been conducted for various configuration of particles: from an isolated sphere and spheroid to Face-Centered Cubic to a random arrangement of spheres. A correlation of the Nusselt number for an isolated prolate spheroid past by a uniform flow is proposed.

Keywords : [Multiphase flow, Numerical modeling, Particle-Resolved DNS, Hydrodynamic forces, Heat transfer, Non-spherical particles]

Unité de recherche

[Institut de Mécanique et d'Ingénierie de Bordeaux - UMR 5295 I2M - 16 avenue Pey-Berland, 33607 Pessac Cedex, France]

Remerciements

Je voudrais tout d'abord remercier mes directeurs de thèse Stéphane Vincent et Jean-Luc Estivalezes pour cette opportunité et leur soutien durant cette thèse.

Merci aux membres du jury d'avoir accepté d'examiner ce travail.

Je voudrais également remercier Eric Climent, directeur de l'Institut de Mécanique des Fluides de Toulouse où j'ai effectué ce travail, pour son accueil et son soutien.

Au même titre je voudrais remercier Thierry Poinot, responsable du groupe Particle Spray and Combustion (PSC), auquel j'ai appartenu ainsi que tout le staff administratif et technique de l'IMFT.

Un grand merci aux membres de ma famille, aux amis et aux collègues qui m'ont soutenu durant ces années.

Je tiens à remercier chaleureusement Stéphane Vincent pour son aide durant ces semaines de rédaction sans laquelle je n'aurais jamais pu aller au bout de ce travail.

À Diane, Mohamed-Mehdi, Philip et Claudie.

Contents

1	Introduction	1
2	Improvement of the Viscous Penalty Method for particle-resolved simulations	7
2.1	Introduction	7
2.2	Model and numerical methods	8
2.3	Uniform Stokes flow past a cylinder	15
2.4	Uniform flow past a square configuration of cylinders	26
2.5	Conclusions and Suggestions	29
3	Accurate estimate of drag forces using particle-resolved direct numerical simulations	31
3.1	Introduction	31
3.2	Model and numerical methods	34
3.2.1	Fictitious domain approach	34
3.2.2	Penalty methods	35
3.2.3	Discretization schemes and solvers	37
3.3	Lagrangian extrapolation of forces for immersed boundary methods .	37
3.3.1	Low order naive approach	38
3.3.2	New high order method based on Lagrange extrapolation . .	41
3.4	Validation on flows interacting with an isolated particle	43
3.4.1	Drag coefficient	43
3.4.2	Simulations setup	43
3.4.3	Study of numerical parameters for the Lagrange extrapolation	44
3.4.4	Result on the drag coefficient	46
3.4.5	Pressure coefficient	46
3.5	Forces in fixed arrangements of spheres	48
3.5.1	Monodispersed arrangements of spheres	49
3.5.2	Bidisperse arrangements of spheres	57
3.6	Conclusions and perspectives	58
3.7	Appendix 1: Taylor Interpolation	60
4	Accurate calculation of heat transfer coefficients for motions around particles with a finite-size particle approach	67
4.1	Introduction	67
4.2	Numerical Methodology	69

4.3	Convective heat transfer forced by a uniform flow around a stationary sphere	71
4.4	Face-Centered Cubic periodic arrangement of spheres	74
4.5	Finite size random arrangement of spheres in a channel	77
4.6	Conclusion	80
5	Drag, lift and Nusselt coefficients for ellipsoidal particles using particle-resolved direct numerical simulations	81
5.1	Introduction	81
5.2	Numerical Methodology	83
5.3	Drag, Lift and Nusselt for an isolated stationary ellipsoid past by a uniform flow	86
5.4	Conclusion	91
6	Novel method to compute drag force and heat transfer for motions around spheres	93
6.1	Introduction	93
6.2	Numerical Methodology	95
6.2.1	Conservation equations	95
6.2.2	Fictitious domain approach and viscous penalty method	95
6.2.3	Drag force and heat flux computation using Aslam extension	95
6.3	Isolated stationary sphere past by a uniform flow	105
6.3.1	Drag force computation	106
6.3.2	Heat transfer computation	112
6.4	Face-Centered Cubic arrangement of stationary sphere past by a uniform flow	114
6.4.1	Monodispersed Face-Centred Cubic periodic arrangement of spheres	115
6.5	Conclusions	118
7	Conclusions and perspectives	121
	Bibliography	125

Chapter 1

Introduction

Multiphase flows involving solid particles interacting with a carrier fluid are part of a very active research area. Indeed, they are widely encountered in nature, for instance in volcanic eruptions [10, 33], sand storms or beach erosion under wave impact. They also occur in many industrial processes such as pneumatic conveying systems as well as fluidized beds [77, 109], gas phase polymerization reactors [46], chemical looping combustion [2, 67, 71, 117], fluid catalytic cracking reactors [3], oil refining and blast furnaces, to name a few.

The achievement and improvements of these industrial applications depends on the engineers ability to determine their best designs by using simulations of particulate flow (limited in this work to fluid-solid flows) in industrial devices. This kind of simulations are also used to understand the environmental phenomena where they took place in order to better prevent their impacts. These simulations, conducted at the application scale, are based on statistical approaches for both the fluid-particle interactions and the continuous phase. This is due to the huge disparity of scales between the particle size and the process scale (for the fluid-particle interactions), and between the smallest and largest eddy scales in the continuous phase at high Reynolds numbers.

Continuous phase modeling

Direct Numerical Simulations (DNS) is the most accurate method to simulate the continuous phase as it resolve the finest details of the flow in space and time. However, at high Reynolds numbers, two constraints make this approach very expensive in CPU time and memory, leading to a limited possible investigation of the approach. On one hand, the Eulerian mesh has to be fine enough to resolve even the smallest velocity and pressure oscillations and capture the energy dissipating eddies. On the other hand, the domain size has to be large enough to account for the larger scale structures of the flow. Thus, other approaches are adopted at high Reynolds number: Large Eddy Simulation (LES) is considered when only large scale vortices are needed to be resolved, while the small eddies are filtered out and energy dissipation occurring at this eddy scale is approximated by sub-grid mod-

els. The second methodology belongs to Reynolds Averaged Navier-Stokes (RANS) models. It is more often used for general purposes, as it gives an average solution of the flow and the fluctuations flow contribution are modeled by semi-empirical laws ($k-\epsilon$...). This method is still less expensive than DNS or even LES since a coarser mesh and larger time-steps can be utilized even if the need of semi-empirical models introduces additional equations to solve and more empiricism in the modeling.

Note that, in the case of particulate flows, the Reynolds number is often moderate ($Re < 300$), therefore direct numerical simulations are used to resolve the fluid especially for dense flows where the collisions are dominant.

Fluid-Particles interactions modeling

Depending on the solid volume fraction α_d *i.e.* the proportion of the solid phase in the mixture, two approaches exist to simulate particulate flows abroad the microscale:

- Eulerian-Lagrangian (EL) approach (for $\alpha_d < 0.1$): in this method each particle is treated individually, which requires computation of both particle-particle and particle-fluid interaction for every body immersed in the flow. Moreover, the motion of every particle has to be calculated separately.
- Eulerian-Eulerian (EE) approach (for $\alpha_d > 0.1$): unlike Eulerian-Lagrangian approaches, the particles in this method are not treated individually but are considered as a continuous phase inter-penetrating with the carrier fluid. Therefore, two Navier-Stokes equations (one for the fluid and one for the averaged particles), linked by the volume fraction, are solved.

Both approaches are based on an important assumption: the scale separation between the size of the particles (the radius R_p for spherical particles) and the size of the problem at the macroscopic scale or more precisely, the size of the cell mesh Δx . To be valid, $R_p \ll \Delta x$. Both models (EL and EE) do also require the knowledge of constitutive laws for drag, lift, torque, collisions or heat transfers to close specific particle-fluid interaction terms. Famous correlations do exist for monodispersed spherical particles: Schiller and Naumann [97] for drag force and Ranz and Marshall [88] for heat transfer used in EL method when the solid volume fraction is very low. Moreover, Ergun [42] and Wen & Yu [114] are used for drag force as well as Gunn [47] for heat transfer. However, the particles in most applications are non-spherical and polydispersed. Therefore, new drag and lift laws as well as Nusselt correlations have to be designed. This will be the main contribution of our particle-resolved DNS modeling, which is detailed in the next sections: allowing to simulate new particle arrangements or shapes in order to provide new drag, lift or Nusselt correlations, that could be used in larger scale EE or EL models.

Theoretical and experimental approaches have been widely investigated to model the unclosed terms representing the average interphase transfer of momentum and

energy between the fluid and the particles. However, these approaches have shown significant limitations: on one hand, theoretical results are limited to Stokes or moderate Reynolds number regimes [1, 81]. On the other hand, experimental measurements showed huge differences of Nusselt number at high volume fraction because of limited optical access [112]. This motivates the community to consider and develop Particle-Resolved Direct Numerical Simulations (PR-DNS) to directly compute the fluid-particle interaction and the associated heat transfer closure laws.

Particle-Resolved Direct Numerical Simulations (PR-DNS)

In the framework of finite-size particle motions, many numerical approaches have been developed to perform PR-DNS of fluid-solid flows. These can be classified on one hand by those that rely on an unstructured body-fitted mesh to simulate the fluid area in the two-phase flow and impose boundary conditions at particles surfaces [29, 56, 57, 72, 98]. However, building such a finite-volume or finite-element mesh in three-dimensions is not easy and requires automatic remeshing as the solid particles move according to time and space. Moreover, the remeshing process at each calculation step is time consuming [62] and can be very difficult to manage automatically in computer softwares when the global shape of the fluid-solid interface is changing at each calculation step [40].

On the other hand, there exist those approaches called Fictitious domain methods [60, 78] that employ a fixed Cartesian grid in the whole domain. With these methods, the mesh is not adapted to the fluid-solid interfaces and includes both phases. Thus, on a mesh point of view, this approach is simpler than the previous one but difficulty lies in taking into account the presence of particles as interface is not explicitly tracked by the mesh that does not conform to the fluid/particle interface. To overcome this problem, a phase function is introduced to locate each phase.

Among the wide variety of fictitious domain approaches, *i.e.* particles are treated as immersed interfaces on a fixed mesh, we can cite the Distributed Lagrangian Method (DLM) of Glowinski and co-workers [78, 79], the Physalis technique of Prosperetti and co-workers [83, 101, 118], the Immersed Interface Method of Li and Lai [66] and the most used among them detailed hereafter:

Immersed Boundary Method (IBM)

The immersed boundary method consists in adding to the Navier-Stokes equation a forcing term to impose a solid behaviour at the particle surface. This method was initially developed by Peskin [80] where the forcing was deduced from the force applied on the particle. Due to instabilities, Ulmann [105] improved it by deducing the forcing term in Navier-Stokes equation from the desired velocity at the particle surface. Although this method has proven its efficiency for handling finite-size particle simulations [36, 102, 105, 106, 113, 116], the forcing on the particle surface

contaminate the fluid area near the interface, which makes hydrodynamic force or heat transfer computation on the surface not straightforward. To overcome this issue, Tenneti *et al.* [103] proposed a new technique called PUREIBM where the forcing term is restricted to the Eulerian grid points that lie in the particle, ensuring that the flow solution in the fluid phase is uncontaminated by the forcing. It is worth noting that an immersed boundary method can be implemented in any CFD code without any need to modify the underlying solver. Moreover, the use of particle meshes representing their body shape to impose the desired velocity makes this method very efficient regardless of the particle shapes and then allows the study of flows past complex particle shapes.

Lattice Boltzmann Method (LBM)

Contrary to the methods based on classical Navier-Stokes approaches which are using macroscopic values, LBM is based on Boltzmann equation with mesoscopic values resolved on a discrete system of fictitious fluid called “particles” (not to be confused with solid bodies immersed in the fluid). These fluid “particles” moves with discrete steps and collides with each others according to specific rules. This method is also very popular [12, 51, 53, 64, 65] as it is very efficient and easy to implement in parallel. In LBM, specific techniques are implemented to account for immersed particles such as bounce back or IBM type methods.

Viscous Penalty Method

This method was originally proposed by Ritz and Caltagirone [91] and improved by Vincent *et al.* [20, 109] to what is called Implicit Tensorial Penalty Method (ITPM). It consists in resolving Navier-Stokes equations in the whole domain and imposing by means of a phase function a large value of viscosity in the Eulerian cells belonging to the dispersed phase. This ensures a solid behavior in the particles [108, 109, 110]. This is the method utilized in this work. It is fully detailed in the next chapter 2. The penalty modeling strategy developed hereafter is based on this approach and will be reported in the next section. The main reason why we choose to use the ITPM instead of IBM for example is that ITPM is fully implicit and compatible with the pressure-velocity treatment that we considered, called augmented Lagrangian method. Another important motivation in investigating particle-resolved simulations with ITPM is that this approach is very robust and allows for handling particle flows at any kind of density ratios or solid fractions [34, 35, 77, 85, 86, 109].

Thesis outline

This work aims at providing a reliable tool to investigate and ultimately model the particle-fluid interactions in the framework of finite-size particle motions. This manuscript describes the different methods implemented during this research work as well as the numerical simulations carried out in this study. It is organized as

follows:

- The second chapter 2 presents the Viscous Penalty Method and details some of its main features. A new method to compute the solid phase function C_μ located at the off-diagonal viscosity coefficients is proposed. A numerical study of the parameters controlling the viscous penalty method is investigated using a uniform Stokes flow past a cylinder, to better set up the Particle-Resolved Direct Numerical Simulations parameters. Moreover, the viscous penalty method set up with the new numerical parameters is validated at higher Reynolds number using the uniform flow past a square configuration of cylinders, where its friction factor is calculated with our particle-resolved simulation approach and compared to Ergun correlation [42] for various solid volume fractions.
- The third chapter 3 presents a new force calculation method based on a third order Lagrange extrapolation coupled with a a third order Taylor interpolation for immersed interfaces. This aspect is very important to extract accurate physics from PR-DNS simulations. The way the drag, lift or Nusselt coefficients are obtained thanks to fictitious domains methods is rarely explained in the literature. This aspect of the PhD is one of the major contributions in terms of numerical developments. This chapter also discusses the order of approximations and associated accuracy of the force calculation method. Validations for flows interacting with isolated spherical particles at various Reynolds numbers are presented as well as simulations and validations of flows through fixed Faced-Centered Cubic arrangement of mono- and bi-dispersed spheres as well as fixed random arrangements of mono-dispersed spheres.
- The fourth chapter 4 is dedicated to the heat transfer computation using the same method as in the second chapter 3 *i.e.* a third order Lagrange extrapolation coupled with a third order Taylor interpolation. Validations of this method are presented for flows interacting with isolated spherical particles at various Reynolds number. Moreover, simulations of a uniform flow past a Face-Centered cubic array of spheres are discussed as well as flows through random arrangements of mono-dispersed spheres.
- The fifth chapter 5 is devoted to ellipsoidal particle. In a first part, a brief description is given for the phase functions (C and C_μ) computation with ellipsoidal particles. The extension of the force and heat transfer calculation to ellipsoidal particles is briefly recalled. Thereafter, estimation of drag, lift and Nusselt for uniform flows around an isolated ellipsoidal particle is presented. Comparisons to existing correlations of the literature are investigated and a new Nusselt correlation is considered for various Reynolds and attack angles.
- The sixth chapter 6 introduces an original method to compute forces and heat transfer based on Aslam extension rather than Lagrange extrapolation used up to now. Thereafter, Aslam extension numerical parameters are detailed and validated. Estimated drag and Nusselt coefficient for uniform flows around

an isolated sphere are compared to those given by Lagrange extrapolation in order to assess the improvements brought by Aslam extension. The same study is presented for flows through fixed arrangements of mono- and bi-dispersed spheres.

- The seventh chapter 7 summarizes general conclusions and discusses perspectives of future works.

Chapter 2

Improvement of the Viscous Penalty Method for particle-resolved simulations

This chapter is the article [26] authored by M.-A. Chadil, S. Vincent and J.-L. Estivalezes

Abstract

A numerical study of the parameters controlling the viscous penalty method is investigated to better set up Particle-Resolved Direct Numerical Simulations (PR-DNS) of particulate flows. Based on this analysis, improvements of the methods are proposed in order to reach an almost second order convergence in space. The viscous penalty method is validated in Stokes regime by simulating a uniform flow past a fixed isolated cylinder. Moreover, it is also utilized in moderate Reynolds number regime for a uniform flow past a square configuration of cylinder and compared in terms of friction factor to the well-known Ergun correlation.

2.1 Introduction

The motion of rigid particles interacting with a carrier fluid is a very active research area that is commonly found in the fields of environment and industrial processes. Among them, we can cite fluidized beds and chemical engineering, material manufacturing and design, sand dynamics, beach erosion under wave impact or nano-particle impact on human health. The simulation of such real problems is based on the use of Eulerian-Eulerian or Eulerian-Lagrangian models that require knowledge of constitutive laws for drag, lift, torque, collisions or heat transfers for the fluid-particle interactions. One way of designing these laws or validating them is to use resolved-scale particle approaches, in which all scales associated with the fluid flow and the hydrodynamic forces on the particle are directly simulated, unlike in point-particle or Eulerian-Eulerian approaches where drag and lift correlations are required *a priori* to simulate the problem.

The numerical simulation of resolved-scale particle motion is a highly developed field of research mainly based on fixed structured grids, as unstructured meshes adapted to the particle motion are difficult to design in three dimensions and CPU time consuming [62]. Among the wide variety of fictitious domain approaches, *i.e.* particles are treated as immersed interfaces on a fixed mesh, we can cite the numerical methods based on Lattice Boltzmann models [12, 51, 53, 64, 65] and the approaches that uses the Navier-Stokes equations, such as the Immersed Boundary Method (IBM) of Uhlmann [105, 106], the PUnRe-IBM approach of Tenneti *et al.* [103], the Distributed Lagrangian Method (DLM) of Glowinski and co-workers [78, 79] and the Implicit Tensorial Penalty Method (ITPM) of Vincent *et al.* [20, 109], also called viscous penalty method.

In the present work, we choose to investigate viscous penalty methods on fixed Cartesian grids for fixed particles. Compared to other fictitious domains techniques, the main interest of penalty methods is to rely on fully coupled velocity solving with incompressible and solid constraints satisfaction instantly, thanks to an augmented Lagrangian method for the fluid and viscous penalty for the solid phase. Our main goal is first to characterize the accuracy and convergence order of the ITPM method on reference particle motion test cases but also to improve the numerical method and the setting of numerical penalty parameters, what has never been done. The reference method from which we left is published in [24, 109]. We choose to use ITPM instead of Darcy penalty method [60] because ITPM was demonstrated to be second order convergence in space [109] whereas Darcy penalty is only first order [6]. In addition, ITPM is a more general approach allowing to deal with moving particles, that is our objective in future works.

The paper is organized as follows. In Section 2.2, the main features of the viscous penalty method are presented and discussed. In particular, a new definition of the solid phase function located at the off-diagonal viscosity coefficients is proposed. The uniform Stokes flow past a cylinder is considered in section 2.3. Various numerical parameters such as the numerical diameter of the particle, the penalty viscosity, the augmented Lagrangian parameter or the solid phase function evaluation are studied. At the end, the best set of parameters is proposed for an improved ITPM method, whose convergence order is almost 2. Section 2.4 is devoted to the uniform flow past a square configuration of cylinders. With the previous best set of parameters of ITPM, the friction factor is calculated with our particle-resolved simulation approach. It is compared to Ergun correlation [42] for various solid volume fractions. Conclusions and perspectives are finally drawn in section 2.5.

2.2 Model and numerical methods

Fictitious domain approach

The simulation of solid particles interacting with a carrier fluid is difficult to implement with unstructured meshes in particular with 3D geometries. The commonly

developed alternative approach consists in simulating this kind of flow on a fixed mesh not adapted to the shape of the particle, *i.e.* by considering a solid phase fraction, and to locate the fluid-solid interface thanks to an auxiliary phase function such as the Volume Of Fluid or the Level Set [95]. The concept that separates the particle interfaces and the mesh used to solve the conservation equations is called fictitious domain approach [60, 87]. Indeed, from the motion equation point of view, the interface is not known, only the presence of the solid phase is taken into account into the motion conservation equations thanks to a volume auxiliary function and associated specific forcing terms.

One-fluid model

As previously presented in [109], incompressible two-phase flows involving a carrier fluid and a solid particle phase can be modeled on a fixed mesh with fictitious domain approaches by considering the incompressible Navier-Stokes equations together with a phase function C describing the particle phase shape. By definition, the phase function C equals to 1 in the solid phase and 0 in the fluid medium. The fluid-solid interface is located by the isosurface $C = 0.5$. As explained by Kataoka [59] for fluid/fluid two-phase flows and Vincent [109] for particle flows, the resulting one-fluid model takes implicitly into account the coupling between different phases separated by resolved interfaces, *i.e.* the particles are larger than the mesh cell size. The motion equations reads

$$\nabla \cdot \mathbf{u} = 0 \quad (2.1)$$

$$\rho \left(\frac{\partial \mathbf{u}}{\partial t} + (\mathbf{u} \cdot \nabla) \mathbf{u} \right) = -\nabla p + \rho \mathbf{g} + \nabla \cdot \left[\mu (\nabla \mathbf{u} + \nabla^t \mathbf{u}) \right] + \mathbf{F}_{si} + \mathbf{F}_m \quad (2.2)$$

$$\frac{\partial C}{\partial t} + \mathbf{u} \cdot \nabla C = 0 \quad (2.3)$$

where \mathbf{u} is the velocity in all phases (fluid and solid), p the pressure, t the time, \mathbf{g} the gravity vector, ρ and μ respectively the density and the dynamic viscosity of the equivalent fluid. The four-way coupling between particles and fluid motions is ensured in the momentum equations by the presence of a solid interaction force \mathbf{F}_{si} [17, 74] which is not considered in the present work as only fixed particles are dealt with. The source term \mathbf{F}_m is used to impose a flow rate to the fluid. In the present work, only fixed particles are considered, so equation (2.3) will be discarded.

The one-fluid model is almost identical to the classical incompressible Navier-Stokes equations, except that the local properties of the equivalent fluid (ρ and μ) depend on C . They will be discussed later on in the present work. In the present form, equations (2.1-2.3) do not account for incompressibility and solid constraints. Satisfying these mechanical properties requires developing specific numerical methods called penalty approaches. They are detailed in the next section 2.3.

Penalty methods

As previously explained, the one-fluid model and the fictitious domain approach formulated to deal with particle flows require to consider each different phase (fluid, solid) as a fluid medium with specific material properties (density and viscosity for an isothermal flow). The domain is covered by a set of representative elementary volumes, *i.e.* the mesh cells on a numerical point of view, that are belonging to different sub-domains located by the phase function C . A way to satisfy fluid and solid constraints is to define penalty terms in the momentum equation (2.2). The first publication that reports on this approach was by Saulev [96]. For fixed particles, various improvements were suggested based on Darcy and Volume penalty methods [6, 60, 63]. Concerning moving particles, the viscous penalty method of first order of convergence in space was initially proposed by Ritz and Caltagirone [91]. The method was then improved by [20, 87, 109, 110] to become a second order in space penalty method called ITPM. This method is detailed in the rest of this section and will be used in the present work.

Ensuring the solid behavior in the solid zones where $C = 1$ requires defining a specific rheological law for the rigid fluid part without imposing the velocity. As reported by [109] the solid constraint is intrinsically maintained if the deformation tensor is nullified in the solid sub-domain Ω^s :

$$\forall \mathbf{P} \in \Omega^s, \nabla \mathbf{u} + \nabla^T \mathbf{u} = 0 \quad (2.4)$$

For the resolution of the momentum conservation equation (2.2) in the Navier-Stokes equations, this condition is asymptotically verified when $\mu \rightarrow +\infty$. In other words, viscous penalty method consists in imposing large values of viscosity in the particles compared to the fluid viscosity to implicitly impose the solid behavior and also the coupling between fluid and solid. For fixed particles, the velocity of the Eulerian cells near the centroid of the particle is assumed to be zero. A Darcy penalty method is utilized to satisfy this conditions. The viscous penalty method is used in the rest of the solid particles. Indeed, it propagates the zero velocity in the whole solid medium. The effect of the ratio between the particles and the fluid viscosities will be studied in this work.

A specific model is designed for handling the solid particle behavior in the one-fluid Navier-Stokes equations. It is based on a decomposition of the strain tensor $\bar{\epsilon} = \nabla \mathbf{u} + \nabla^T \mathbf{u}$. Following the work of Caltagirone and Vincent [20], the strain tensor can be reformulated so as to distinguish several natural contributions of the strain tensor dealing with tearing, shearing and rotation. The interest of this decomposition is then to act distinctly on each term in order to strongly impose the associated stress. If we assume that the Navier-Stokes equations for a Newtonian fluid contain all physical contributions traducing shearing or pure rotation effects, the splitting of the viscous stress tensor allows to impose separately these contributions by modifying the orders of magnitude of each term, through the related viscosity coefficients. These penalty terms act directly in the motion equations and so ensure the coupling between the fluid and the solid part of the simulation domain

instantaneously.

Decomposing $\bar{\bar{\epsilon}}$ according to the partial derivative of the velocity in Cartesian coordinates for the sake of simplicity, we obtain [20]

$$\begin{aligned} \bar{\bar{\epsilon}} = & 2 \begin{bmatrix} \frac{\partial u}{\partial x} & 0 & 0 \\ 0 & \frac{\partial v}{\partial y} & 0 \\ 0 & 0 & \frac{\partial w}{\partial z} \end{bmatrix} + 2 \begin{bmatrix} 0 & \frac{\partial u}{\partial y} & \frac{\partial u}{\partial z} \\ \frac{\partial v}{\partial x} & 0 & \frac{\partial v}{\partial z} \\ \frac{\partial w}{\partial x} & \frac{\partial w}{\partial y} & 0 \end{bmatrix} \\ & - \begin{bmatrix} 0 & \frac{\partial u}{\partial y} - \frac{\partial v}{\partial x} & \frac{\partial u}{\partial z} - \frac{\partial w}{\partial x} \\ \frac{\partial v}{\partial x} - \frac{\partial u}{\partial y} & 0 & \frac{\partial v}{\partial z} - \frac{\partial w}{\partial y} \\ \frac{\partial w}{\partial x} - \frac{\partial u}{\partial z} & \frac{\partial w}{\partial y} - \frac{\partial v}{\partial z} & 0 \end{bmatrix} \end{aligned} \quad (2.5)$$

This decomposition is written in compact form as

$$\bar{\bar{\epsilon}}_{ij} = 2 \Lambda_{ij} + 2 \Theta_{ij} - \Gamma_{ij} \quad (2.6)$$

where Λ is the tearing tensor, Θ is the shearing tensor and Γ is the rotation tensor.

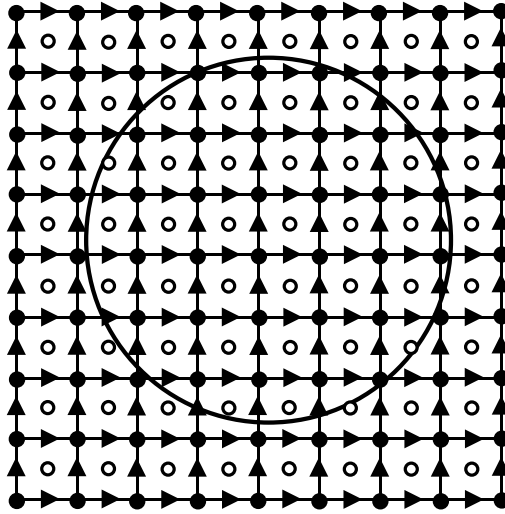


Figure 2.1: Discrete interpretation of the split viscous penalty approach on staggered grids: (●) pressure points, arrows for velocity components and (○) for pure shearing and rotations viscosities. The black line represents the interface between a particle and the carrier fluid.

Consequently, the divergence of the viscous stress tensor for a Newtonian fluid appearing in the one-fluid model (2.2) reads

$$\nabla \cdot (\mu(\nabla \mathbf{u} + \nabla^t \mathbf{u})) = \nabla \cdot [\mu_t \Lambda(\mathbf{u})] + \nabla \cdot [\mu_{sh} \Theta(\mathbf{u})] - \nabla \cdot [\mu_r \Gamma(\mathbf{u})] \quad (2.7)$$

The main interest of formulation (2.7) is to dissociate stresses operating in a viscous flow and then to make the implementation of a numerical penalty method easier. For instance, in a solid phase, if μ is chosen larger than the surrounding fluid viscosity, (2.7) imposes that the local solid flow admits no shearing, no tearing and a constant rotation according to the surrounding flow constraints. These flow constraints are implicitly transmitted to the particle sub-domain as they are solved with the fluid motion at the same time. In the same way, the modifications of the flow motion by the particle movement are directly accounted for (two-way coupling).

For obtaining a second order convergence in space [109], a staggered grid (see Figure 2.1) is needed to implement this strain tensor decomposition where the tearing viscosity $\mu_t = 2\mu$ is located at the pressure nodes whereas the pure shearing $\mu_{sh} = 2\mu$ and rotation $\mu_r = \mu$ viscosities lie on a specific grid, at the center of the mesh grid cells. Defining μ in the solid 2 to 3 orders of magnitude larger than the fluid velocity is equivalent to having μ_t , μ_{sh} and μ_r tending to large values and so acting as viscous penalty terms in the motion equation. In these grid cells, the local medium will be almost solid.

Phase function

The phase function C located at pressure nodes is automatically built by projecting particles onto the pressure mesh (black nodes in Figure 2.1). The color function is defined as the amount of solid in a pressure cell, *i.e.* the local solid fraction. Therefore, in the cells containing the interface, C is computed thanks to virtual test points [109]. In a given pressure cell, 10 test points are seeded in each direction, as illustrated in Figure 2.2. By counting the number of test points belonging to the particle and dividing this number by the total number of test points, the solid fraction C is naturally obtained. It has been previously demonstrated that using 10 points by directions provides an error on C lower than 1% [109].

In our second order convergence penalty approach, a phase function C_μ located at the viscous mesh nodes (white nodes in Figure 2.1) is introduced. As in [109], it can be interpolated from C :

$$C_\mu = \frac{1}{4} \sum_N C_N \quad (2.8)$$

where N denotes the indices of the pressure nodes located at the vertices of the cell to which C_μ belongs.

Alternatively, a projection of the particle on the viscous mesh is proposed in this work to provide the phase function C_μ by using test points, as presented in figure 2.2, instead of interpolating it. The effect of this improvement is studied in this paper.

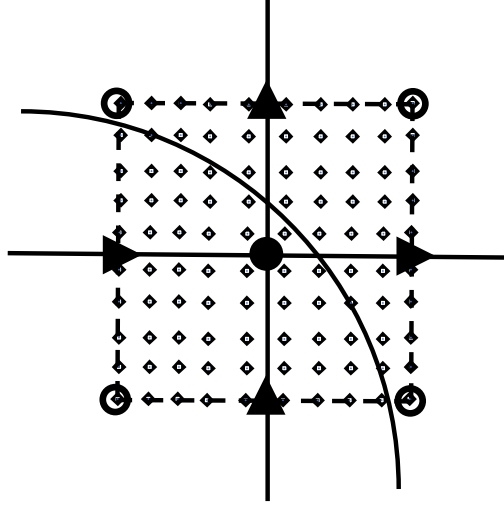


Figure 2.2: Virtual points (◆) on a pressure cell in a staggered grid.

Local properties of the equivalent fluid

On a discrete point of view, the flow grid cells cut by the fluid-solid interface must be distinguished compared to those entirely included in the particles or in the fluid. Different methods can be designed to define the homogenized viscosity μ in these mixed cells. Three different numerical viscous laws have been investigated according to the fluid and solid viscosities (μ_f and μ_s respectively), C for the diagonal viscous stress tensor terms, C_μ for the off diagonal viscous contributions and also a conditional indicator function I_C satisfying $I_{C<0.5} = 1$ if $C < 0.5$ or $I_{C\geq 0.5} = 1$ if $C \geq 0.5$:

1. Discontinuous law:

$$\mu = [\mu_f I_{C<0.5} + \mu_s I_{C\geq 0.5}]$$

2. Arithmetic law:

$$\mu = [(1 - C)\mu_f + C\mu_s]$$

3. Harmonic law:

$$\mu = \left[\frac{\mu_f \mu_s}{C\mu_f + (1 - C)\mu_s} \right]$$

In the previous laws, C can be replaced by C_μ if the viscosity is located at shearing μ_{sh} or pure rotations μ_r nodes. Concerning the density, an arithmetic average is used whatever its location on the discretization grid. The effect of the choice of the viscosity average law is studied in this work.

Augmented Lagrangian method

Following the pioneer work of Fortin and Glowinski [45], an augmented Lagrangian method is applied to the unsteady Navier-Stokes equations dedicated to particulate flows. It allows dealing with the coupling between the velocity and pressure and to satisfy the fluid and solid constraints at the same time by solving a saddle point problem. Starting with $\mathbf{u}^{*,0} = \mathbf{u}^n$ and $p^{*,0} = p^n$, the augmented Lagrangian solution reads

while $\|\nabla \cdot \mathbf{u}^{*,m}\| > \epsilon_{AL}$, solve

$$\begin{aligned} & (\mathbf{u}^{*,0}, p^{*,0}) = (\mathbf{u}^n, p^n) \\ & \rho \left(\frac{\mathbf{u}^{*,m} - \mathbf{u}^{*,0}}{\Delta t} + \mathbf{u}^{*,m-1} \cdot \nabla \mathbf{u}^{*,m} \right) - \nabla (r \nabla \cdot \mathbf{u}^{*,m}) \\ & = -\nabla p^{*,m-1} + \rho \mathbf{g} + \nabla \cdot [\mu (\nabla \mathbf{u}^{*,m} + \nabla^T \mathbf{u}^{*,m})] + \mathbf{F}_{si} \\ & p^{*,m} = p^{*,m-1} - r \nabla \cdot \mathbf{u}^{*,m} \end{aligned} \quad (2.9)$$

where r is an augmented Lagrangian penalty parameter used to impose the incompressibility constraint, m is an iterative convergence index and ϵ_{AL} a numerical threshold controlling the constraint. The augmented Lagrangian method is a kind of penalty technique: if $r \rightarrow +\infty$, the incompressibility is imposed but the solving of the linear system is difficult with iterative solvers as the conditioning of linear system is degraded while $r \rightarrow 0$ does not act on the fluid constraint and keeps the conditioning of the matrix unchanged. As recommended by [45], a constant value of r is used, for example equal to the average between the minimum and maximum eigenvalues of the linear system for Stokes flows [45]. From numerical experiments, optimal values are found to be of the order of ρ_i and μ_i in each phase (fluid or solid) to accurately solve the motion equations in the related zones [108, 110]. Algebraic improvements have also been proposed by Vincent [111] to automatically estimate the local values of r . In the present work, an automatic algebraic estimate of r will be used to optimize as much as possible the conditioning of the linear system while maintaining expected incompressible and solid constraints in the related zones. The effect of the Lagrangian parameter r is considered in the following section 2.3.

Discretization schemes and solvers

All the schemes and solvers utilized in the present work are presented and discussed in detail in [109]. The mass and momentum conservation equations, containing the viscous and augmented Lagrangian penalty terms, are discretized with implicit Finite volumes on structured staggered meshes (see figure 2.1). The time derivative is approximated with a second order Euler scheme while the inertial, viscous and augmented Lagrangian terms are discretized with second-order centered schemes. All fluxes are written at time $(n+1)\Delta t$, except the non-linear inertial term that is linearized with a second order Adams-Bashforth scheme as follows

$$\mathbf{u} \cdot \nabla \mathbf{u} \approx (2\mathbf{u}^n - \mathbf{u}^{n-1}) \cdot \nabla \mathbf{u}^{n+1} \quad (2.10)$$

The obtained linear system can be solved in three-dimensions with a BiCGSTAB II iterative solver [48], preconditioned under a Modified and Incomplete LU approach [39] to speed-up the convergence of the solver. In this work, direct MUMPS solver [4, 5] is preferred as it provides computer error residuals. All the code is working on massively parallel computers by using MPI devices and exchanges [109].

2.3 Uniform Stokes flow past a cylinder

A validation of the presented method and a numerical study of some of its parameters are conducted considering the steady uniform Stokes flow past an isolated cylinder. The analytical solution is illustrated in Figure 2.3. According to [13, 19], a uniform Stokes flow ($Re = 10^{-3}$) past a cylinder of diameter $d = 2m$, with the undisturbed velocity being noted $U_\infty = 1m/s$, is solution of the Brinkman equation $-\nabla p + \mu \Delta \mathbf{u}_i - \frac{\mu}{K} \mathbf{u}_i = 0$. The reference solution is given in polar coordinate frame (r, θ) , centered on the particle, by:

$$\mathbf{u}^*(r^*, \theta) = \begin{cases} \frac{1}{r^*} \left(- \left(1 + \frac{2K_1(\lambda)}{\lambda K_0(\lambda)} \right) \frac{1}{r^*} + r^* + \frac{2}{\lambda K_0(\lambda)} K_1(\lambda r^*) \right) \cos \theta \\ - \left(1 + \left(1 + \frac{2K_1(\lambda)}{\lambda K_0(\lambda)} \right) \frac{1}{(r^*)^2} - \frac{2}{K_0(\lambda)} \left(K_0(\lambda r^*) + \frac{K_1(\lambda r^*)}{\lambda r^*} \right) \right) \sin \theta \end{cases} \quad (2.11)$$

$$p^*(r^*, \theta) = \frac{2}{Re} \lambda^2 \left(- \left(1 + \frac{2K_1(\lambda)}{\lambda K_0(\lambda)} \right) \frac{1}{r^*} - r^* \right) \cos \theta \quad (2.12)$$

where $\mathbf{u}^* = \frac{\mathbf{u}}{U_\infty}$, $p^* = \frac{p}{\rho U_\infty^2}$, $r^* = \frac{2r}{d}$, $\rho = 1kg.m^{-3}$ is the fluid density, $\lambda = \frac{d^2}{4K}$ is the dimensionless permeability of the porous medium in Brinkman sens, K is the permeability of the inside and outside the porous cylinder, K_0 and K_1 are the modified Bessel functions of rank 0 and 1. For $K \rightarrow 0$, the porous cylinder can be likened to an impermeable solid particle whereas outside the cylinder, $K \rightarrow +\infty$ to obtain a fluid behavior.

Simulations setup

The computational domain used to simulate a uniform Stokes flow past a cylinder is a square of a Length $L = 2d$, and the spatial discretization, using a regular Cartesian grid called Eulerian mesh, is represented by the number of grid cells across the diameter of the particle $\frac{d}{\Delta x} = 20$. The velocity and pressure exact solutions ((2.11), (2.12) respectively) for a Stokes flow past a cylinder were taken as initial condition, as illustrated in Figure 2.3. They were also implemented at boundary conditions as a Dirichlet condition to be able to simulate such a flow in a numerically small domain not extending to infinity as Stokes flow would require.

A first simulation of a uniform flow past a cylinder is carried out using a reference set of parameters presented bellow:

- Viscous law: Arithmetic average law is chosen for this simulation.

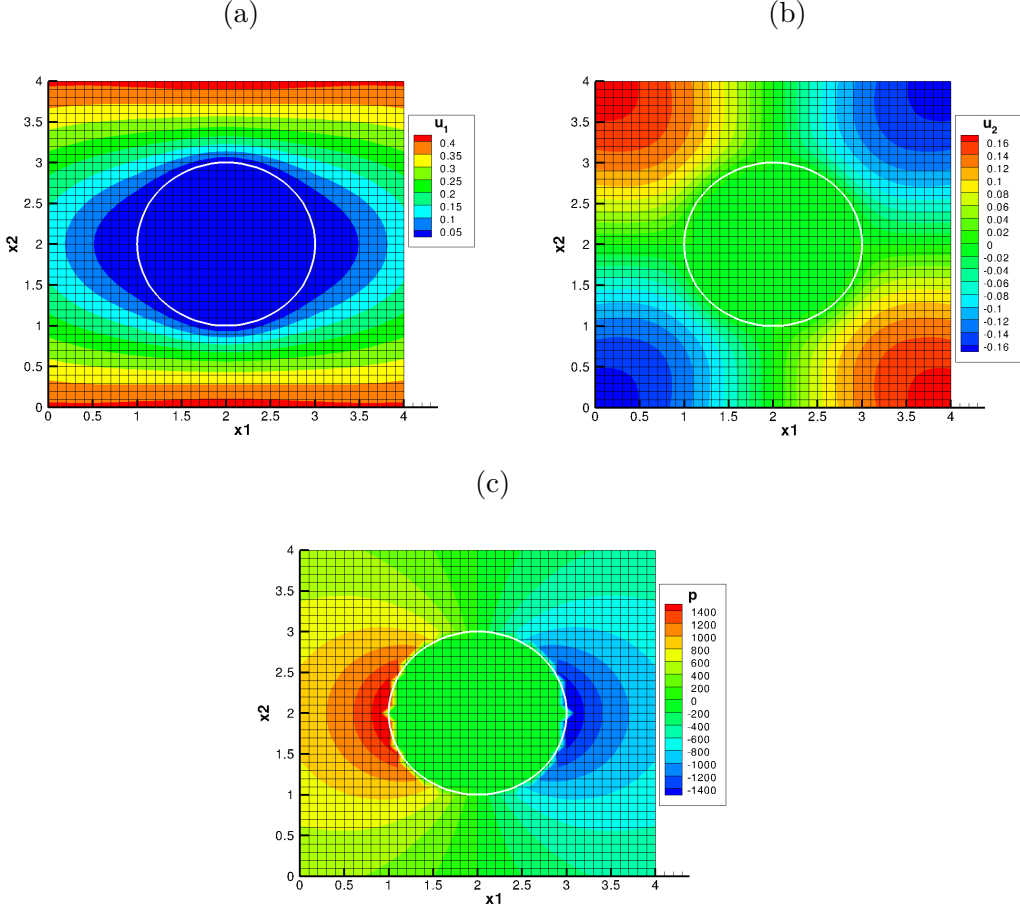


Figure 2.3: Exact solution for a Stokes flow past a fixed cylinder: the first velocity component field u_1 (a), the second velocity component field u_2 (b), and the pressure field p (c), are plotted at each point of the domain (fluid and solid).

- Numerical radius: it has been previously mentioned [109] that on a numerical point of view, the cylinder radius has to be tuned according to its physical radius. Indeed, interpolations are used in the cells cut by the fluid-solid interface for viscous discrete nodes, inducing numerical variations of the solid phase compared to the real one. In our simulations, the numerical radius R_n of the cylinder is given by:

$$R_n = \frac{d}{2} + e \frac{\Delta x}{16}$$

e is a correction coefficient on R_n . It is imposed to be $e = 0$, *i.e.* $R_n = \frac{d}{2}$, so that R_n is the physical radius of the cylinder for this simulation.

- Computation of C_μ : For the first simulation, it is interpolated from C , known in the pressure mesh, on the viscous mesh.

- The viscosity ratio $\frac{\mu_s}{\mu_f}$ between the viscosity imposed in the Eulerian cells inside the cylinder μ_s and the fluid viscosity μ_f is chosen such that $\frac{\mu_s}{\mu_f} = 500$ for this simulation.
- The Lagrangian parameter is $r = 10^5$.

Figure 2.4 shows the relative error in each point of the domain for the velocity

$$Error = \begin{cases} \frac{|u_{Simu} - u_{Analytic}|}{|u_{Analytic}|} & \text{if } u_{Analytic} \neq 0 \\ |u_{Simu}| & \text{if } u_{Analytic} = 0 \end{cases} \quad (2.13)$$

and the pressure between the simulation results and the analytical solution given by (2.11) and (2.12). This error is about 100% for the pressure in the fluid domain as illustrated in Figure 2.4(c) and more than 50% in the fluid region near the cylinder and about 10% in the rest of the fluid domain for both velocity components as illustrated in Figure 2.4(a), Figure 2.4(b).

Facing this huge error for both pressure and velocity, we decided to conduct a numerical study on the effect of previously listed numerical parameters on the simulation results. Our main goal is to set up the selection of parameters to minimize these errors. At the end of each study, the simulation results obtained with new parameters will be given in order to show the improvement made.

Sensitivity of simulations to viscous law, numerical radius R_n and phase function computation C_μ on the viscous mesh

The viscous law and the numerical radius are first investigated. To do so, several simulations are carried out with discontinuous, arithmetic and harmonic average laws (for both C and C_μ which is interpolated at this state) and for different numerical radius as follows:

$$R_n = \frac{d}{2} + e \frac{\Delta x}{16} \quad e \in [-16, 16]$$

All other parameters remain unchanged: $\frac{\mu_s}{\mu_f} = 500$ and $r = 10^5$.

Figure 2.5 shows the velocity L1 relative error in the whole domain

$$Error = \frac{\sum |u_{Simu} - u_{Analytic}|}{\sum |u_{Analytic}|} \quad (2.14)$$

for the Stokes flow past a cylinder for different viscous laws. It can be observed that the minimum error for arithmetic average law is reached for $R_n = \frac{d}{2} - \Delta x$ whereas it is reached for a numerical radius $R_n = \frac{d}{2} + \frac{\Delta x}{8}$ for harmonic and discontinuous average laws. This minimum error is about 1% for both harmonic and discontinuous law whereas it is 0.5% larger for the arithmetic law with R_n being modified in

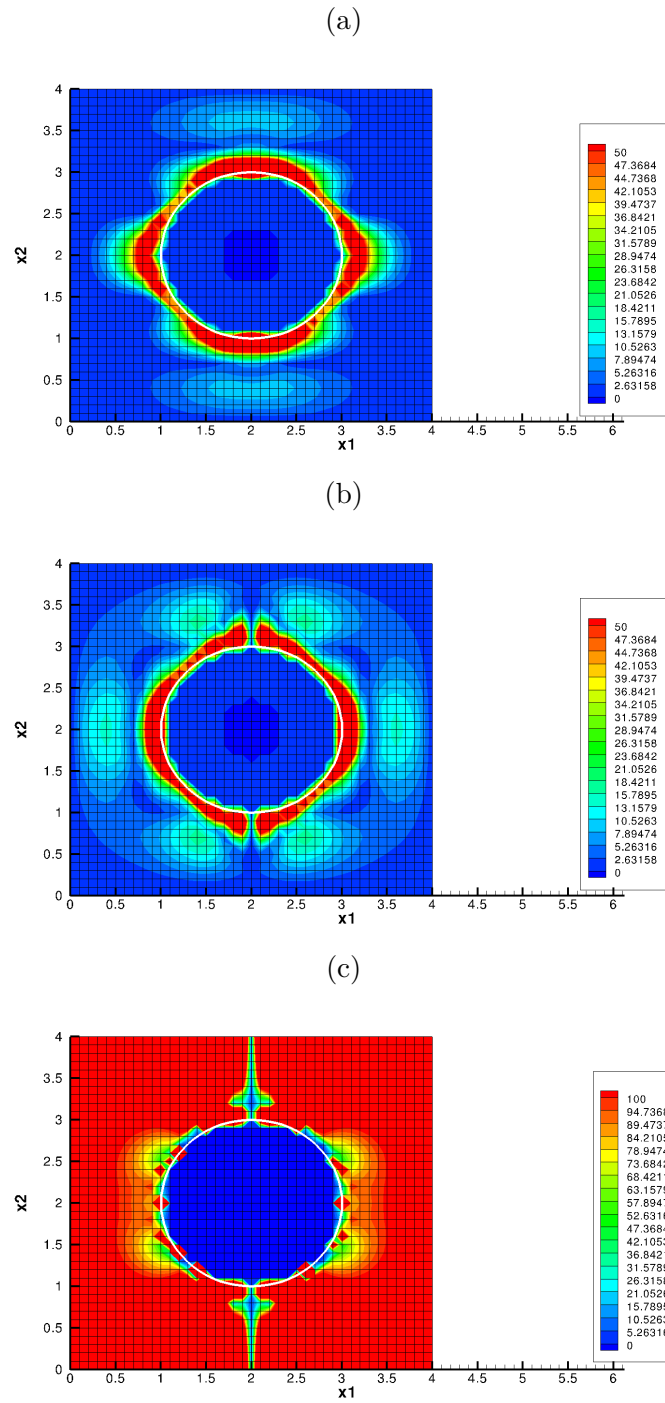


Figure 2.4: Relative error (%) in the whole domain (fluid and solid zones) of the first component of velocity u_1 (a), the second component of velocity u_2 (b) and the pressure p (c) for Stokes flow past cylinder.

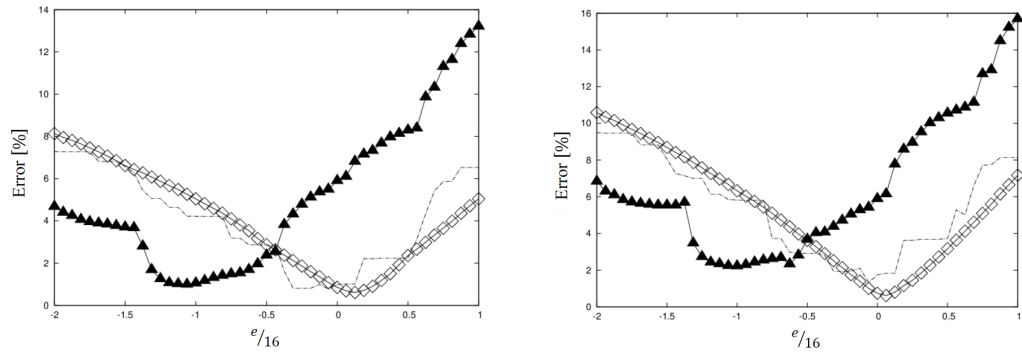


Figure 2.5: Relative error (%) of the first component of velocity u_1 (left) and the second component of velocity u_2 (right) for Stokes flow past a cylinder simulated using different viscous laws: (---) discontinuous, (\diamond) harmonic and (\blacktriangle) arithmetic average. C_μ is interpolated from C computed by projecting the cylinder on the pressure mesh.

a larger extent. A first conclusion here is that choosing harmonic or discontinuous averages is more desirable as R_n is closer to the physical cylinder radius and the obtained error is smaller

Until now, the color function on the viscous mesh C_μ was interpolated from C computed on the pressure mesh [109]. One interesting issue is how the error implied by the different average laws will change if C_μ is computed directly on the viscous mesh by projecting the cylinder shape with the virtual point procedure presented before in figure 2.2. To answer this question, the same study is conducted on R_n and average viscous laws by considering the C_μ directly calculated on the viscous points without using the pressure nodes.

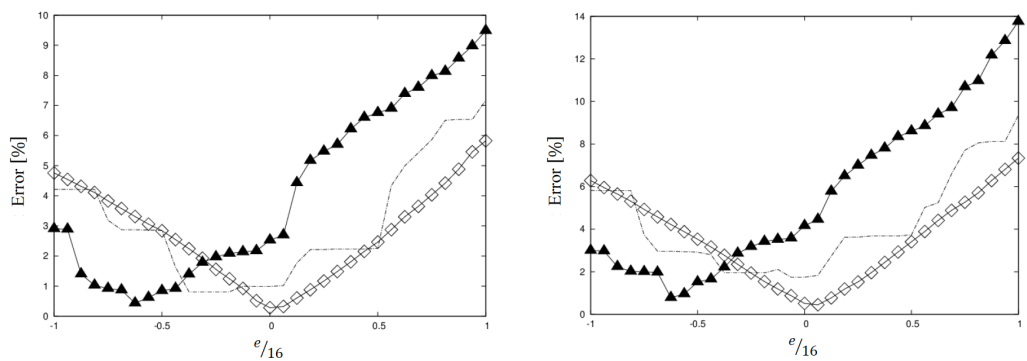


Figure 2.6: Relative error (%) on the first component of velocity u_1 (left) and the second component of velocity u_2 (right) for Stokes flow past a cylinder simulated using different viscous laws: (---) discontinuous, (\diamond) harmonic and (\blacktriangle) arithmetic average. C_μ is computed by projecting directly the cylinder shape on the viscous mesh.

Figure 2.6 shows the velocity L1 relative error in the whole domain (2.14) for Stokes flow past a cylinder for the three viscous laws discussed above but with the color function C_μ computed on the viscous mesh instead of interpolating it from the C function on the pressure nodes as in previous simulations. One can observe that the minimum error is reached for a numerical radius $R_n = \frac{d}{2} - \frac{\Delta x}{2}$ for arithmetic average law instead of $R_n = \frac{d}{2} - \Delta x$ when C_μ was interpolated, whereas the new C_μ computation seems to have no influence on the discontinuous law results. On the other hand, for the harmonic average law, not only the minimum error is divided by 10 but also this error is reached for the physical diameter of the cylinder $R_n = \frac{d}{2}$. Therefore, and for the rest of this work, the color function C_μ will always be computed by projecting the particle shape on the viscous mesh, together with the use of the harmonic average law to compute the viscosity in the Eulerian mesh containing the interface. This important conclusion is new and has never been obtained in previous penalty simulations of particle flows [34, 35, 77, 109]

A new simulation is carried out with a new set of parameter -conclusion of the numerical study above-. They are given by:

- Viscous law: harmonic average law instead of arithmetic law.
- Numerical radius: it is kept unchanged *i.e.* equal to the physical cylinder radius $R_n = \frac{d}{2}$.
- The color function C_μ is computed on the viscous mesh instead of being interpolated from C .
- The viscosity ratio is the same $\frac{\mu_s}{\mu_f} = 500$.
- The Lagrangian parameter $r = 10^5$ remains the same.

With this new set of numerical parameters, Figure 2.7 shows the huge improvement brought by the new set of numerical parameters on relative error for the velocity (2.13) and the pressure. Indeed the error decreases from 100% to less than 5% for the pressure in the fluid domain, except in the cells containing the interface as illustrated in Figure 2.4(c). If we refer to Figures 2.4(a) and 2.4(b), the error went from 50% to 10% in the fluid region near the cylinder and from 10% to less than 2% in the rest of the fluid domain for both velocity components.

Effect of the viscosity ratio and the augmented Lagrangian parameter r

The viscous penalty method consists in imposing large values of viscosity in the Eulerian cells belonging to the solid phase, compared to the fluid viscosity. This penalty method allows ensuring the solid behavior in the particles. Therefore, the

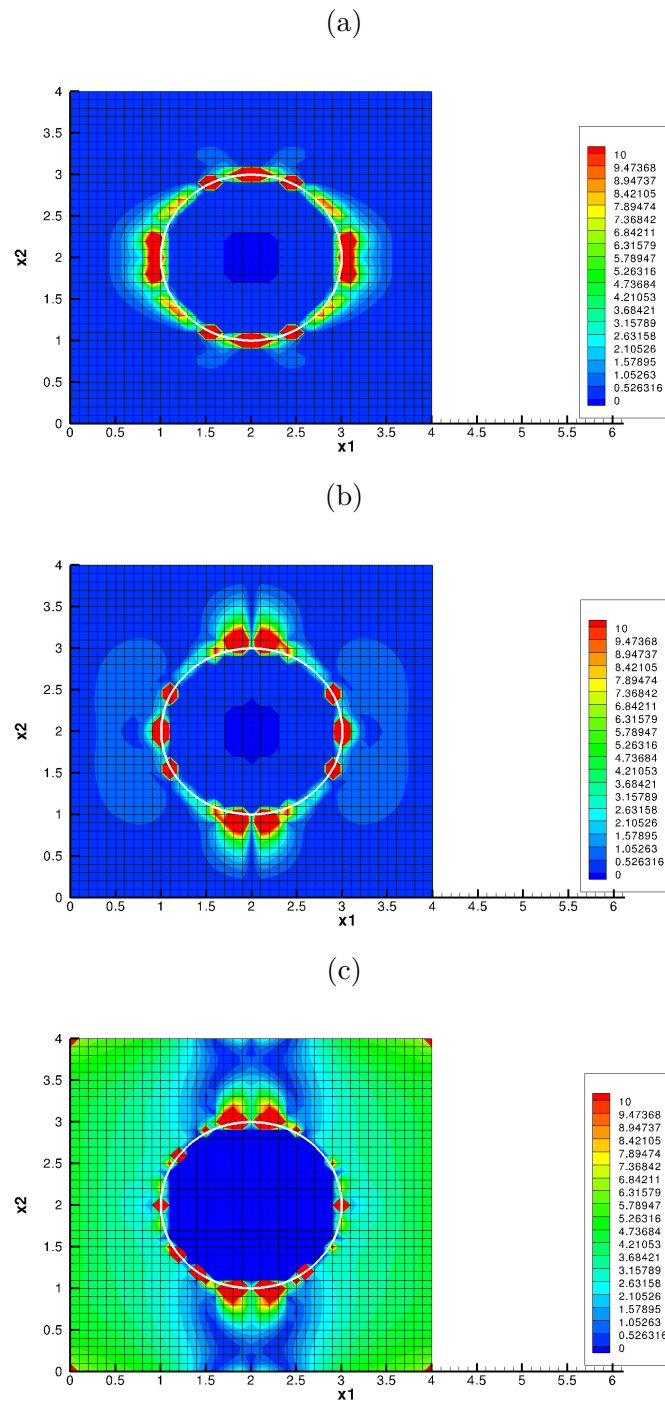


Figure 2.7: Relative error (%) of the first component of velocity u_1 (a), of the second component of velocity u_2 (b) and of the pressure p (c) for Stokes flow past cylinder in the whole domain.

viscosity ratio $\frac{\mu_s}{\mu_f}$ is to be carefully considered to simulate gas-solid flows as best as possible with the viscous penalty method. For this motivation, numerous simulations of a uniform Stokes flow past an isolated fixed cylinder were carried out, with different values of $\frac{\mu_s}{\mu_f}$, to study the viscosity ratio effect on the viscous penalty method accuracy.

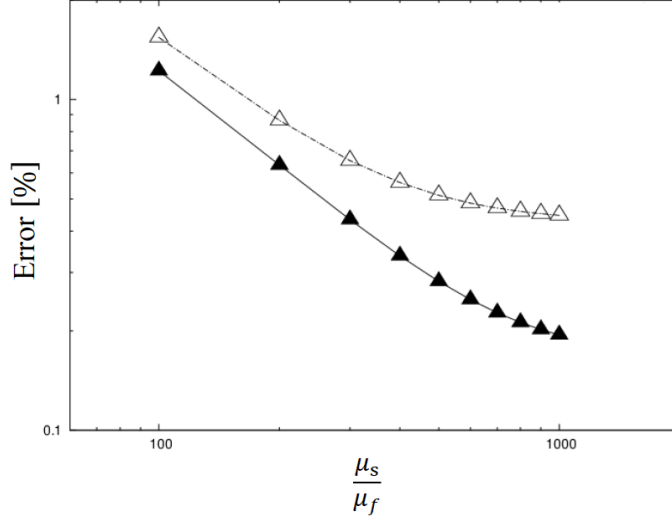


Figure 2.8: Relative error (%) on the first component of velocity u_1 (\blacktriangle) and the second component of velocity u_2 (\triangle) for Stokes flow past a cylinder simulated with different viscosity ratio.

Figure 2.8 shows the velocity L1 relative error in the whole domain (2.14) for Stokes flow past a cylinder for a viscosity ratio between 100 and 1000. It can be observed that the error of the second component of velocity seems to be viscosity ratio independent from $\frac{\mu_s}{\mu_f} \geq 600$ and to stabilize for the first component of velocity when $\frac{\mu_s}{\mu_f} \geq 900$. Therefore, $\frac{\mu_s}{\mu_f} = 1000$ seems to be a reasonable choice in order to get a viscosity ratio independent solution. This viscosity ratio will be used in the rest of this work.

The last numerical parameter to be studied in this work is the Lagrangian parameter r . Indeed, the augmented Lagrangian method is a kind of penalty technique, and the incompressibility is imposed when $r \rightarrow +\infty$. Therefore, knowing from which value of r the solution does no longer depend on it is an important matter to be carefully studied. Indeed, the larger r is, the worse is the solving of the linear system. As a consequence, r has to be large to impose incompressibility and at the same time the smallest possible to keep the conditioning of the linear system as small as possible too.

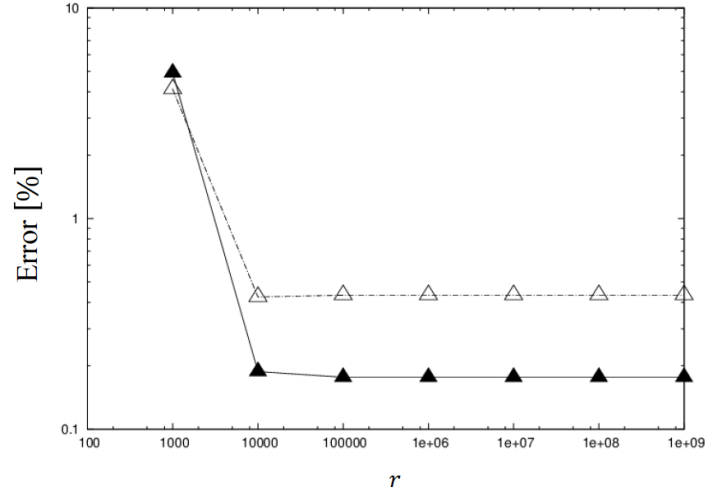


Figure 2.9: Relative error (%) on the first component of velocity u_1 (\blacktriangle) and the second component of velocity u_2 (\triangle) for Stokes flow past a cylinder simulated with different Lagrangian parameter values.

Figure 2.9 shows the velocity L1 relative error in the whole domain (2.14) for Stokes flow past a cylinder for a Lagrangian parameter r between 10^3 and 10^9 . One can observe that the solution is augmented Lagrangian parameter independent for $r \geq 10^5$. This is the value that will be used in the rest of this work. Note that in this work, the resolution of the linear system is ensured by a direct solver, which allows us to use a large values of r . On the other hand, the use of an iterative solvers can be difficult in the case of $r = 10^5$. This point is not addressed in the present work.

A new simulation is carried out with the set of all most efficient parameters, summarized below:

- Viscous law: harmonic average law.
- Numerical radius: physical cylinder radius $R_n = \frac{d}{2}$.
- The color function C_μ is computed on the viscous mesh.
- The viscosity ratio is $\frac{\mu_s}{\mu_f} = 1000$ instead of $\frac{\mu_s}{\mu_f} = 500$.
- The Lagrangian parameter is kept $r = 10^5$.

Figure 2.10 shows the relative error for the velocity (2.13) and the pressure between the results of the penalty simulation with the best set of parameters and the analytical solution. It can be seen that error is now lower than 1% for either velocity and pressure in the fluid area far from the particle, and about 10% in the region containing the interface. This is mainly due to the one-fluid model for which the physical proprieties of the equivalent fluid in the mixed cells are neither fluid

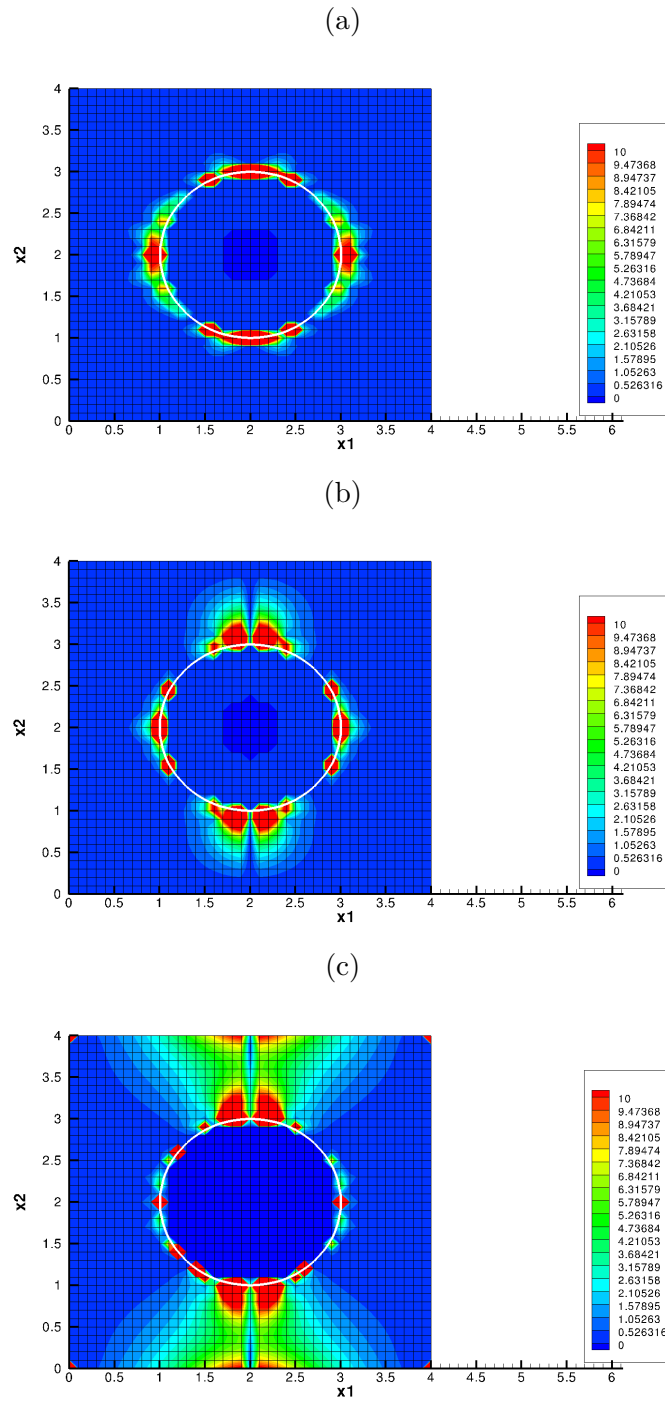


Figure 2.10: Relative error (%) on the first component of velocity u_1 (a), the second component of velocity u_2 (b) and the pressure p (c) for Stokes flow past cylinder in the whole domain.

nor solid but an average of them, consequently the velocity and the pressure in these cells are less accurate.

Order of convergence

Given the fact that we have been able to find a satisfactory set of parameters to obtain accurate result on velocity and pressure, as illustrated in Figure 2.10, a study of convergence order of the viscous penalty method is conducted by simulating a series of uniform flow past a cylinder using the best set of parameters and by changing the Eulerian mesh resolution using different $\frac{d}{\Delta x}$.

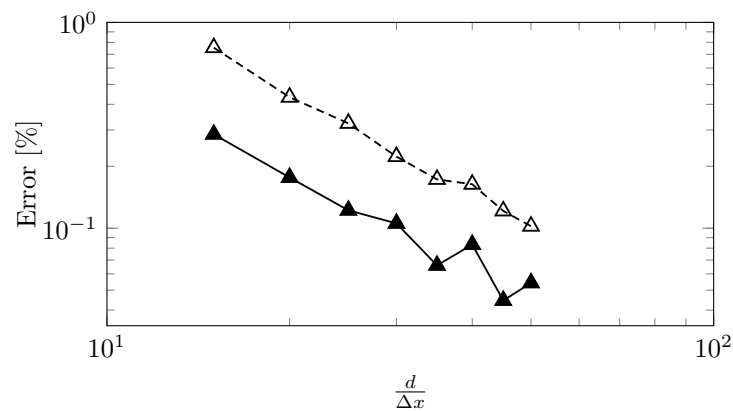


Figure 2.11: Relative error (%) on both velocity components for Stokes flow past a cylinder with respect to Eulerian mesh refinement.

Figure 2.11 shows L1 relative error in the whole domain (2.14) for both component of velocity with respect to the Eulerian mesh resolution given by $\frac{d}{\Delta x}$. The order of convergence computed from these error between the simulation results and (2.11), (2.12) is 1.67 based on a logarithmic data fit. It can be observed that some oscillations appears when refining the Eulerian mesh. A possible reason could be the effect of the particle interface position with respect to the Eulerian mesh. To assess this assumption, we have conducted different simulation by changing only the position of the cylinder inside the same Eulerian mesh: the cylinder center coordinates (x_c, y_c) are:

$$x_c = i \frac{\Delta x}{10} \quad , \text{ where } \quad i \in \llbracket 0, 10 \rrbracket$$

$$y_c = j \frac{\Delta y}{10} \quad , \text{ where } \quad j \in \llbracket 0, 10 \rrbracket$$

Figure 2.12 shows the effect of the position of the Lagrangian mesh with respect to the Eulerian mesh. It is observed that the way that the interface intersects the

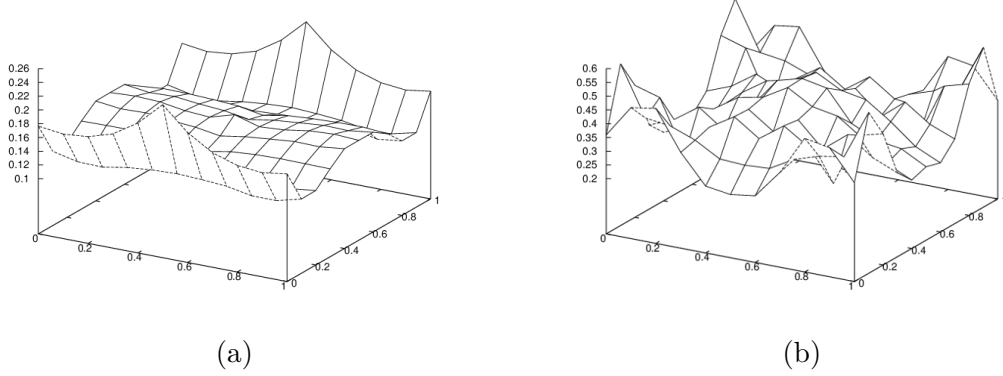


Figure 2.12: Relative error (%) on the first component of velocity u_1 (a) and the second component of velocity u_2 (b) for Stokes flow past cylinder with respect to cylinder center position.

Eulerian mesh clearly affects the velocity results. In the convergence order study, the Eulerian mesh refinement changes the way the interface cuts the Eulerian cells, which explains the oscillations.

2.4 Uniform flow past a square configuration of cylinders

To validate the viscous penalty method outside the Stokes regime and with the new set of parameters prescribed in previous section 2.3, an additional test is investigated: a uniform flow past a square configuration of cylinders. This configuration consists in putting a cylinder of a diameter d in a periodic square of length L . This configuration is equivalent to an infinite array of cylinders equidistant from each other in each direction. The Eulerian mesh refinement respects the condition given in [24]: $\Delta x = \frac{d}{5\sqrt{Re}}$ which ensure the boundary layer resolution if $Re > 16$ and

$\Delta x = \frac{d}{20}$ if $Re < 16$. The fluid is accelerated using a pressure drop $\mathbf{F}_m = \frac{\Delta P}{L}$ as a source term in the momentum equation. The domain length L is fixed, given a solid volume fraction α_d , by:

$$\frac{L}{d} = \frac{1}{2} \sqrt{\frac{\pi}{\alpha_d}}$$

An illustration of a uniform flow past a square configuration of cylinders for different solid volume fraction ($\alpha_d = 0.2$, $\alpha_d = 0.4$ and $\alpha_d = 0.6$) is given in Figure 2.13.

The aim of this section is to validate the superficial mean fluid velocity $\langle \mathbf{u}_f \rangle = (1 - \alpha_d) \frac{\int_V (1 - C) \mathbf{u} dV}{\int_V (1 - C) dV}$, where \mathbf{u} is solution of the Navier-Stokes equation using the viscous penalty method (ITPM) with the best set of parameters proposed in the previous section 2.3. Numerous correlation have been proposed for predicting

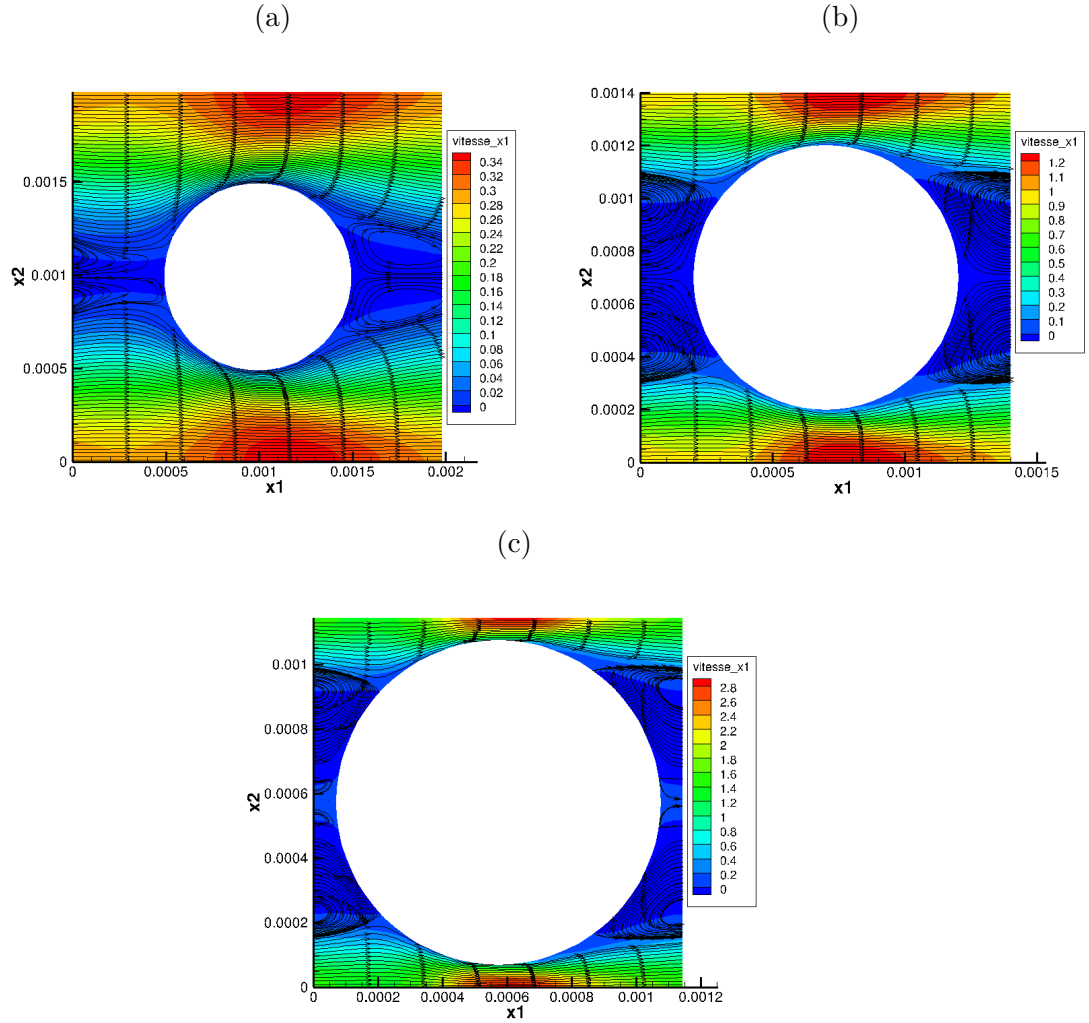


Figure 2.13: Streamlines and u_1 component of velocity field for a steady uniform flow along the x -axis of a square configuration of cylinders for different solid volume fractions: $\alpha_d = 0.2$ (a), $\alpha_d = 0.4$ (b), $\alpha_d = 0.6$ (c).

$\frac{\Delta P}{L}$ from the $\langle \mathbf{u}_f \rangle$: Darcy [32] was the earlier pioneer in the subject by proposing in the Stokes limit the linear relation $\frac{\Delta P}{L} = \frac{\mu}{K} \langle \mathbf{u}_f \rangle$. At higher Reynolds number, this relation is no longer linear due to inertial effects. Ergun [42] established a semi-empirical relation given by:

$$\frac{\Delta P}{L} = 150 \frac{\alpha_d^2}{(1 - \alpha_d)^3} \frac{\mu \langle \mathbf{u}_f \rangle}{d^2} + 1.75 \frac{\alpha_d}{(1 - \alpha_d)^3} \frac{\rho \langle \mathbf{u}_f \rangle^2}{d} \quad (2.15)$$

This relation is a generalization of the Forchheimer equation [44].

Given the non-dimensional friction factor f_p defined as:

$$f_p = \frac{\Delta P}{L} \frac{d}{\rho \langle \mathbf{u}_f \rangle^2} \quad (2.16)$$

and the Reynolds number Re given by:

$$Re = \frac{\rho \langle \mathbf{u}_f \rangle d}{\mu \alpha_d}$$

the Ergun equation (2.15) can be written as:

$$f_p = \frac{\alpha_d}{(1 - \alpha_d)^3} \left(\frac{150}{Re} + 1.75 \right) \quad (2.17)$$

The validation consists in

- simulating a uniform flow past a square configuration of cylinders, for a given pressure drop $\frac{\Delta P}{L}$ and a solid volume fraction α_d
- extracting from the velocity field the superficial mean fluid velocity $\langle \mathbf{u}_f \rangle$
- computing the friction factor f_p using (2.16)
- comparing f_p to the Ergun correlation [42] given by (2.17).

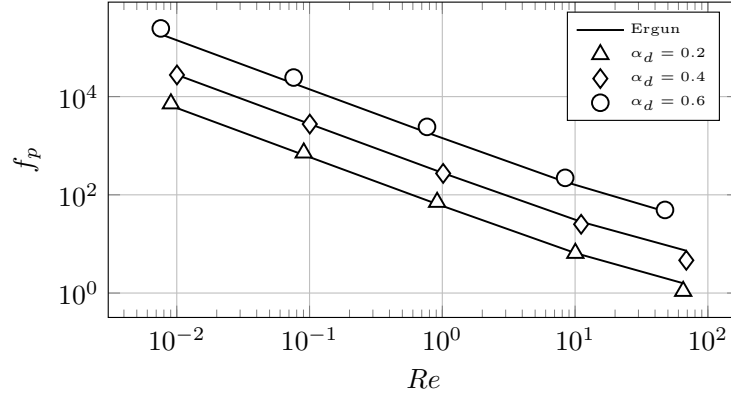


Figure 2.14: Friction factor for a uniform flow past a square configuration of cylinders.

Figure 2.14 shows the good agreement of the friction factor deduced from the superficial mean fluid velocity $\langle \mathbf{u}_f \rangle$ using (2.16) and Ergun's correlation [42]. This validate the viscous penalty method at Higher Reynolds number with the best set of parameters found in the previous section 2.3: harmonic average for viscous laws, $R_n = \frac{d}{2}$, C_μ computed on the viscous mesh, $\frac{\mu_s}{\mu_f} = 1000$ and $r = 10^5$.

2.5 Conclusions and Suggestions

The Viscous Penalty Method ITPM [109] has been used to simulate two-dimensional fixed particulate flows. The first goal of the work was to set up the best numerical parameters in order to obtain lower errors as possible when the simulations are compared to the analytical solution for the Stokes flow around a cylinder. The viscosity ratio between the fluid and the penalty viscosity μ_s inside the particle, the augmented Lagrangian parameter r , the viscous law, the solid fraction estimate C_μ at the viscous nodes and the numerical radius of the particle were investigated. For the first time, we have been able to demonstrate that if C_μ is directly calculated by projecting the real shape of the particle on the viscous nodes, the numerical radius of the particle R_n does not have to be adapted compared to its real physical value. Moreover, the best accuracy is obtained when an harmonic law on the viscosity is used to build the equivalent properties of the one-fluid model in cells cut by the fluid/particle interface. Concerning the penalty viscosity, imposing 1000 times the fluid velocity is the best compromise between error level and solving efficiency. To finish with setting of ITPM parameters, $r = 10^5$ allows to satisfy the incompressibility and solid constraints with lower errors as possible. Using larger values of μ_s and r does not improve the accuracy of ITPM, due to numerical errors coming from the rest of the numerical methods and solver efficiency. A convergence study was conducted with respect to mesh refinement. An order of 1.67 was obtained for all velocities inside the fluid.

A second problem was considered at larger particle Reynolds number: the uniform flow past a square arrangement of cylinders. With the best set of ITPM parameters, comparisons of simulations with reference correlations of Ergun allowed us to demonstrate that for various solid fractions ranging from 0.2 to 0.6, the simulations were in very good agreement with the expected values.

Ongoing works are developed in several directions:

- the ITPM is used to extract the drag and lift force coefficient for various arrangements of spherical particles [24]
- the ITPM is extended to heat transfers in particulate flows. As for the force coefficient, the heat transfer coefficient is extracted for any particle inside various arrangements of spheres [23]
- the viscous penalty method is utilized to simulate the force exerted by an incompressible flow on ellipsoidal particles as well as heat transfer coefficients [25]

Chapter 3

Accurate estimate of drag forces using particle-resolved direct numerical simulations

This chapter is the article [24] authored by M.-A. Chadil, S. Vincent and J.-L. Estivalezes

Abstract

An accurate force estimate for finite-size particle simulations is proposed based on Lagrange extrapolation of third order, coupled with a Taylor interpolation of same order, to estimate pressure and viscous constraints on the surface of particles. The main point of our approach is to upwind the interpolation support in the normal direction to the fluid/solid interface so as to use only fluid values to estimate forces. Also, detailed validations of forces are considered for estimating accuracy and convergence order of the method on various incompressible motions such as the flow around an isolated particle at various Reynolds numbers and flows across packed spheres under Face-Centered Cubic, random and bi-disperse arrangements.

3.1 Introduction

In the framework of finite-size particle motions, the numerical simulation of a particulate flow interacting with a surrounding fluid can be investigated following two different numerical strategies: unstructured or structured grids. This important choice is in particular motivated by the instantaneous description of the evolving complex shape represented by the interface between the carrier fluid and a set of moving particles. On the one hand, the more natural discretization seems to be the implementation of an unstructured body-fitted grid to simulate the fluid area in the two-phase particle flow [29, 56, 57, 72]. Building such a finite-volume or finite-element mesh in three-dimensions is not easy and requires automatic remeshing as the solid particles move according to time and space. The remeshing process at each calculation step is time consuming and can be very difficult to manage automatically

in computer softwares when the global shape of the fluid-solid interface is changing at each calculation step [40]. On the other hand, it can be imagined to develop a fixed structured grid approach to simulate particulate flows. With this method, the mesh is not adapted to the fluid-solid interfaces and includes both phases. On a mesh point of view, this approach is simpler than the previous one. The difficulty lies in taking into account the presence of particles in the fluid whose interface is not explicitly tracked by the mesh that does not conform to the fluid/particle interface. This type of modeling and numerical problem belongs to the class of fictitious domains [60, 78]. The penalty modeling strategy [108, 109, 110] developed hereafter is based on this approach and will be reported in the next section 3.2.

One major interest of finite-size particle motion simulation is to provide a local estimate of all flow characteristics (velocity, pressure, viscous stress) together with a local description of the particle-fluid interface. The resolved scale particle motion does not require any force modeling nor interaction model as soon as the mesh is refined enough. In the present work, we will demonstrate that having at least 5 points in the boundary layer attached to a given particle allows to recover all the physics of the particle flow without using any force or interaction model (drag, lift, lubrication, etc). As a consequence, the finite-size particle approach can be considered as a kind of fully resolved Direct Numerical Simulation (DNS) of the particulate flow as soon as no modeling is required to solve the problem. The mesoscopic or macroscopic particle flow models (Eulerian-Lagrangian, Eulerian-Eulerian) do require the knowledge of interaction forces to close specific particle-motion interaction terms. For an isolated particle in an infinite medium, the drag force law of Schiller and Naumann [97] is well known and often used in large scale models. For fixed and moving beds of particles, we can cite the correlations based on experiments proposed by Ergun [42] and Wen&Yu [114] and also Gobin [46] who proposed a correlation based on these two correlations. As soon as the solid fraction is high and the particle size or shape of particles is not constant (bi-dispersed flows, spheroidal particles, etc), drag and lift laws have to be designed. This is the main objective of the present work, *i.e.* providing a DNS framework with accurate force calculation in order to finally obtain new force laws for various particulate motions.

Numerous numerical works have been devoted to performing DNS of finite-size particulate flows and obtaining resulting drag force laws from the macroscopic analysis of local flow motions in the vicinity of the particle surface. The first class of numerical models, generally investigated for fixed arrangements of particles, is the Lattice Boltzmann approach. It was used in numerous works by Ladd [64, 65] for particle suspensions, by Hill *et al.* [51] for monodisperse face cubic centered (FCC) array of spheres, by Hoef *et al.* [53] and Beetstra *et al.* [12] for random monodisperse and bidisperse array of spheres to cite a few. Another class of very popular methods for handling finite-size particle is the Immersed Boundary Method (IBM) coupled with incompressible Navier-Stokes equations initially developed for particulate flows by [105, 106, 113]. For random monodisperse array of spheres, the work of Tenneti *et al.* [103] is very interesting as it covers a wide range of solid fractions $\alpha_d = 0.1 - 0.4$, and also Reynolds number up to 300. At the end,

a new correlation is proposed for drag force laws. The last interesting class of numerical approaches is the body fitted mesh method, that is restricted to fixed array of particles as it is impossible to generate automatically a three-dimensional mesh that adapts to the motion of particles. Among the most interesting works in the field, we can cite the simulations and analysis of Massol [70] for monodispersed FCC arrays of spheres. The Massol's work [70] was conducted using AVBP code [98] destined to unsteady simulation. This is an unstructured mesh code with third order finite volume scheme in time and space. Massol [70] studied various grid type (hexahedra and hybrid prims/tetrahedra) and resolution effects on the drag force. Indeed, simulations of Face-Centred Cubic arrangements of spheres were carried out at Reynolds number 50 and solid volume fraction of 0.15 with hexahedra grids when the number of points changed from 304904 to 812312 and drag difference was of 2%. With hybrid prisms/tetrahedra grids, when the number of points changed from 249619 to 559893, the maximum drag difference was of 1%. Finally the maximum drag difference between the two grid type was about 2%.

In all these numerical approaches, the drag force can be deduced in different ways:

- with Darcy penalty methods [84], it can be obtained directly from the source term used to accelerate the fluid outside the particles.
- with the LBM, the drag force exerted by the fluid on the particles is calculated according to the momentum exchange algorithm of Ladd [64].
- In the IBM approach, the forces exerted by the fluid on the particles can be deduced from the reaction IBM force imposed in the momentum equations to satisfy a solid behaviour [18, 113], or by using the velocity and pressure fields solution of the Navier-Stokes equation [73, 103].
- with the Volume Penalty Method (VPM), Bizid [14] uses Taylor extrapolations to get the pressure and viscous stress projection on particle surface.

Our major contribution is to propose an accurate force estimate for finite-size particle simulations. Even if all full DNS of particle flows extract forces on particles [57, 85, 105, 109], few works report on how practically these forces can be calculated and what is the accuracy or convergence order of the forces. Among the wide literature devoted to full DNS of particle motions, we can cite the work of Bizid [13, 14] who uses Taylor extrapolation to estimate pressure and viscous constraints on the particle surface. This approach is of low accuracy as it utilizes velocity and pressure values that can be inside the particle volume. The most advanced work on force calculation on immersed interfaces is due to Zastawny *et al.* [116] with an improved mirroring immersed boundary method. In the present work, a new force calculation is proposed based on Lagrange extrapolation of third order, coupled with a Taylor interpolation of same order. The main point of our approach is to upwind the interpolation support in the normal direction to the fluid/solid interface so as to use only fluid values to estimate forces. Detailed validations of forces are considered for estimating accuracy and convergence order of the proposed method.

The article is structured as follows. A presentation of the models and numerical methods is first proposed in section 3.2, paying attention to describe fictitious domain and penalty methods used to model and approximate incompressible particulate motions. In the third section 3.3, a new force calculation for immersed interfaces is proposed, with discussions conducted on order of approximations and associated accuracy. Validations for flows interacting with isolated spherical particles at various Reynolds number are presented in the fourth section 3.4. Section 3.5 is devoted to simulations and validations of flows through fixed arrangements of mono- and bi-dispersed spheres. Finally, conclusions and perspectives are drawn.

3.2 Model and numerical methods

3.2.1 Fictitious domain approach

The modeling and simulation of moving objects (bubbles, droplets, solid particles) interacting with a carrier fluid is impossible to realize with unstructured meshes as soon as these objects deform or move in a 3D geometry. The commonly developed alternative approach consists in simulating this kind of flow on a fixed grid and to locate the interface thanks to an auxiliary phase function such as Volume Of Fluid or Level Set functions [95]. The concept that disconnects the interface motion and the mesh used to solve the conservation equations is called fictitious domain approach [60, 87]. Indeed, from the motion equation point of view, the interface is not known, only its presence is taken into account thanks to a volume auxiliary function. In these approaches, the interface tracking and the associated building of the phase function is of primary importance.

As proposed in [109], incompressible two-phase flows involving a carrier fluid and a solid phase can be modeled on a fixed mesh with fictitious domain approaches by considering the incompressible Navier-Stokes equations together with a phase function C describing the particle phase shape evolutions through an advection equation on the corresponding phase function. As explained by Kataoka [59] for fluid/fluid two-phase flows and Vincent [109] for particle flows, the resulting model takes implicitly into account the coupling between different phases separated by resolved interfaces, *i.e.* larger than the mesh cell size. The motion equations reads

$$\nabla \cdot \mathbf{u} = 0 \quad (3.1)$$

$$\rho \left(\frac{\partial \mathbf{u}}{\partial t} + (\mathbf{u} \cdot \nabla) \mathbf{u} \right) = -\nabla p + \rho \mathbf{g} + \nabla \cdot \left[\mu (\nabla \mathbf{u} + \nabla^t \mathbf{u}) \right] + \mathbf{F}_{si} + \mathbf{F}_m \quad (3.2)$$

$$\frac{\partial C}{\partial t} + \mathbf{u} \cdot \nabla C = 0 \quad (3.3)$$

where \mathbf{u} is the velocity, p the pressure, t the time, \mathbf{g} the gravity vector, ρ and μ respectively the density and the viscosity of the equivalent fluid. The two-way coupling between particle and fluid motions is ensured in the momentum equations by the presence of a solid interaction force \mathbf{F}_{si} [17, 74] which is not considered in the present work as only fixed particles are dealt with. The source term \mathbf{F}_m , given by 'Eq. 3.23', is used to impose a flow rate to the fluid if required, for example when

pipe flows are considered.

The one-fluid model is almost identical to the classical incompressible Navier-Stokes equations, except that

- the local properties of the equivalent fluid (ρ and μ) depend on C . In the present work, an arithmetic average is used for density ($\rho = C\rho_s + (1 - C)\rho_f$) and an harmonic average is considered for viscosity $\left(\mu = \frac{\mu_s\mu_f}{C\mu_f + (1 - C)\mu_s}\right)$ [109].
- the interface localization requires the solving of an additional equation on C . Instead of solving this equation on the Eulerian mesh, which is source of numerical diffusion or tearing of interfaces, a Lagrangian representation is preferred. A specific mesh (linear elements in 2D and set of triangles in 3D) is considered for the particle surface S . Equation (3.3) is reformulated as $\frac{d\mathbf{X}_b}{dt} = \mathbf{V}_p$, with \mathbf{X}_b the centroid of the spherical particle and \mathbf{V}_p the velocity of the particle interpolated with surrounding Eulerian velocities coming from the solving of equations (3.1-3.2). The approximation of the Lagrangian tracking of \mathbf{X}_b is detailed in [109]. Once \mathbf{X}_b is known, the position of each particle surface mesh element is also known. The phase function C is automatically build by projecting the Lagrangian particle mesh onto the Eulerian mesh [95]. For non-spherical particles the rotational motion has to be considered. It is for example solved with Quaternions [41]. In the present work, only fixed arrangements of particles are dealt with. As a consequence, the Lagrangian particle tracking is not considered even if the Lagrangian mesh for representing particles is used to calculate forces.

Satisfying the incompressible and solid constraints in fluid and particles requires developing a specific model. Two penalty approaches are proposed and detailed in the next section 3.3 to tackle with these constraints.

3.2.2 Penalty methods

As explained in the previous section 3.1, the one-fluid model and the fictitious domain approach formulated for dealing with particle flows require to consider each different phase (fluid, solid) as a fluid domain with specific material properties (density and viscosity for an isothermal flow). Each sub-domain is located by a phase function C .

In addition to local physical characteristics of the fluid that change over time due to particle motion, the local constraints that have to be fulfilled change potentially at each time step. Indeed, a given point or cell can be inside a fluid zone at time $n\Delta t$ and can be solid at the next time step $(n+1)\Delta t$. Here, n is the time index and Δt the associated time step. Two different numerical methods are used to satisfy in a coupled way and at the same time the fluid incompressibility and the solid behavior:

- Ensuring the solid behavior in the solid zones where $C = 1$ requires to define a specific rheological law for the rigid fluid part without imposing the velocity, as the particle velocities are not always known *a priori* in particulate motions (particle sedimentation, fluidized beds, turbulence particle interaction). A specific model is implemented for handling the solid particle behavior in the one-fluid Navier-Stokes equations. It is based on a decomposition of the viscous stress tensor and on a penalty method that acts on the viscosity which tends to large values in the particles [20] to implicitly impose the solid behavior and also the coupling between fluid and solid motion. For fixed particles, the velocity of the cell containing the centroid of the particle is imposed equal to zero. The viscous penalty method propagates the zero velocity in the whole solid medium.
- Following a similar walkthrough as in the work on Stokes and Navier-Stokes equations proposed by Fortin and Glowinski [45], an augmented Lagrangian method is applied to the unsteady Navier-Stokes equations dedicated to particulate flows. The main objective is to deal with the coupling between velocity and pressure and to satisfy the fluid and solid constraints at the same time. Starting with $\mathbf{u}^{*,0} = \mathbf{u}^n$ and $p^{*,0} = p^n$, the augmented Lagrangian solution reads
 while $\|\nabla \cdot \mathbf{u}^{*,m}\| > \epsilon$, solve

$$\begin{aligned}
 & (\mathbf{u}^{*,0}, p^{*,0}) = (\mathbf{u}^n, p^n) \\
 & \rho^n \left(\frac{\mathbf{u}^{*,m} - \mathbf{u}^{*,0}}{\Delta t} + \mathbf{u}^{*,m-1} \cdot \nabla \mathbf{u}^{*,m} \right) - \nabla(r \nabla \cdot \mathbf{u}^{*,m}) \\
 & = -\nabla p^{*,m-1} + \rho^n \mathbf{g} + \nabla \cdot [\mu^n (\nabla \mathbf{u}^{*,m} + \nabla^T \mathbf{u}^{*,m})] + \mathbf{F}_{si} + \mathbf{F}_m \\
 & p^{*,m} = p^{*,m-1} - r \nabla \cdot \mathbf{u}^{*,m}
 \end{aligned} \tag{3.4}$$

where r is an augmented Lagrangian parameter used to impose the incompressibility constraint, m is an iterative convergence index and ϵ a numerical threshold controlling the constraint. The augmented Lagrangian method is a kind of penalty technique: if $r \rightarrow +\infty$, the incompressibility is imposed but the solving of the linear system is difficult with iterative solvers while $r \rightarrow 0$ does not act on the fluid constraint and keeps the conditioning of the matrix unchanged. Usually, a constant value of r is used, for example equal to the average between the minimum and maximum eigenvalues of the linear system for Stokes flows [45]. From numerical experiments, optimal values are found to be of the order of ρ_i and μ_i in each phase (fluid or solid) to accurately solve the motion equations in the related zone [108, 110]. Algebraic improvements have also been proposed by Vincent [111] to automatically estimate the local values of r . In the present work, a constant value of r will be used.

The penalty method has been validated on numerous analytical and experimental reference solutions in [20, 34, 77, 87, 109, 110, 111].

3.2.3 Discretization schemes and solvers

The schemes and solvers used in the present work are detailed in [109]. The mass and momentum conservation equations, containing the viscous and augmented Lagrangian penalty terms, are discretized with implicit finite volumes on structured staggered meshes. The time derivative is approximated with a first or second order Euler scheme while the inertial, viscous and augmented Lagrangian terms are discretized with a second-order centered scheme. All fluxes are written at time $(n + 1)\Delta t$, except the non-linear inertial term that is linearized at first or second order as follows

- $\mathbf{u} \cdot \nabla \mathbf{u} \approx \mathbf{u}^n \cdot \nabla \mathbf{u}^{n+1}$ for first order linearization
- $\mathbf{u} \cdot \nabla \mathbf{u} \approx (2\mathbf{u}^n - \mathbf{u}^{n-1}) \cdot \nabla \mathbf{u}^{n+1}$ for second order Adams-Bashforth like linearization

The obtained linear system is solved with a BiCGSTAB II iterative solver [48], preconditioned with a Modified and Incomplete LU approach [39]. All the code is working on massively parallel computers by using MPI devices and exchanges [109]. As an example, the simulation of the bidisperse case presented in section 3.5.2, with $Re = 100$, $\alpha_d = 0.15$ and a 170^3 mesh, takes 2 days of CPU time on 216 processors to reach the steady state after 10000 iterations. These results have been obtained on intel (r) IVYBRIDGE 2.8 GHz processors.

3.3 Lagrangian extrapolation of forces for immersed boundary methods

The drag force due to the fluid-solid interaction at a surface S of the solid phase is:

$$\mathbf{F}^D = \mathbf{F}_p + \mathbf{F}_v \tag{3.5}$$

where the pressure force \mathbf{F}_p and the viscous force \mathbf{F}_v are:

$$\mathbf{F}_p = \oint_S -p \mathbf{n} \, dS \tag{3.6}$$

$$\mathbf{F}_v = \oint_S 2\mu \bar{\bar{\epsilon}} \cdot \mathbf{n} \, dS \tag{3.7}$$

Here, $\bar{\bar{\epsilon}}$ is the fluid strain tensor.

The computation of these forces consists in discretizing S on a set of N elements (triangles in $3d$ and segments in $2d$) called Lagrangian mesh (see figure 3.1), such that:

$$\mathbf{F}_p \approx \sum_l^N -p_l \mathbf{n}_l \, dS_l \tag{3.8}$$

$$\mathbf{F}_v \approx \sum_l^N 2\mu \bar{\bar{\epsilon}}_l \cdot \mathbf{n}_l \, dS_l \tag{3.9}$$

where p_l , $\bar{\epsilon}_l$ and \mathbf{n}_l are respectively the pressure, strain tensor and outgoing normal vector at the center \mathbf{C}_l of the l^{th} element of the Lagrangian mesh as illustrated in figure 3.1. Normal \mathbf{n}_l and element surface dS_l are deduced from the coordinates of the nodes constituting the l^{th} element.

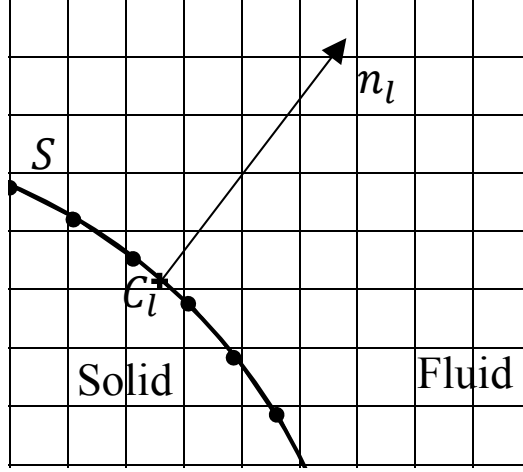


Figure 3.1: Details of a 2D discretization of the particle surface S used in drag force computation

3.3.1 Low order naive approach

Given that the pressure field p and the viscous stress tensor $\bar{\epsilon}$, used in the drag force computation, are known on the Eulerian mesh and not on the Lagrangian mesh as explained above, the naive approach to overcome this problem consist in interpolating them from the Eulerian mesh on the Lagrangian mesh using a second order Taylor interpolation detailed in Appendix 1 (3.7).

To validate this approach, we compute the drag force exerted by a uniform Stokes flow ($Re = 10^{-3}$) on an isolated cylinder (2D) and an isolated sphere (3D), as detailed below.

Uniform Stokes flow past a cylinder

According to [13], a uniform Stokes flow ($Re = 10^{-3}$) past a cylinder of diameter $d = 2m$, with the undisturbed velocity being noted $U_\infty = 1m/s$, is solution of the Brinkman equation $-\nabla p + \mu \Delta \mathbf{u}_i - \frac{\mu}{K} \mathbf{u}_i = 0$. In the polar coordinate frame (r, θ) centered on the particle, it reads:

$$\mathbf{u}^*(r^*, \theta) = \begin{cases} \frac{1}{r^*} \left(- \left(1 + \frac{2K_1(\lambda)}{\lambda K_0(\lambda)} \right) \frac{1}{r^*} + r^* + \frac{2}{\lambda K_0(\lambda)} K_1(\lambda r^*) \right) \cos \theta \\ - \left(1 + \left(1 + \frac{2K_1(\lambda)}{\lambda K_0(\lambda)} \right) \frac{1}{(r^*)^2} - \frac{2}{K_0(\lambda)} \left(K_0(\lambda r^*) + \frac{K_1(\lambda r^*)}{\lambda r^*} \right) \right) \sin \theta \end{cases} \quad (3.10)$$

$$p^*(r^*, \theta) = \frac{2}{Re} \lambda^2 \left(- \left(1 + \frac{2K_1(\lambda)}{\lambda K_0(\lambda)} \right) \frac{1}{r^*} - r^* \right) \cos \theta \quad (3.11)$$

The corresponding drag force is:

$$\mathbf{F}^D = \frac{2\pi}{Re} \left(2\lambda^2 + 4 \frac{\lambda K_1(\lambda)}{K_0(\lambda)} \right) \mathbf{e}_x \quad (3.12)$$

where $\mathbf{u}^* = \frac{\mathbf{u}}{U_\infty}$, $p^* = \frac{p}{\rho U_\infty^2}$, $r^* = \frac{2r}{d}$, $\rho = 1kg.m^{-3}$ is the fluid density, $\lambda = \frac{d^2}{4K}$ is the dimensionless permeability of the porous medium in Brinkman sens, K is the permeability of the porous cylinder, K_0 and K_1 are the modified Bessel functions of rank 0 and 1. For $K \rightarrow 0$, the porous cylinder can be likened to an impermeable solid particle.

Uniform Stokes flow past a sphere

For the uniform flow past a sphere in Stokes regime, the velocity and pressure are [11] :

$$\mathbf{u}(x, y, z) = \begin{cases} U_\infty - \frac{3}{4} \left(\frac{d}{2} \right) U_\infty \left(\frac{x^2}{r^3} + \frac{1}{r} \right) + \frac{3}{4} \left(\frac{d}{2} \right)^3 U_\infty \left(\frac{x^2}{r^5} - \frac{1}{3r^3} \right) \\ \frac{3}{4} U_\infty \left(\frac{(\frac{d}{2})^3}{r^5} - \frac{(\frac{d}{2})}{r^3} \right) xy \\ \frac{3}{4} U_\infty \left(\frac{(\frac{d}{2})^3}{r^5} - \frac{(\frac{d}{2})}{r^3} \right) xz \end{cases} \quad (3.13)$$

$$p = -\frac{3}{4} \mu d U_\infty \frac{x}{r^3} \quad (3.14)$$

where $r = \sqrt{x^2 + y^2 + z^2}$.

The drag force is analytically given by:

$$\mathbf{F}^D = 3\pi \mu d U_\infty \mathbf{e}_x \quad (3.15)$$

Simulations setup

The computational domain used to simulate a uniform Stokes flow past a cylinder (resp. a sphere) is a square (resp. a cube) of a Length $L = 2d$, and the spatial discretization, using a regular Cartesian grid called Eulerian mesh, is represented by the number of grid cells across the diameter of the particle $D_m = \frac{d}{\Delta x} = 20$. The exact solution (3.10), (3.11) (resp. (3.13), (3.14)) for a Stokes flow past a cylinder (resp. a sphere) was implemented at boundary conditions to be able to simulate such a flow in a numerically small domain not extending to infinity as Stokes flow would require. Practically, the considered simulation domain is two particle diameter long in each space direction.

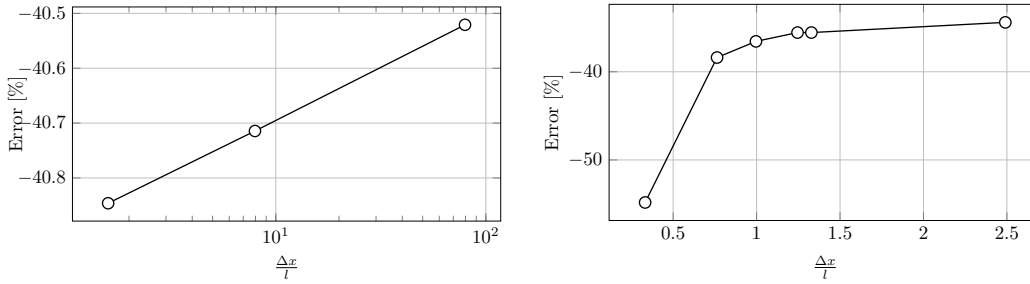


Figure 3.2: Drag force relative error (%) for the Stokes flow past a cylinder (left), and the Stokes flow past a sphere (right) in terms of Lagrangian mesh refinement - the force is computed with the naive 2^{nd} order Taylor interpolation method. The size of the Lagrangian particle surface mesh element is l while the size of the Cartesian Navier-Stokes mesh is Δx .

Results

Figure 3.2 shows that the computation of the drag force with a naive approach is not accurate, the error being about at least 40% even if the surface Lagrangian mesh is refined. This is due to the use of pressure and strain tensor values in the cells containing the fluid-solid interface where the error with the analytic solution is the highest, as illustrated in figure 3.3 for the uniform flow past a cylinder ($2D$) and a sphere ($3D$). This error is due to the fact that the physical characteristics (μ, ρ) in the mixed fluid-solid cells are the average between those of the fluid and those of the solid.

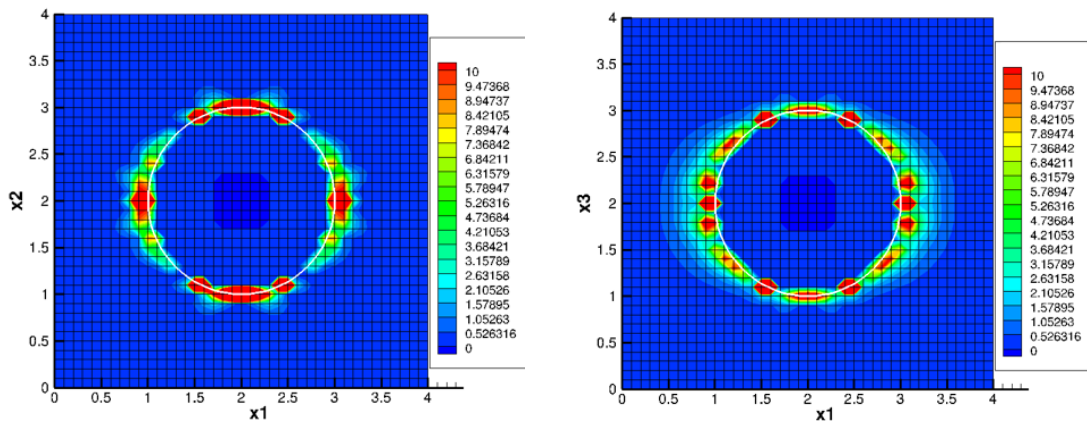


Figure 3.3: Relative error (%) of the first component of velocity for Stokes flow past cylinder (left) and Stokes flow past sphere (right) in the whole domain

To prevent the use of wrong pressure and velocities in the cells cut by the fluid-particle interface, we have to extrapolate the pressure and the strain tensor from the

fluid area far from the particle to the interface. To do so, a Lagrange extrapolation is considered, as detailed below. The same contamination of the flow field is expected with standard IBM methods [105, 116]. To preclude this drawback in IBM method, extrapolation techniques were proposed by [116] in the force computation, with a lower order as what is explained in the next section 3.4. Another approach is the PUReIBM [103] that avoid the contamination of the fluid nodes in the Eulerian cells cut by the interface, allowing a direct interpolation of the stress tensor.

3.3.2 New high order method based on Lagrange extrapolation

Given a function $f : X \in \mathbb{R}^3 \rightarrow \mathbb{R}$ and a set of k points $\mathbf{P}_i, i = 1..k$, the k^{th} Lagrange extrapolation of f at point \mathbf{C}_l is given by:

$$f(\mathbf{C}_l) = \sum_{i=1}^k f(\mathbf{P}_i)L_i(\mathbf{C}_l) \quad , \text{ where } \quad L_i(\mathbf{C}_l) = \prod_{j \neq i}^k \frac{|\mathbf{C}_l - \mathbf{P}_j|}{|\mathbf{P}_i - \mathbf{P}_j|} \quad (3.16)$$

The k^{th} order of the drag force computation consists now of interpolating (using the k^{th} order Taylor interpolation detailed in Appendix 1) the pressure and the strain tensor on k \mathbf{P}_i fictitious points built along the normal (see figure 3.4 for third order), and then using the k^{th} order Lagrange extrapolation (3.16) to compute them at \mathbf{C}_l . With (3.5), (3.8), (3.9), the friction force exerted by the fluid on the particle can be calculated.

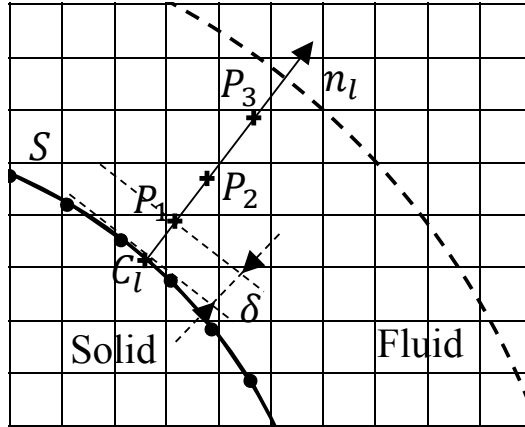


Figure 3.4: Details of third order Lagrange extrapolation used in drag force computation

In figure 3.4, points P_1, P_2 and P_3 are the fictitious points used in third order Lagrange extrapolation of the pressure and viscous components of the force on the particle surface. The zone between the particle surface S (solid line) and the dash line corresponds to the Eulerian discrete points that have an influence on the force calculation. Parameter δ is the minimum distance between the first fluid point and S that is required to obtain a correct force estimate.

Note that the order of the drag force computation may not be the same on all the Lagrangian mesh element. Indeed the choice of the computation order located at the centre \mathbf{C}_l of each Lagrangian mesh element is governed by the fact that all the points used in the Lagrange extrapolation and the Taylor interpolation have to be fully fluid, *i.e.* the fluid-phase indicator function $C = 0$ on these points. When two particles are close, the drag force computation order is adapted for each Lagrangian mesh cell in a way that no extrapolation or interpolation point belongs to a neighboring sphere. If one of these points is located in a solid zone, the order of drag force computation is downgraded until all the calculation points belongs to the fluid. At least an order 1 is considered.

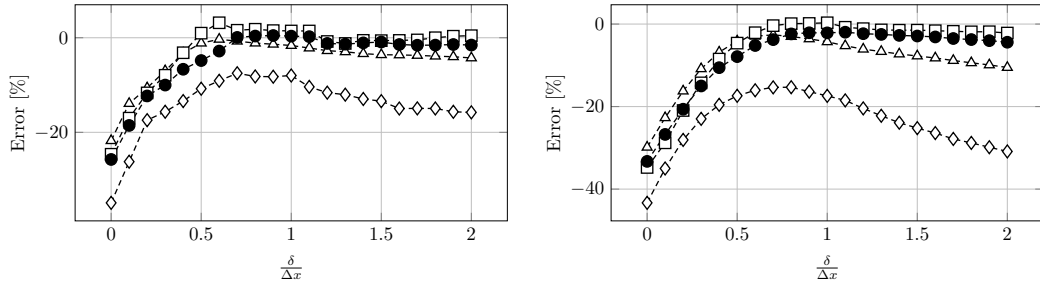


Figure 3.5: Drag force relative error (%) according to extrapolation distance δ (written in Δx unit) for the Stokes flow past a cylinder (left) and the Stokes flow past a sphere (right) at different order: (\diamond) first, (\triangle) second, (\bullet) third, and (\square) fourth orders are plotted.

Considering that the pressure and strain tensor have to be extrapolated from the nearest fluid region in the vicinity of the particle, where the physical characteristics belong to the fluid, to the interface region where the drag force is computed, the first step consists in increasing the distance δ (see figure 3.4) until the computation of the force is accurate enough. As illustrated in figure 3.5, the minimum error is reached for $\delta = \Delta x$ and remains stable for the third and fourth order Lagrange interpolation, for both simulations, namely the Stokes flow past a cylinder (left), and past a sphere (right). This conclusion holds for our method and probably for all the methods that contaminate the fluid cells cut by the interface. Different behavior would certainly be observed with PURE-IBM [103]. To limit the computational effort while keeping a good accuracy, the third order force computation with $\delta = \Delta x$ will be considered thereafter as it requires less computational effort. The errors obtained with the new high order force calculation method are reported in figure 3.6. Compared to the naive approach, the error levels for both cylinder and sphere cases are now always less or around 2% as soon as the local size of the Lagrangian surface mesh elements is comparable to Δx . Thanks to the novel force estimate, the error has been reduced by a factor of 20. In the rest of the work, the value of δ will be chosen to be Δx if not specified.

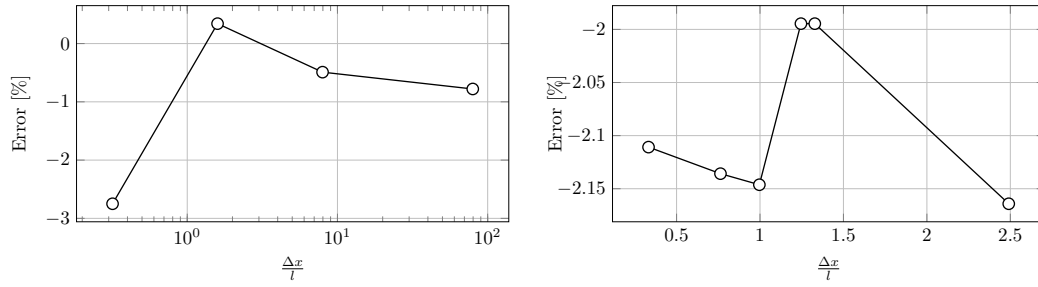


Figure 3.6: Drag force relative error (%) for the Stokes flow past a cylinder (left) and the Stokes flow past a sphere (right) in term of the Lagrangian mesh refinement l : force computed using 3^{rd} Lagrange extrapolation and 2^{nd} order Taylor interpolation

3.4 Validation on flows interacting with an isolated particle

3.4.1 Drag coefficient

For validation purpose, the force acting on a particle and in particular the corresponding drag coefficient is recalled. It is defined as [31]:

$$C_d = \frac{|\mathbf{F}^D|}{\frac{1}{2}\rho\tilde{U}^2 A_p} \quad (3.17)$$

where $\tilde{U} = |U_\infty \mathbf{e}_x - \mathbf{U}_p|$ is the relative velocity between the particle and the fluid velocity at infinity, $U_\infty \mathbf{e}_x$ is fluid velocity in the mean flow direction far from the particle, \mathbf{U}_p is the particle velocity, ν is the fluid kinematic viscosity and $A_p = \frac{\pi}{4}d^2$ the cross-sectional area of the particle.

The drag coefficient is dependent on the flow regime determined by the Reynolds number:

$$Re = \frac{\tilde{U}d}{\nu} \quad (3.18)$$

The drag coefficient in Stokes regime, *i.e.* when $Re \rightarrow 0$, is:

$$C_d = \frac{24}{Re} \quad (3.19)$$

The correlation of drag coefficient for a finite Reynolds number, proposed by Schiller & Naumann [97] is:

$$C_d = \frac{24}{Re} \left(1 + 0.15 Re^{0.687}\right) \quad (3.20)$$

3.4.2 Simulations setup

The computational domain is first chosen, its lengths being $L_x = 16d$ and $L_y = L_z = 8d$ in each Cartesian direction. The Eulerian mesh refinement is constant in a box of

extension $[(2d, 3d, 3d); (6d, 5d, 5d)]$ centered around the particle position. Outside this box, the Eulerian mesh is exponentially coarsen from the box to the boundaries of the simulation domain. Accurate drag force calculation needs properly resolved boundary layers around the particle. It is expected that a 5 cell resolution in the boundary layer thickness will be enough at least for the range of Reynolds numbers studied in the present article. This choice is also consistent with the compact support of cells needed to get third order Lagrange extrapolation accuracy (see figures 3.4 3.25). A numerical study of the Eulerian mesh effect was conducted to assess this assumption (see figure 3.7). It can be observed that the error stabilizes for $\frac{d}{\sqrt{Re}} \geq 5$ which is in accordance with the choice made for the Eulerian mesh criteria. This gives $\frac{d}{\sqrt{Re}} = 5\Delta x$ according to scaling laws for laminar dynamic boundary layers. Therefore, in the box surrounding the particle, the minimum cell size is:

$$\Delta x = \frac{d}{5\sqrt{Re}} \quad (3.21)$$

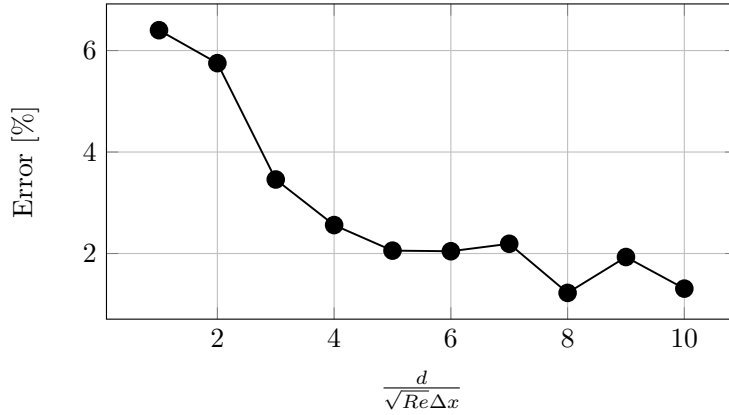


Figure 3.7: Drag force relative error (%) for the uniform flow past sphere at $Re = 100$ as function of the number of Eulerian cells in the boundary layer.

The Eulerian meshes used in all simulated cases of the present work will fulfill (3.21). The inlet boundary conditions is $\mathbf{u} = U_\infty \mathbf{e}_x$ (see figure 3.8) and Neumann conditions are applied elsewhere.

3.4.3 Study of numerical parameters for the Lagrange extrapolation

As an extension of the work carried out for the Stokes regime, we have performed the same kind of study for a higher finite Reynolds number $Re = 100$ when inertial effects are important. The effect on the drag force computation of the distance δ between the particle interface points \mathbf{C}_l and the first Eulerian mesh extrapolation point P_1 has been considered. The role played by the Lagrangian mesh refinement have also been analyzed. Unlike the stokes flow there is no analytical results for

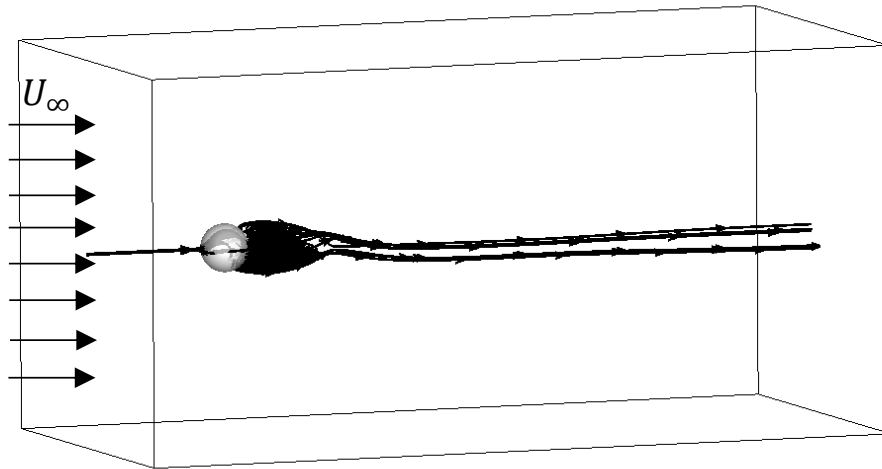


Figure 3.8: Illustration of instantaneous stream lines obtained for a uniform flow past an isolated sphere at $Re=290$. The upstream unperturbed velocity U_∞ is imposed at the left boundary condition.

drag force at higher Reynolds number, therefore the error here is estimated with respect to Schiller & Naumann [97] correlation.

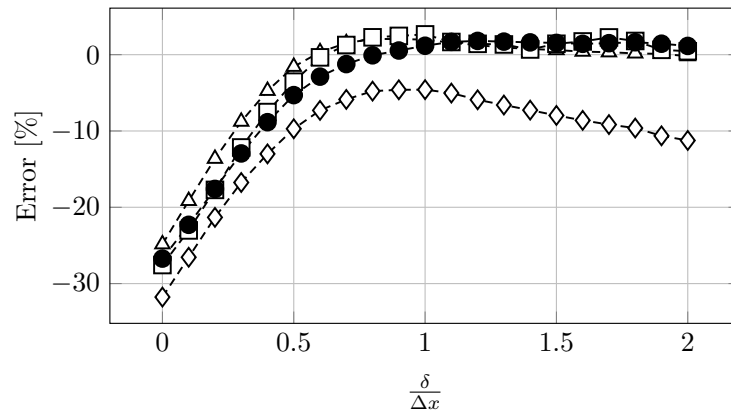


Figure 3.9: Drag force relative error (%) for the uniform flow past sphere at $Re = 100$. Different orders of Lagrange extrapolation are considered: (\diamond) first, (\triangle) second, (\bullet) third, and (\square) fourth order. The distance between the first Eulerian point used to extrapolate forces and the particle surface is δ .

One can observe in figure 3.9 a similar behaviour of error as already found for Stokes flows (the reader can refer to figure 3.5 right) indicating that in this range, Reynolds number have little influence on drag force errors at least for 2^{nd} , 3^{rd} and 4^{th} order Lagrange extrapolations. To conclude on the distance between Eulerian interpolation points and particle surface, as soon as $\delta \geq \Delta x$, the error on drag force calculation is less than 2% for 3^{rd} and 4^{th} order Lagrange extrapolation in

Stokes and Navier-Stokes regimes. In this case, a 3^{rd} order Lagrange extrapolation is considered, as being a good compromise between implementation complexity, calculation time and accuracy.

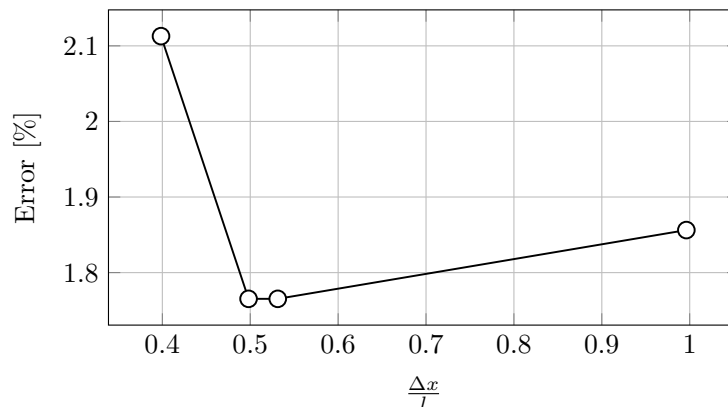


Figure 3.10: Drag force relative error (%) according to Lagrangian surface element size l for uniform flow past sphere at $Re = 100$.

As illustrated in figure 3.10, the Lagrangian mesh refinement does not affect a lot the drag force computation as soon as the Lagrangian particle surface element size l is of the order of Δx . For $Re = 100$, the error is around 2% on the drag force calculation.

In the rest of the present work, the 3^{rd} order Lagrange extrapolation will always be used together with $l = \Delta x$.

3.4.4 Result on the drag coefficient

The transition area between axisymmetric flow and non-axisymmetric vortex shedding regime being around $Re = 300$, for a uniform flow past a fixed isolated sphere, we have conducted several simulations for Reynolds numbers up to 290 ($Re = 0.1, 1, 10, 20, 40, 60, 80, 100, 150, 200, 250, 290$). In each case, the simulations are stopped when the steady state of the flow is reached. The drag coefficient obtained at the final step of each simulation is compared to the correlations (3.19) and (3.20). Figure 3.11 shows a very good agreement of the numerically calculated drag coefficient compared to the correlation of Schiller & Naumann [97]. This test case provides an interesting validation of the force calculation for a single particle.

3.4.5 Pressure coefficient

The analysis of local pressure profiles can give insight into the pressure behavior depending on the Reynolds number. The local pressure coefficients are defined by equation (3.22) in a spherical coordinate system (see figure 3.12). They are considered along the azimuthal angle θ as follows:

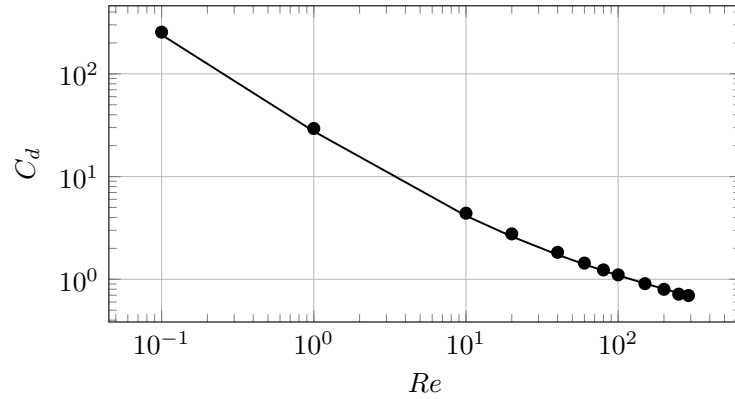


Figure 3.11: Drag coefficient for uniform flow past sphere at different Reynolds number: (—) Schiller & Naumann [97], (●) present work.

$$C_p(\theta) = \frac{p(\theta)}{\frac{1}{2}\rho U_\infty^2} \quad (3.22)$$

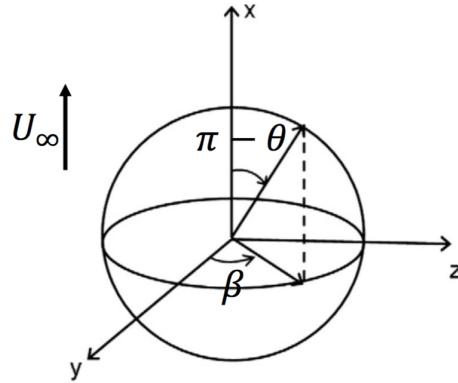


Figure 3.12: Spherical coordinate system around a particle. The flow direction is represented by the undisturbed velocity U_∞ .

The pressure coefficient distribution according to θ is compared for $Re = 1, 10, 100$ to some available body fitted simulations results conducted by Magnaudet [68], Dennis & Walker [38], LeClair *et al.* [30] and Massol [70]. The results are presented in figure 3.13. It can be observed that a very good agreement is found between our force calculations and reference results. We can observe that the local pressure profile is symmetric with respect to $\theta = 90$ for $Re = 1$ as shown in figure 3.13 a) and become increasingly asymmetric while increasing the Reynolds number in figures 3.13 b) and c). This feature of the flow is clearly highlighted for $Re = 10$ where the local pressure profile is no more symmetric with a negative pressure region that took place after $\theta = 60$. For $Re = 100$, the same conclusion holds where the negative pressure region appears at $\theta = 50$.

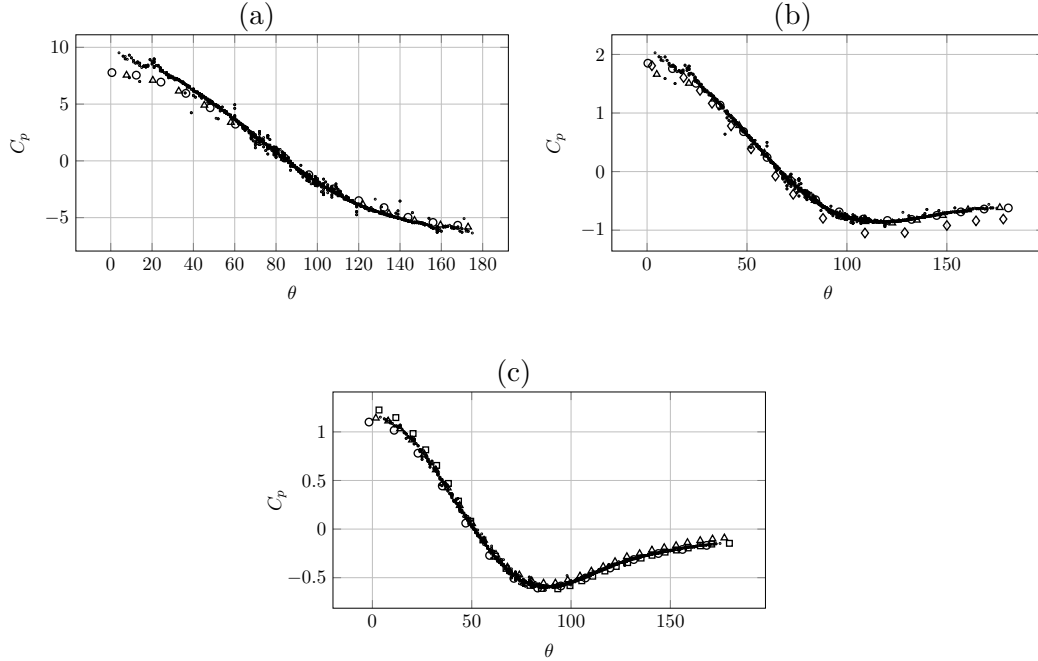


Figure 3.13: Pressure coefficient for a uniform flow past an isolated sphere at (a) $Re = 1$, (b) $Re = 10$, (c) $Re = 100$: (\diamond) Dennis *et al.* [38], (\triangle) Magnaudet *et al.* [68], (\circ) LeClair *et al.* [30], (\square) Massol [70], and (\cdot) present work

3.5 Forces in fixed arrangements of spheres

In the previous section 3.4, we have exhibited various successful validations of the force calculation for uniform flows past a fixed isolated sphere. We can now confidently complexify the simulated particulate motion by investigating a flow past fixed particle assemblies which corresponds to a gas-solid flow with high Stokes number. Two way are possible to set up a uniform flow past fixed packed particles:

- by imposing a constant pressure gradient in the domain. In this configuration, the mean fluid velocity $\langle \mathbf{u}_f \rangle = \frac{\int_V (1 - C) \mathbf{u} dV}{\int_V (1 - C) dV}$ evolves to reach a steady state corresponding to the imposed pressure gradient.
- by choosing a desired mean fluid velocity $\langle \mathbf{u}_f \rangle = \mathbf{u}_d$, and so a desired Reynolds number. A source term

$$\mathbf{F}_m = -\rho \frac{\langle \mathbf{u}_f \rangle - \mathbf{u}_d}{\Delta t} + \frac{\sum_i^{N_p} \mathbf{F}_i^D}{V_f} \quad (3.23)$$

is inserted in the momentum conservation equations. It is adjusted until the desired Reynolds number is reached. This is the method used in this work. Its main advantage is to be able to simulate a prescribed Reynolds number without a trial and error procedure unlike to what is require in the pressure gradient technique.

Two ways to distribute the particles are studied in this work: a Face-Centered Cubic arrangement of spheres for both mono and bi-dispersed flows, and random assemblies of spheres only for mono-dispersed flows.

The particulate Reynolds number $Re = \frac{|\langle \mathbf{u}_f \rangle| d}{\nu}$ is used studying the Face-Centered Cubic arrangement of spheres following the work of Massol [70]. On the other hand, in the random assemblies of spheres, another Reynolds number based on the superficial velocity $(1 - \alpha_d)|\langle \mathbf{u}_f \rangle|$ is considered to take into account the solid loading in the characterization of the flows [12, 103]. It is given by:

$$Re_S = \frac{(1 - \alpha_d)|\langle \mathbf{u}_f \rangle| d}{\nu} \quad (3.24)$$

The relation between the solid volume fraction α_d and the number of particle N_p is:

$$N_p = \frac{6}{\pi} \left(\frac{L}{d} \right)^3 \alpha_d \quad (3.25)$$

As for the uniform flow past an isolated sphere, the grid resolution is fixed by imposing 5 Cartesian cells in the boundary layer as $\Delta x = \frac{d}{5\sqrt{Re_S}}$.

The mean non-dimensional drag force for all the particles is then defined as:

$$F = \frac{|\langle \mathbf{F}^D \rangle|}{3\pi\mu d(1 - \alpha_d)|\langle \mathbf{u}_f \rangle|} \quad (3.26)$$

with $\langle \mathbf{F}^D \rangle = \frac{1}{N_p} \sum_i^{N_p} \mathbf{F}_i^D$, \mathbf{F}_i^D being the drag force computed over the i^{th} particle.

3.5.1 Monodispersed arrangements of spheres

3.5.1.1 Face-Centred Cubic periodic arrangement of spheres

A Face-Centered Cubic (FCC) array is a cube where three spheres are placed on the faces centers, and one sphere is located on the vertices with periodic boundary conditions, as illustrated in the figure 3.14.

This configurations was widely studied [51, 70, 103] to understand and separate the wake effects, observed when spheres are aligned along the flow direction, *i.e.* streamwise interactions, from the blocking effects, where the spheres are aligned along the direction perpendicular to the flow direction, *i.e.* lateral interactions. Two regimes, *i.e.* attached and separated flows, govern the uniform flow past a FCC array of spheres, depending on the Reynolds number and the solid volume fraction. They are considered below.

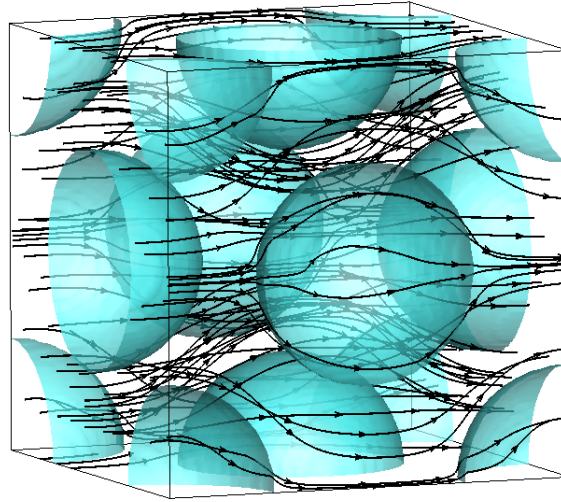


Figure 3.14: Streamlines of a steady flow along the x-axis of a Face-Centred Cubic array of spheres at $Re = 50$ and $\alpha_d = 0.5$. The particle shape is plotted in blue.

Regime 1: attached flows

For low Reynolds numbers, the boundary layer remains attached to the particles. Unlike the isolated sphere configurations, the boundary layer detachment occurs for higher Reynolds numbers when FCC arrays are considered, due to the blocking effect of the surrounding particles. In fact, the presence of lateral spheres speeds-up the flow between the spheres and blocks the detachment of the boundary layer. Figure 3.15 illustrates this regime for $Re = 50$, $\alpha_d = 0.15$. A very good agreement is observed for the pressure distribution over the spheres in both plans $\beta = 0^\circ$ and $\beta = 45^\circ$ as shown in figure 3.15(a) and 3.15(b), compared to the results of Massol [70] obtained with body fitted meshes. The same agreement is observed for the axial friction coefficient as illustrated in figure 3.15(c) and 3.15(d) for the plans $\beta = 0^\circ$ and $\beta = 45^\circ$, the spherical coordinates α and β are illustrated in the figure 3.12. It is worthwhile to note that the flow is non-axisymmetric even if all particles see the same flow due to the symmetry of the array and the periodicity of boundary conditions. Note that the pressure coefficient is known at the center of each Lagrangian element. The C_p value given on each β plan is that of the nearest Lagrangian element to the given plan.

Regime 2: separated flows downstream of the spheres

With increasing Reynolds numbers, a separation of the boundary layer occurs in the downstream hemisphere of the particles. As noticed for an isolated sphere, the recirculating zone length increases with the Reynolds number. The flow confinement due to the presence of the lateral particles is so significant that high speed jet flows are obtained between the particles. These jet flows impact the spheres onto the

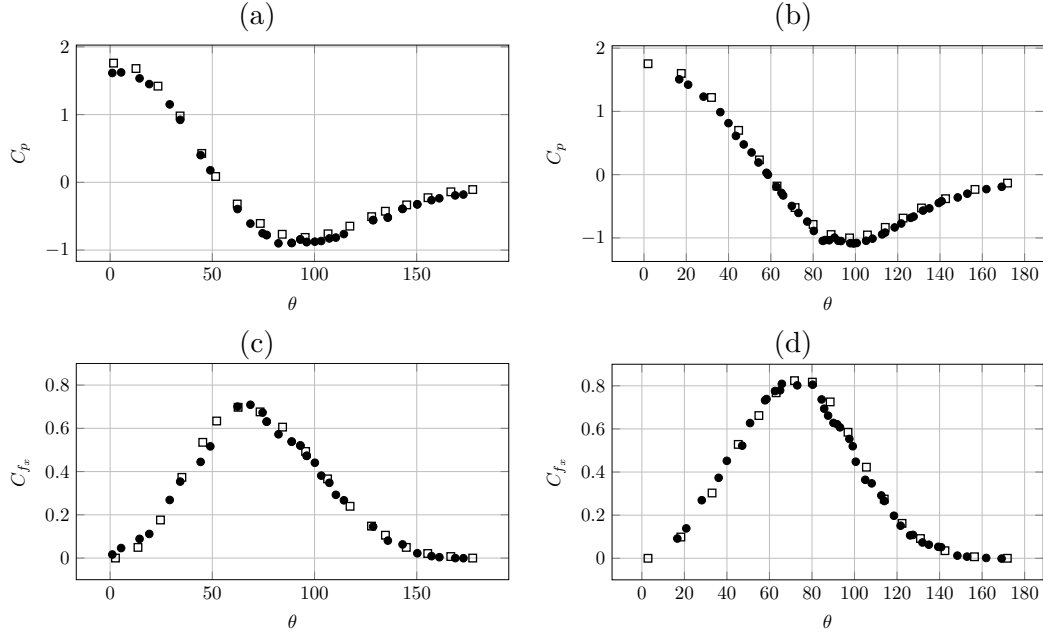


Figure 3.15: Pressure coefficient [(a) $\beta = 0$, (b) $\beta = 45$] and axial friction coefficient [(c) $\beta = 0$, (d) $\beta = 45$], for a uniform flow past a FCC at $Re = 50$, $\alpha_d = 0.15$: (\square) Massol [70], and (\bullet) present work

upstream hemisphere. As illustrated in figure 3.16(a), this mechanism induces the development of a fountain effect on the vertical plan $\beta = 0^\circ$, the direct consequence of which is that the maximum pressure is no longer at $\theta = 0^\circ$ but at $\theta = 36^\circ$. Note that the same result was found by Massol [70]. Figures 3.16(a) and 3.16(b) show again the good agreement of the pressure distribution on the vertical and lateral plans with the body fitted simulations of Massol [70], and the same conclusions is observed in the figures 3.16(c) and 3.16(d) for the axial friction coefficient distribution. It can be noticed that for this Reynolds number of 300, larger differences are observed between our force calculation and body fitted grid results, mostly in the vicinity of the pressure peaks in the $\beta = 0^\circ$ plans.

Drag force

The non-dimensional drag force F normalized by the isolated sphere non-dimensional drag force (given by Schiller & Naumann [97]) $F_s = \frac{1 + 0.15Re_S^{0.687}}{(1 - \alpha_d)^2}$, noted as $\frac{F}{F_s}$, is compared to existing literature results:

- Tenneti *et al.* [103]:

$$F_T = F_s + F_\phi + F_{\phi, Re_S} \quad (3.27)$$

$$F_\phi = \frac{5.81\phi}{(1 - \alpha_d)^2} + 0.48 \frac{\alpha_d^{\frac{1}{3}}}{(1 - \alpha_d)^3}$$

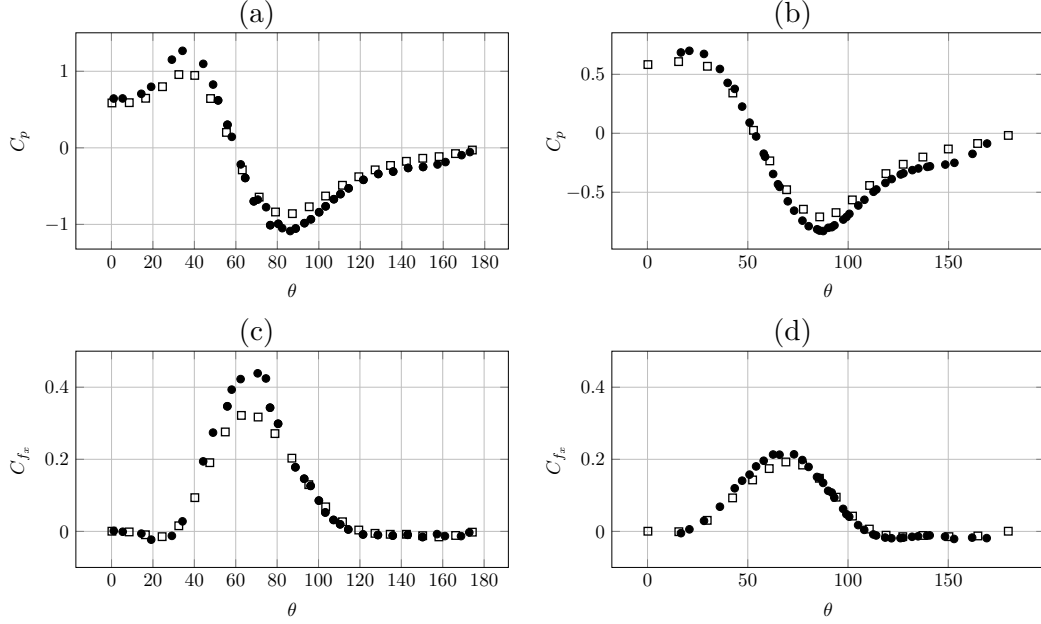


Figure 3.16: Pressure coefficient [(a) $\beta = 0$, (b) $\beta = 45$] and axial friction coefficient [(c) $\beta = 0$, (d) $\beta = 45$], for a uniform flow past a FCC at $Re = 300$, $\alpha_d = 0.15$: (\square) Massol [70], and (\bullet) present work

$$F_{\phi, Re_S} = (1 - \alpha_d) \alpha_d^3 Re_S \left(0.95 + \frac{0.61 \alpha_d^3}{(1 - \alpha_d)^2} \right)$$

- Gobin *et al.* [46]:

$$F_G = \begin{cases} F_{WY} & \text{if } \alpha_d \leq 0.3 \\ \min(F_{WY}, F_E) & \text{otherwise} \end{cases}$$

$$F_{WY} = F_s (1 - \alpha_d)^{-1.7} \quad \text{Wen \& Yu [114]}$$

$$F_E = \frac{150}{18} \frac{\alpha_d}{(1 - \alpha_d)^2} + \frac{7}{4} \frac{1}{18} \frac{Re_S}{(1 - \alpha_d)^2} \quad \text{Ergun [42]}$$

- Beetstra *et al.* [12]:

$$F_B = \frac{10 \alpha_d}{(1 - \alpha_d)^2} + (1 - \alpha_d)^2 (1 + 1.5 \sqrt{\alpha_d}) + \frac{0.413}{(1 - \alpha_d)^2} \frac{Re_S}{24} \frac{\frac{1}{(1 - \alpha_d)} + 3(1 - \alpha_d) \alpha_d + 8.4 Re_S^{-0.343}}{1 + 10^{3 \alpha_d} Re_S^{-0.5 - 2 \alpha_d}} \quad (3.28)$$

Our FCC results are compared to FCC results of Massol [70] and Randrianarivelo *et al.* [84]. Laws corresponding to random configurations are also considered, following the conclusion of Massol [70] that FCC arrangement of spheres provides a better agreement to random configurations compared to simple cubic, tetragonal

and centered cubic arrangements. These comparisons are presented in figure 3.17 at different Reynolds number $Re = 10$ figure 3.17(a), $Re = 50$ figure 3.17(b), $Re = 100$ figure 3.17(c) and $Re = 300$ figure 3.17(d). It can be observed that a nice match is found between our results and those of Massol [70] which was extracted from body fitted simulations and with those of Tenneti *et al.* [103] extracted from IBM simulations. Reasonable agreement is also observed with Gobin *et al.* [46], and Beetstra *et al.* [12] even if larger differences are noticed for $Re = 300$ with Beetstra's results *et al.* [12] which can be a consequence of insufficient Eulerian mesh resolution at that Reynolds number.

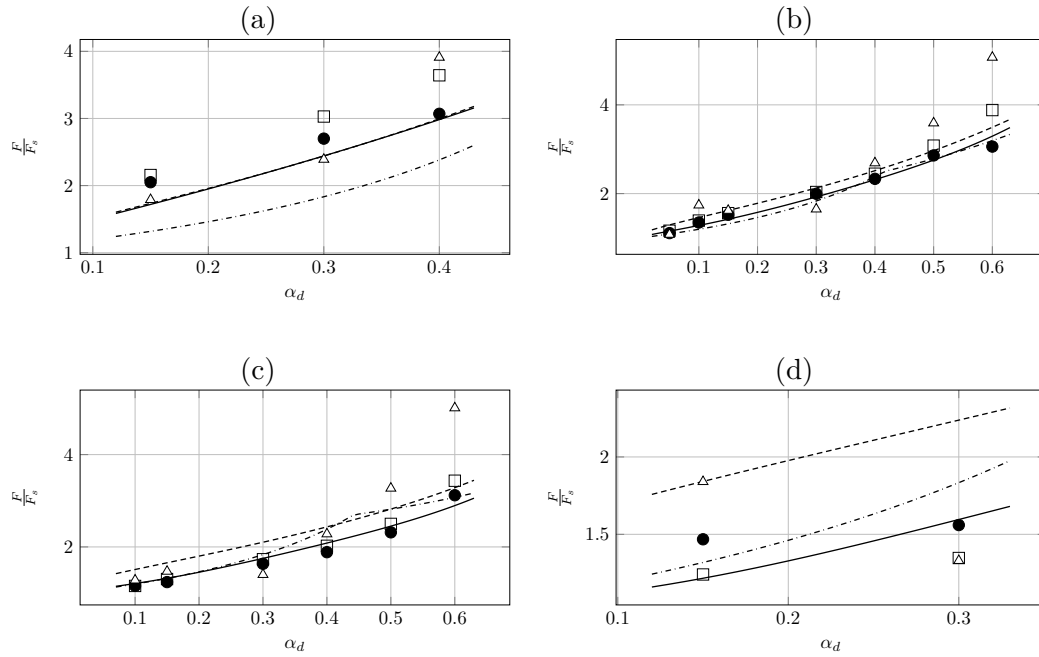


Figure 3.17: Drag force for a uniform flow past a FCC, normalized by Schiller & Naumann [97] drag force for a uniform flow past an isolated sphere. Results are presented as a function of the solid volume fraction α_d and Reynolds number (a) $Re = 10$, (b) $Re = 50$, (c) $Re = 100$, (d) $Re = 300$: (—) Tenneti *et al.* [103], (---) Gobin *et al.* [46], (· · ·) Beetstra *et al.* [12], (Δ) Randrianarivelo [84], (\square) Massol [70], and (\bullet) present work.

3.5.1.2 Random periodic arrangement of spheres

A new step is taken in the complexity of the problem by randomly distributing a set of spheres in a box for a given solid volume fraction. An illustration is given in figure 3.18 for $Re_S = 50$ and $\alpha_d = 0.3$. Following the work of Tenneti *et al.* [103] the box lengths are $L_x = L_y = L_z = 5d$ (d is the spheres diameter) which ensures simulations statistically converged in terms of number of spheres. The locations of the spheres are randomly drawn to distribute them in the domain until

the desired compacity is reached with no overlapping between the spheres. To simulate an infinite domain, periodic boundary conditions are specified in all directions.

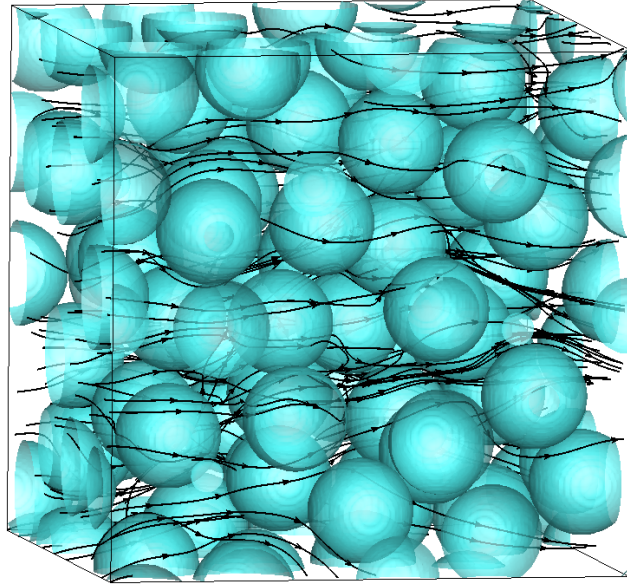


Figure 3.18: Random periodic arrangement of spheres, for $Re_S = 50$ and $\alpha_d = 0.3$ - The particle shape is plotted in blue while black lines represent streamlines.

To be statistically converged in terms of number of realizations, we performed for most cases five Multiple Independent Simulations (MIS), Tenneti *et al.* [103] conducted the same number of MIS to obtain their correlation for the drag force (due to CPU time requirements, 5 MIS were not conducted for all Reynolds numbers and solid fractions). Consequently, the representative non-dimensional drag force numerically obtained is an average of those calculated over the different realizations (MIS). Simulations with various solid volume fraction $\alpha_d = 0.1, 0.15, 0.2, 0.3$ have been investigated, together with different superficial Reynolds numbers ranging from 20 to 200.

The results presented in figure 3.19 demonstrate again a good global agreement of our results with existing correlations of Tenneti *et al.* [103], Gobin *et al.* [46] and Beetstra *et al.* [12] for each solid volume fractions studied here as shown in figures: 3.19(a) for $\alpha_d = 0.1$, 3.19(b) for $\alpha_d = 0.15$, 3.19(c) for $\alpha_d = 0.2$ and 3.19(d) for $\alpha_d = 0.3$, all function of the superficial Reynolds number. In all cases, for larger Re_S , the correlation of Beetstra *et al.* [12] is farther from other works.

The pressure profiles according to θ are given in figures 3.20 and 3.21. They have been obtained with our force calculation and our simulations. It can be noticed that the pressure contribution on the drag force increase with the solid volume fraction in both vertical plan $\beta = 0^\circ$ as illustrated in figure 3.20(a) and lateral plan $\beta = 45^\circ$ see figure 3.20(b). On the contrary, it seems that the Reynolds number

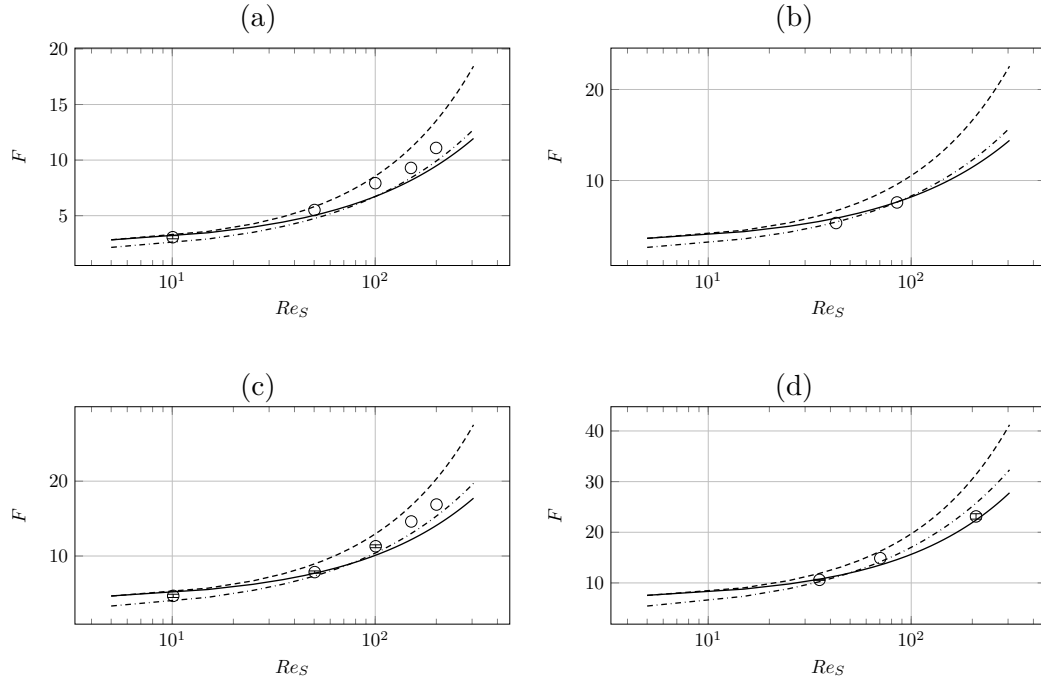


Figure 3.19: Normalized drag force for a uniform flow past random packed spheres as function of the superficial Reynolds number Re_S and solid volume fraction (a) $\alpha_d = 0.1$, (b) $\alpha_d = 0.15$, (c) $\alpha_d = 0.2$, (d) $\alpha_d = 0.3$: (—) Tenneti *et al.* [103], (- - -) Gobin *et al.* [46], (- · - ·) Beetstra *et al.* [12] and (○) present work. The error bars represent 95% confidence intervals over 5 MIS in the estimation of the normalized drag force.

has a small effect on the distribution of the pressure over the particles, and here again for both plans, as illustrated in figure 3.21. This result has previously been obtained in the study of Tenneti *et al.* [103]. One can observe that the same result is obtained for both plans β .

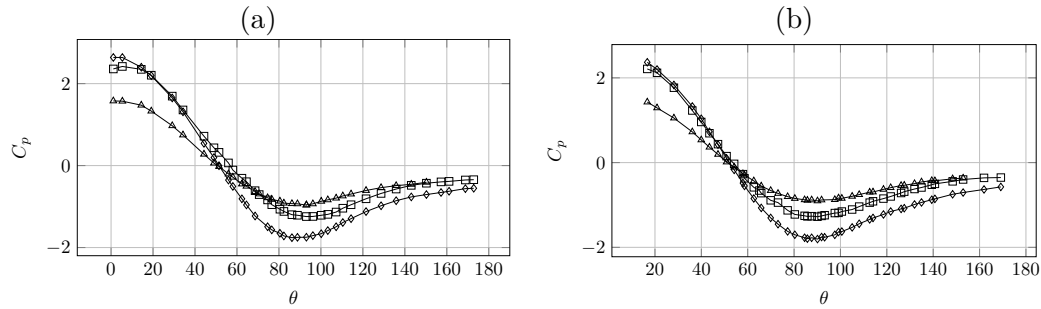


Figure 3.20: Pressure coefficient for a uniform flow past random packed spheres at $Re_S = 200$ as function of α_d (a) $\beta = 0$, (b) $\beta = 45$: (Δ) $\alpha_d = 0.1$, (\square) $\alpha_d = 0.2$ and (\diamond) $\alpha_d = 0.3$

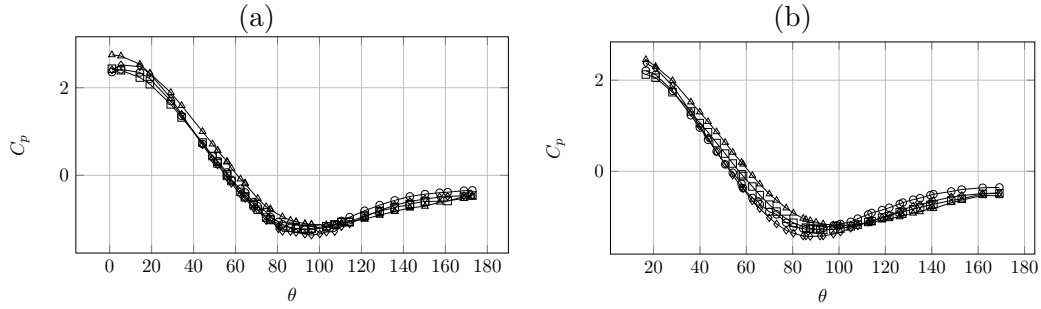


Figure 3.21: Pressure coefficient for a uniform flow past random packed spheres at $\alpha_d = 0.2$ as function of Re_S (a) $\beta = 0$, (b) $\beta = 45$: (Δ) $Re_S = 50$, (\square) $Re_S = 100$, (\diamond) $Re_S = 150$ and (\circ) $Re_S = 200$

As can suggest the correlation of Gobin *et al.* [46], our results (see figure 3.22) show that the drag force in a random arrangement of spheres is having the same dependence on the Reynolds number as for an isolated sphere. On the contrary, different behaviours are noticed for Tenneti and Beetstra simulations.

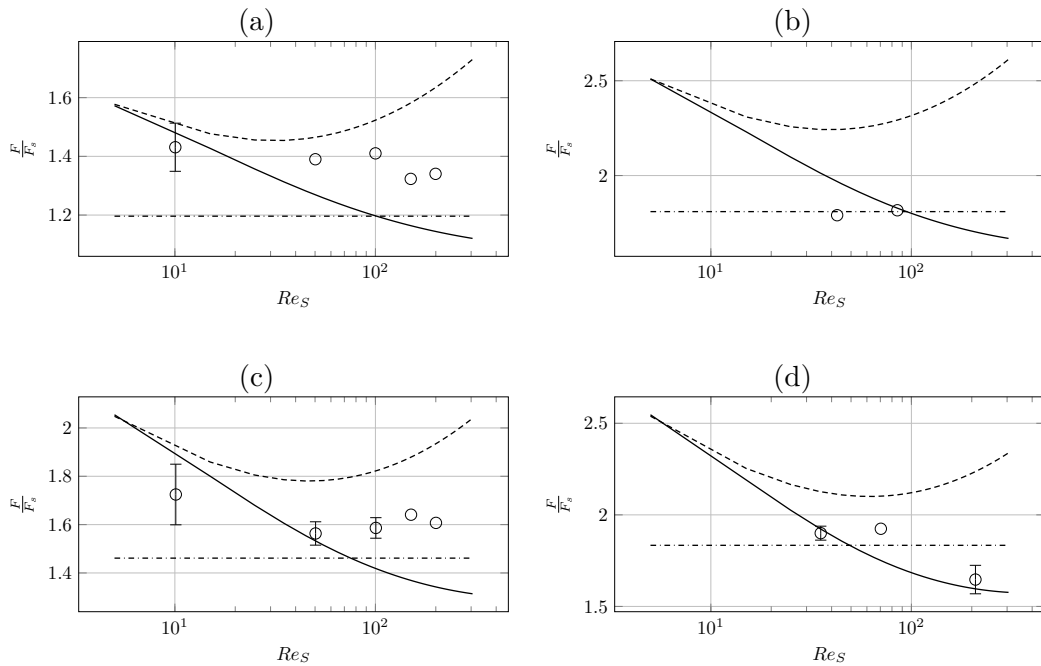


Figure 3.22: Drag force for a uniform flow past random packed spheres, normalized by Schiller & Naumann [97] drag force for a uniform flow past an isolated sphere, as function of the superficial Reynolds number Re_S and solid volume fraction (a) $\alpha_d = 0.1$, (b) $\alpha_d = 0.15$, (c) $\alpha_d = 0.2$, (d) $\alpha_d = 0.3$: (—) Tenneti *et al.* [103], (---) Gobin *et al.* [46], (-.-) Beetstra *et al.* [12] and (\circ) present work. The error bars represent 95% confidence intervals over 5 MIS in the estimation of the normalized drag force

3.5.2 Bidisperse arrangements of spheres

For a bidisperse arrangement of sphere, *i.e.* with two types of particle size, we studied a Face-Centred Cubic periodic arrangement for the two species of spheres: the larger particles are distributed in the same configuration as the one previously presented for monodisperse arrangements while the smaller particles are positioned at the center of the vertices and at the center of the cubic simulation domain. This geometry of the particle arrangement is illustrated in figure 3.23.

Two additional dimensionless parameters, for each species, are now necessary to characterize the flow:

$$x_i = \frac{\alpha_i}{\alpha_d} \quad , \quad y_i = \frac{d_i}{d_s} \quad (3.29)$$

where d_i and α_i are the particle diameter and the solid volume fraction of the specie i respectively. The Sauter mean diameter d_s is given by:

$$d_s = \left[\sum_i \frac{2 x_i}{d_i} \right]^{-1}$$

The Sauter mean diameter is one of the most important characteristic dimension for the bidisperse particle arrangement that is often used in the literature [12].

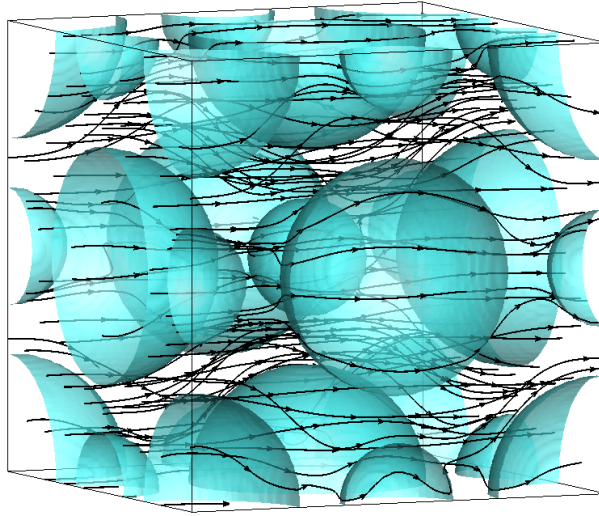


Figure 3.23: FCC/FCC bidisperse arrangement of spheres for $Re = 50$ and $\alpha_d = 0.3$ - the particle shape is plotted in blue and the black lines are the streamlines.

We have performed simulations of FCC/FCC bidispersed arrangement of spheres, for which $\frac{d_1}{d_2} = 2$, at Reynolds number $Re = 50$ and 100. The solid volume fractions for the larger particles are $\alpha_1 = 0.15$ and 0.3. The corresponding values of x_i , y_i and d_s are reported in Table 3.1.

Table 3.1: values of the parameters characterizing the bi-disperse flows simulated in this work.

x_1	x_2	y_1	y_2	d_s
0.88889	0.11111	1.11111	0.55556	0.0009m

Our force calculation results are given in figure 3.24. They are compared to Beetstra *et al.* [12] correlation that provides the drag force for the i^{th} species of particle as follows:

$$(F_B)_i = ((1 - \alpha_d)y_i + \alpha_d y_i^2 + 0.0064(1 - \alpha_d)y_i^3)F_B$$

where F_B is the Beetstra drag force for a mono-dispersed arrangement of spheres given in equation (3.28). Mehrabadi *et al.* [73] took over the Tenneti *et al.* mono-dispersed work [103] and extend it to bidispersed arrangement of spheres. A correlation was proposed from the PR-DNS data, it is given by:

$$(F_M)_i = ((1 - \alpha_d)y_i + \alpha_d y_i^2)F_T$$

where F_T is the Tenneti drag force for a mono-dispersed arrangement of spheres given in equation (3.27). The values of forces obtained with our method are compared to Beetstra [12] and Mehrabadi [73] correlations and to Massol body fitted results [70] in Figure 3.24. It can be observed that for all Reynolds numbers and solid fractions, our drag forces are in better agreement with Massol simulations than with Beetstra and Mehrabadi laws extracted from their simulations. The drag forces computed on the larger particles (y_1) seems to be lower than those in random arrangement case, when the drag forces on the smaller particles (y_2) are greater. This can be explained by the fact that in FCC/FCC arrangement of spheres, all the smaller particles are not in flow wake of the greater spheres. It can be assumed that the flow sped up by the lateral larger spheres comes to impact the small particles increasing the FCC drag force compared to the random arrangement case. In this later configuration, some of the small spheres can be behind the larger particles. The difference between FCC/FCC and random configuration forces increases with solid volume fraction (see Figure 3.24 (b) and (d)). This discrepancy is less important for the larger spheres of the bidisperse arrangement (see Figure 3.24).

3.6 Conclusions and perspectives

A new method has been designed for estimating forces in finite-size particle simulations. It is based on Lagrange extrapolation and Taylor interpolation of third order. In our method, a Lagrangian mesh is used to describe the particle shape over time on the Eulerian Cartesian mesh devoted to the flow motion. One of the most original part of our approach is to upwind the interpolation support in the normal direction to the fluid/particle interface in order to use only fluid values to

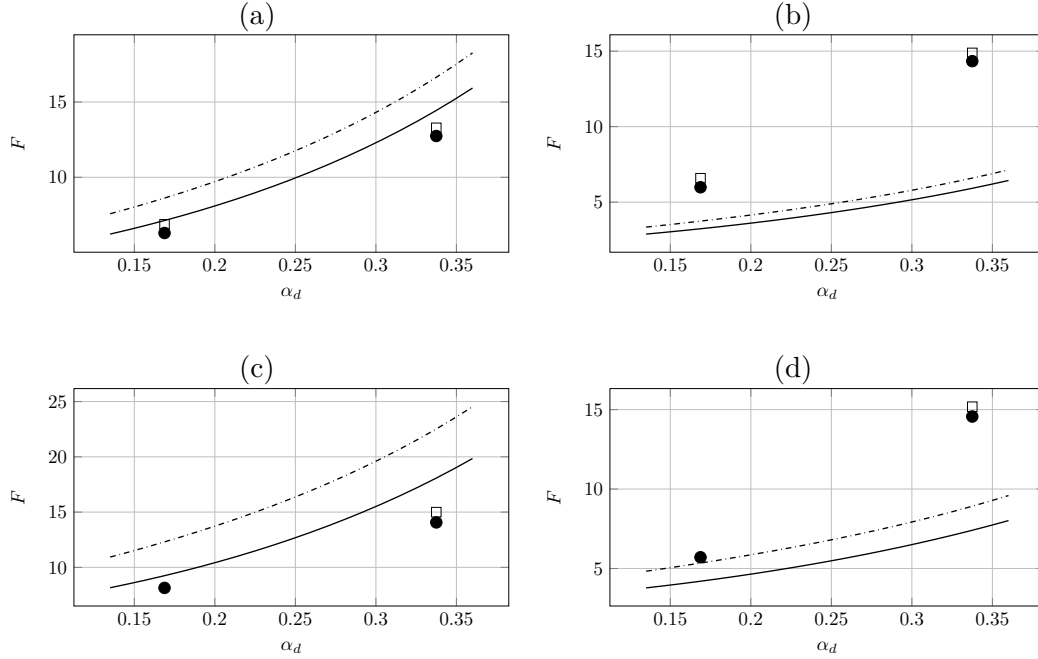


Figure 3.24: Normalized drag force for a uniform flow past a FCC/FCC packed spheres as function of the solid volume fraction α_d (a) : ($Re = 50, y_1$), (b) : ($Re = 50, y_2$), (c) : ($Re = 100, y_1$), (d) : ($Re = 100, y_2$), : (—) Beetstra & al. [12], (---) Mehrabadi *et al.* [73], (□) Massol [70], (●) present work.

estimate forces. Various parameters of the method have been tested such as effect of interpolation and extrapolation orders or the size of the particle surface elements on the error observed on forces.

Based on a second order fictitious domain method using penalty techniques and augmented Lagrangian procedures for the incompressibility constraint, we have simulated various particulate flow motions ranging from incompressible flows around an isolated particle at various Reynolds numbers to flows across packed spheres under Faced-Centered Cubic, random and bi-disperse arrangements. In all configuration, the drag forces have been compared to reference results of the literature for various solid fractions and Reynolds numbers. The general conclusion that we have obtained is that our force calculation method fits always nicely to body fitted simulations of Massol *et al.* [70] and our results are also in very good agreement with correlations of the literature such as Schiller and Naumann [97] for single particle flows and Tenneti and coworkers [73, 103] for various arrangements of particles. It has also been demonstrated that having at least 5 points in the boundary layer attached to a particle ensures to recover all the physics of the interaction between the carrier fluid and particles without using any force or interaction model. To our understanding, for obtaining a correct force calculation in finite-size particle simulations, the most important parameter is not the number of Eulerian cells along a particle diameter but the number of mesh cells belonging to the boundary layer

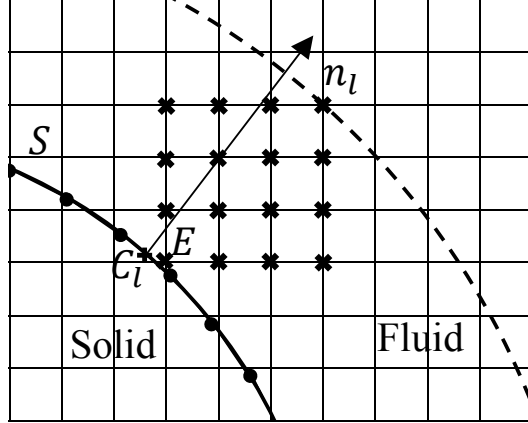


Figure 3.25: Details of Taylor interpolation points for the drag force computation at point \mathbf{C}_l of the surface Lagrangian mesh. \mathbf{E} is the nearest fluid point to the particle/fluid interface. The crosses represent the discrete compact support of the fluid points required for a 3rd order Taylor interpolation.

surrounding the particle, whatever the particle diameter.

Future works and ongoing developments are devoted to extending our method to heat flux calculation and extraction of heat transfer coefficients in particulate flows. Another interesting way of possible improvement of the accuracy of our approach is the use of Aslam extensions [8] to replace the Lagrange extrapolation in our force calculation method. Other interesting issues are the extension of the present force calculation to more complex and realistic particle shapes such as spheroid or spherocylindrical particles.

3.7 Appendix 1: Taylor Interpolation

Let us consider $f : X \in \mathbb{R}^3 \rightarrow \mathbb{R}$ a n -differentiable function at a given point \mathbf{E} . The n^{th} order Taylor Interpolation of f at point \mathbf{C}_l is:

$$f(\mathbf{C}_l) = \sum_{|\alpha|=0}^{n-1} \frac{1}{\alpha!} \frac{\partial^\alpha f}{\partial x^\alpha}(\mathbf{E})(\mathbf{C}_l - \mathbf{E})^\alpha + O(\|\mathbf{C}_l - \mathbf{E}\|^n)$$

where $\alpha = (\alpha_1, \alpha_2, \alpha_3) \in \mathbb{N}^3$ is the sum multi-index. As described in figure 3.25, \mathbf{E} denotes the nearest point to the Lagrangian particle surface point \mathbf{C}_l . Point \mathbf{E} belongs to the fluid domain and so is located on the fixed Eulerian mesh.

The four first order or Taylor interpolation are the following:

- First order:

$$f(\mathbf{C}_l) = f(\mathbf{E}) + O(\|\mathbf{C}_l - \mathbf{E}\|) \tag{3.30}$$

- Second order:

$$f(\mathbf{C}_l) = f(\mathbf{E}) + \frac{\partial f}{\partial x_i}(\mathbf{E})((\mathbf{C}_l)_i - \mathbf{E}_i) + O(\|\mathbf{C}_l - \mathbf{E}\|^2) \quad (3.31)$$

- Third order:

$$\begin{aligned} f(\mathbf{C}_l) = & f(\mathbf{E}) + \frac{\partial f}{\partial x_i}(\mathbf{E})((\mathbf{C}_l)_i - \mathbf{E}_i) + \frac{1}{2} \frac{\partial^2 f}{\partial x_i^2}(\mathbf{E})((\mathbf{C}_l)_i - \mathbf{E}_i)^2 \\ & + \frac{\partial^2 f}{\partial x_i \partial x_j}(\mathbf{E})((\mathbf{C}_l)_i - \mathbf{E}_i)((\mathbf{C}_l)_j - \mathbf{E}_j) + O(\|\mathbf{C}_l - \mathbf{E}\|^3) \end{aligned} \quad (3.32)$$

- Fourth order:

$$\begin{aligned} f(\mathbf{C}_l) = & f(\mathbf{E}) + \frac{\partial f}{\partial x_i}(\mathbf{E})((\mathbf{C}_l)_i - \mathbf{E}_i) + \frac{1}{2} \frac{\partial^2 f}{\partial x_i^2}(\mathbf{E})((\mathbf{C}_l)_i - \mathbf{E}_i)^2 \\ & + \frac{\partial^2 f}{\partial x_i \partial x_j}(\mathbf{E})((\mathbf{C}_l)_i - \mathbf{E}_i)((\mathbf{C}_l)_j - \mathbf{E}_j) + \frac{1}{6} \frac{\partial^3 f}{\partial x_i^3}(\mathbf{E})((\mathbf{C}_l)_i - \mathbf{E}_i)^3 \\ & + \sum_{i \neq j} \frac{1}{2} \frac{\partial^3 f}{\partial x_i^2 \partial x_j}(\mathbf{E})((\mathbf{C}_l)_i - \mathbf{E}_i)^2 ((\mathbf{C}_l)_j - \mathbf{E}_j) \\ & + \frac{\partial^3 f}{\partial x_1 \partial x_2 \partial x_3}(\mathbf{E})((\mathbf{C}_l)_1 - \mathbf{E}_1)((\mathbf{C}_l)_2 - \mathbf{E}_2)((\mathbf{C}_l)_3 - \mathbf{E}_3) \\ & + O(\|\mathbf{C}_l - \mathbf{E}\|^4) \end{aligned} \quad (3.33)$$

For each order of interpolation, we have to discretize the partial derivative used in it by considering the same order of discretization. To avoid using solid point in the approximation of these derivatives, we choose to use, depending on the sign of the outgoing normal vector \mathbf{n}_l , a forward (resp. a backward) difference scheme if $(\mathbf{n}_l)_i > 0$ (resp. $(\mathbf{n}_l)_i < 0$). The forward difference scheme for the derivatives used in (3.30), (3.31), (3.32), (3.33) is detailed below. The backward difference scheme is straightforwardly obtained.

Gradient approximation

$$\frac{\partial f}{\partial x_i} = \frac{3f_i - 4f_{i+1} + f_{i+2}}{-2\Delta x_i} + O(\|\Delta x\|^2)$$

$$\frac{\partial f}{\partial x_i} = \frac{11f_i - 18f_{i+1} + 9f_{i+2} - 2f_{i+3}}{-6\Delta x_i} + O(\|\Delta x\|^3)$$

$$\frac{\partial f}{\partial x_i} = \frac{25f_i - 48f_{i+1} + 36f_{i+2} - 16f_{i+3} + 3f_{i+4}}{-12\Delta x_i} + O(\|\Delta x\|^4)$$

Hessian approximation

$$\frac{\partial^2 f}{\partial x_i^2} = \frac{35f_i - 104f_{i+1} + 114f_{i+2} - 56f_{i+3} + 11f_{i+4}}{12\Delta x_i^2} + O(\|\Delta x\|^3)$$

$$\begin{aligned} \frac{\partial^2 f}{\partial x_i \partial x_j} &= \frac{539f_{i,j} - 781f_{i+1,j} + 297f_{i+2,j} - 55f_{i+3,j} - 781f_{i,j+1} + 1035f_{i+1,j+1}}{192\Delta x_i \Delta x_j} \\ &\quad - \frac{303f_{i+2,j+1} + 49f_{i+3,j+1} + 297f_{i,j+2} - 303f_{i+1,j+2} + 3f_{i+2,j+2}}{192\Delta x_i \Delta x_j} \\ &\quad + \frac{3f_{i+3,j+2} - 55f_{i,j+3} + 49f_{i+1,j+3} + 3f_{i+2,j+3} + 3f_{i+3,j+3}}{192\Delta x_i \Delta x_j} \\ &\quad + O(\|\Delta x\|^3) \end{aligned}$$

$$\frac{\partial^2 f}{\partial x_i^2} = \frac{45f_i - 154f_{i+1} + 214f_{i+2} - 156f_{i+3} + 61f_{i+4} - 10f_{i+5}}{12\Delta x_i^2} + O(\|\Delta x\|^4)$$

$$\begin{aligned} \frac{\partial^2 f}{\partial x_i \partial x_j} &= \frac{117f_{i,j} - 73f_{i+1,j} - 83f_{i+2,j} + 42f_{i+3,j} - 3f_{i+4,j} - 73f_{i,j+1} - 243f_{i+1,j+1}}{60\Delta x_i \Delta x_j} \\ &\quad - \frac{477f_{i+2,j+1} - 173f_{i+3,j+1} + 12f_{i+4,j+1} - 83f_{i,j+2} + 477f_{i+1,j+2}}{60\Delta x_i \Delta x_j} \\ &\quad + \frac{-528f_{i+2,j+2} + 137f_{i+3,j+2} - 3f_{i+4,j+2} + 42f_{i,j+3} - 173f_{i+1,j+3}}{60\Delta x_i \Delta x_j} \\ &\quad + \frac{137f_{i+2,j+3} - 3f_{i+3,j+3} - 3f_{i+4,j+3} - 3f_{i,j+4} + 12f_{i+1,j+4} - 3f_{i+2,j+4}}{60\Delta x_i \Delta x_j} \\ &\quad + \frac{-3f_{i+3,j+4} - 3f_{i+4,j+4}}{60\Delta x_i \Delta x_j} + O(\|\Delta x\|^4) \end{aligned}$$

Third order derivative approximation

$$\begin{aligned} \frac{\partial^3 f}{\partial x_i^3} &= \frac{49f_i - 232f_{i+1} + 461f_{i+2} - 496f_{i+3} + 307f_{i+4} - 104f_{i+5} + 15f_{i+6}}{-8\Delta x_i^3} \\ &\quad + O(\|\Delta x\|^4) \end{aligned}$$

$$\begin{aligned}
\frac{\partial^3 f}{\partial x_i^2 \partial x_j} = & \frac{2775f_{i,j} - 8725f_{i+1,j} + 10895f_{i+2,j} - 7105f_{i+3,j} + 2550f_{i+4,j}}{-480\Delta x_i^2 \Delta x_j} \\
& - \frac{390f_{i+5,j} - 4085f_{i,j+1} + 11931f_{i+1,j+1} - 13489f_{i+2,j+1}}{-480\Delta x_i^2 \Delta x_j} \\
& + \frac{7911f_{i+3,j+1} - 2654f_{i+4,j+1} + 386f_{i+5,j+1} + 1675f_{i,j+2}}{-480\Delta x_i^2 \Delta x_j} \\
& + \frac{-3889f_{i+1,j+2} + 2856f_{i+2,j+2} - 744f_{i+3,j+2} + 101f_{i+4,j+2}}{-480\Delta x_i^2 \Delta x_j} \\
& + \frac{f_{i+5,j+2} - 385f_{i,j+3} + 711f_{i+1,j+3} - 264f_{i+2,j+3} - 64f_{i+3,j+3}}{-480\Delta x_i^2 \Delta x_j} \\
& + \frac{f_{i+4,j+3} + f_{i+5,j+3} + 10f_{i,j+4} - 14f_{i+1,j+4} + f_{i+2,j+4} + f_{i+3,j+4}}{-480\Delta x_i^2 \Delta x_j} \\
& + \frac{f_{i+4,j+4} + f_{i+5,j+4} + 10f_{i,j+5} - 14f_{i+1,j+5} + f_{i+2,j+5} + f_{i+3,j+5}}{-480\Delta x_i^2 \Delta x_j} \\
& + \frac{f_{i+4,j+5} + f_{i+5,j+5}}{-480\Delta x_i^2 \Delta x_j} + O(\|\Delta x\|^4)
\end{aligned}$$

$$\begin{aligned}
\frac{\partial^3 f}{\partial x_1 \partial x_2 \partial x_3} = & \frac{4069f_{i,j,k} - 13656f_{i+1,j,k} - 6f_{i+2,j,k} - 6f_{i+3,j,k} - 6f_{i+4,j,k}}{-9000\Delta x_1 \Delta x_2 \Delta x_3} \\
& + \frac{12194f_{i,j+1,k} - 23256f_{i+1,j+1,k} + 10194f_{i+2,j+1,k} + 444f_{i+3,j+1,k}}{-9000\Delta x_1 \Delta x_2 \Delta x_3} \\
& + \frac{-306f_{i+4,j+1,k} - 16681f_{i,j+2,k} + 77094f_{i+1,j+2,k} - 19206f_{i+2,j+2,k}}{-9000\Delta x_1 \Delta x_2 \Delta x_3} \\
& + \frac{-456f_{i+3,j+2,k} + 294f_{i+4,j+2,k} - 6f_{i,j+3,k} - 52956f_{i+1,j+3,k}}{-9000\Delta x_1 \Delta x_2 \Delta x_3} \\
& + \frac{11244f_{i+2,j+3,k} + 244f_{i+3,j+3,k} - 6f_{i+4,j+3,k} - 6f_{i,j+4,k}}{-9000\Delta x_1 \Delta x_2 \Delta x_3} \\
& + \frac{13794f_{i+1,j+4,k} - 3006f_{i+2,j+4,k} - 6f_{i+3,j+4,k} - 6f_{i+4,j+4,k}}{-9000\Delta x_1 \Delta x_2 \Delta x_3} \\
& + \frac{-6f_{i,j,k+1} + 18294f_{i+1,j,k+1} + 744f_{i+2,j,k+1} - 6f_{i+3,j,k+1}}{-9000\Delta x_1 \Delta x_2 \Delta x_3} \\
& + \frac{-6f_{i+4,j,k+1} + 59869f_{i,j+1,k+1} - 6f_{i+1,j+1,k+1} - 6f_{i+2,j+1,k+1}}{-9000\Delta x_1 \Delta x_2 \Delta x_3} \\
& + \frac{-6f_{i+3,j+1,k+1} - 6f_{i+4,j+1,k+1} - 177281f_{i,j+2,k+1} - 40506f_{i+1,j+2,k+1}}{-9000\Delta x_1 \Delta x_2 \Delta x_3} \\
& + \frac{-756f_{i+2,j+2,k+1} - 6f_{i+3,j+2,k+1} - 6f_{i+4,j+2,k+1} + 153019f_{i,j+3,k+1}}{-9000\Delta x_1 \Delta x_2 \Delta x_3} \\
& + \frac{26994f_{i+1,j+3,k+1} + 1494f_{i+2,j+3,k+1} - 6f_{i+3,j+3,k+1} - 6f_{i+4,j+3,k+1}}{-9000\Delta x_1 \Delta x_2 \Delta x_3} \\
& + \frac{-34281f_{i,j+4,k+1} - 7506f_{i+1,j+4,k+1} - 6f_{i+2,j+4,k+1} - 6f_{i+3,j+4,k+1}}{-9000\Delta x_1 \Delta x_2 \Delta x_3} \\
& + \frac{-6f_{i+4,j+4,k+1} - 7581f_{i,j,k+2} + 3444f_{i+1,j,k+2} - 4356f_{i+2,j,k+2}}{-9000\Delta x_1 \Delta x_2 \Delta x_3} \\
& + \frac{-606f_{i+3,j,k+2} + 144f_{i+4,j,k+2} - 136281f_{i,j+1,k+2}}{-9000\Delta x_1 \Delta x_2 \Delta x_3} \\
& + \frac{-4506f_{i+1,j+1,k+2} + 3744f_{i+2,j+1,k+2} - 6f_{i+3,j+1,k+2} - 6f_{i+4,j+1,k+2}}{-9000\Delta x_1 \Delta x_2 \Delta x_3} \\
& + \frac{348519f_{i,j+2,k+2} + 3744f_{i+1,j+2,k+2} - 6f_{i+2,j+2,k+2} - 6f_{i+3,j+2,k+2}}{-9000\Delta x_1 \Delta x_2 \Delta x_3} \\
& + \frac{-6f_{i+4,j+2,k+2} - 257481f_{i,j+3,k+2} - 6f_{i+1,j+3,k+2} - 6f_{i+2,j+3,k+2}}{-9000\Delta x_1 \Delta x_2 \Delta x_3} \\
& + \frac{-6f_{i+3,j+3,k+2} - 6f_{i+4,j+3,k+2} + 51294f_{i,j+4,k+2} - 6f_{i+1,j+4,k+2}}{-9000\Delta x_1 \Delta x_2 \Delta x_3} \\
& + \frac{-6f_{i+2,j+4,k+2} - 6f_{i+3,j+4,k+2} - 6f_{i+4,j+4,k+2} - 6f_{i,j,k+3}}{-9000\Delta x_1 \Delta x_2 \Delta x_3} \\
& + \frac{-1206f_{i+1,j,k+3} - 6f_{i+2,j,k+3} + 494f_{i+3,j,k+3} - 6f_{i+4,j,k+3}}{-9000\Delta x_1 \Delta x_2 \Delta x_3} \\
& + \frac{97519f_{i,j+1,k+3} - 6f_{i+1,j+1,k+3} - 6f_{i+2,j+1,k+3} - 6f_{i+3,j+1,k+3}}{-9000\Delta x_1 \Delta x_2 \Delta x_3} \\
& + \frac{-6f_{i+4,j+1,k+3} - 212981f_{i,j+2,k+3} - 6f_{i+1,j+2,k+3} - 6f_{i+2,j+2,k+3}}{-9000\Delta x_1 \Delta x_2 \Delta x_3} \\
& + \frac{-6f_{i+3,j+2,k+3} - 6f_{i+4,j+2,k+3} + 136469f_{i,j+3,k+3} - 6f_{i+1,j+3,k+3}}{-9000\Delta x_1 \Delta x_2 \Delta x_3} \\
& + \frac{-6f_{i+2,j+3,k+3} - 6f_{i+3,j+3,k+3} - 6f_{i+4,j+3,k+3} - 20181f_{i,j+4,k+3}}{-9000\Delta x_1 \Delta x_2 \Delta x_3}
\end{aligned}$$

$$\begin{aligned}
& + \frac{-6f_{i+1,j+4,k+3} - 6f_{i+2,j+4,k+3} - 6f_{i+3,j+4,k+3} - 6f_{i+4,j+4,k+3}}{-9000\Delta x_1\Delta x_2\Delta x_3} \\
& + \frac{-6f_{i,j,k+3} + 294f_{i+1,j,k+3} - 6f_{i+2,j,k+3} - 6f_{i+3,j,k+3} - 6f_{i+4,j,k+3}}{-9000\Delta x_1\Delta x_2\Delta x_3} \\
& + \frac{-19531f_{i,j+1,k+3} - 6f_{i+1,j+1,k+3} - 6f_{i+2,j+1,k+3} - 6f_{i+3,j+1,k+3}}{-9000\Delta x_1\Delta x_2\Delta x_3} \\
& + \frac{-6f_{i+4,j+1,k+3} + 38294f_{i,j+2,k+3} - 6f_{i+1,j+2,k+3} - 6f_{i+2,j+2,k+3}}{-9000\Delta x_1\Delta x_2\Delta x_3} \\
& + \frac{-6f_{i+3,j+2,k+3} - 6f_{i+4,j+2,k+3} - 18931f_{i,j+3,k+3} - 6f_{i+1,j+3,k+3}}{-9000\Delta x_1\Delta x_2\Delta x_3} \\
& + \frac{-6f_{i+2,j+3,k+3} - 6f_{i+3,j+3,k+3} - 6f_{i+4,j+3,k+3} - 6f_{i,j+4,k+3}}{-9000\Delta x_1\Delta x_2\Delta x_3} \\
& + \frac{-6f_{i+1,j+4,k+3} - 6f_{i+2,j+4,k+3} - 6f_{i+3,j+4,k+3} - 6f_{i+4,j+4,k+3}}{-9000\Delta x_1\Delta x_2\Delta x_3} \\
& + O(\|\Delta x\|^4)
\end{aligned}$$

Chapter 4

Accurate calculation of heat transfer coefficients for motions around particles with a finite-size particle approach

This chapter is the article [23] authored by M.-A. Chadil, S. Vincent and J.-L. Estivalezes

Abstract

The calculation of heat transfers between an incompressible fluid and a set of resolved-scale particles is a complex task as soon as the simulation mesh is not adapted to the shape of the particles. In the present work, an Implicit tensorial Viscous penalty method is used to resolve the particulate flow. A new Lagrange extrapolation coupled to a Taylor interpolation of high order [24] is extended to the accurate estimate of heat transfer coefficients on an isolated sphere, a fixed Faced-Centered Cubic array of spheres and a random pack of spheres. The simulated heat transfer coefficients are compared with success to various existing Nusselt laws of the literature.

4.1 Introduction

Gas-solid flows are widely encountered in nature, for example in volcanic eruptions [10, 33]. They also participate to heat transfers in many industrial processes such as petroleum refining, blast furnaces or chemical looping combustion [2, 67, 71]. Due to the scale disparity between these applications and the particle size at the industrial scale, the CFD simulations of such applications are based on statistical approaches where the average interphase transfer of energy between the fluid and the particles need to be modeled.

Theoretical and Experimental approaches have been widely investigated to model these unclosed terms with significant limitations. Indeed, theoretical results are limited to creeping Stokes flows or moderate Reynolds number regimes [1, 81]. In addition, experimental measurements showed huge differences of Nusselt number at high volume fraction because of limited optical access [112]. This motivates the community to consider and develop Particle-Resolved Direct Numerical Simulations (PR-DNS) to directly compute the fluid-particle interaction and the associated heat transfer closure laws.

In the last decade, many researchers have conducted numerical studies to characterize, understand and then model the energy interphase exchange in gas-solid flows for numerous configurations of particulate motions. Among them, we can cite Massol [70] who studied heat transfers in a fixed array of monodisperse spheres using a body fitted three-dimensional PR-DNS (AVBP code [98]). This configuration will be studied in this work and our results will be compared to those of Massol [70]. Deen *et al.* [36] and Tavassoli *et al.* [102] used Immersed Boundary Methods (IBM) for three-dimensional PR-DNS with inflow and outflow boundary conditions to compute the gas-solid Nusselt number that is compared with Gunn's correlation [47]. Note that Gunn [47] proposed his correlation based on experimental results. Tenneti *et al.* [104] utilized the so called PUREIBM with a periodic boundary conditions and proposed a correlation from their results for various flow configurations. Later, Deen *et al.* [37] proposed a correlation based on Tavassoli *et al.* [102] and Tenneti *et al.* [104] results. Tenneti *et al.* [104] simulations were carried out for a limited range of Reynolds number and solid volume fraction. As a consequence, Sun [99] took over this work and extended it to larger values of Reynolds numbers and solid volume fractions and proposed a correlation that fits their PR-DNS data.

Our contribution is to propose an accurate heat flux estimate for finite-size particle simulations using Implicit Tensorial Penalty Method (ITPM) [109]. This work is an extension of the developments conducted to compute the drag force [24] in previous studies. The proposed method uses a fixed Eulerian structured mesh for the flow solving. It manages to avoid the contaminated flow in the Eulerian cells cut by the interface, and therefore extract the accurate heat flux needed to compute the Nusselt number.

The article is structured as follows. A presentation of the models and numerical methods is first proposed in section 4.2. In the third section 4.3, validations for flows interacting with isolated spherical particles at various Reynolds number are discussed. Simulations of a uniform flow past a Face-Centered cubic array of spheres are presented in the fourth section 4.4. Section 4.5 is devoted to simulations and validations of flows through random arrangements of monodispersed spheres. Finally, conclusions and perspectives are drawn in 4.6.

4.2 Numerical Methodology

Conservation equations

The motion equations of incompressible two-phase flows, involving a carrier fluid and a solid particle phase, are based on one-fluid model as explained in [26, 109]. They are given by:

$$\nabla \cdot \mathbf{u} = 0 \quad (4.1)$$

$$\rho \left(\frac{\partial \mathbf{u}}{\partial t} + (\mathbf{u} \cdot \nabla) \mathbf{u} \right) = -\nabla p + \rho \mathbf{g} + \nabla \cdot [\mu(\nabla \mathbf{u} + \nabla^t \mathbf{u})] \quad (4.2)$$

$$\rho C_p \left(\frac{\partial T}{\partial t} + \mathbf{u} \cdot \nabla T \right) = \nabla \cdot (k_f \nabla T) \quad (4.3)$$

where \mathbf{u} is the velocity, p the pressure, T the temperature, t the time, \mathbf{g} the gravity vector, ρ , μ , C_p and k_f respectively the density, the viscosity, the specific heat and the thermal conductivity of the equivalent fluid. By equivalent fluid we mean the fluid that is considered in both fluid and solid phases in our fixed mesh approach, *i.e.* densities, viscosities, specific heat and conductivities are continuous across interface in the cells cut by the particle surface. Specific arithmetic or harmonic laws are used to defined them according to a phase function C . This phase function is directly obtained by projecting the shape of the particles on the Eulerian mesh [24] [109]. The discretization, solving and validation of equations (4.1-4.3) is developed in [109] and [63].

The particles in this work are motionless. Numerically, their velocity is set to zero by imposing the velocity of the Eulerian cells near their centroids to zero, and the viscous penalty method propagates the zero velocity in the whole solid medium. The particle temperatures being also constant, they are imposed in the whole solid medium.

Heat transfer rate computation for immersed boundary methods

The goal of this work is to extract from the temperature field, that is solution of the energy equation 4.3, the Nusselt number given by:

$$Nu = \frac{H_p d}{k_f} \quad (4.4)$$

where d is the particle diameter and H_p is the heat transfer rate given by:

$$H_p = \frac{Q_p}{(T_s - T_f) \pi d^2} \quad (4.5)$$

where T_s and T_f are the temperatures of the particle and the fluid respectively, and Q_p is the heat flux across the particle surface S . It is given by:

$$Q_p = \oint_S -k_f \nabla T \cdot \mathbf{n} \, dS \quad (4.6)$$

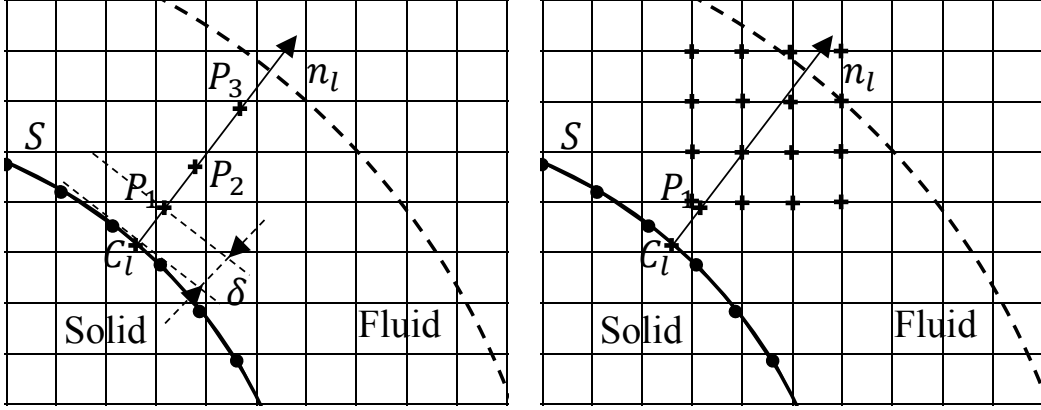


Figure 4.1: Notations for the third order Lagrange extrapolation (left) and the third order Taylor interpolation (right), used in heat flux computations.

The computation of the heat flux consists in discretizing S on a set of N elements called Lagrangian mesh (see Figure 4.1), such that:

$$Q_p \approx \sum_l^N -k_f (\nabla T)_l \cdot \mathbf{n}_l \Delta S_l \quad (4.7)$$

where the ongoing normal to the l^{th} element \mathbf{n}_l and its area ΔS_l are deduced from its nodes coordinates. However, the temperature T being solved on the Eulerian mesh, the temperature gradient $(\nabla T)_l$ is not known at the l^{th} element center C_l . To deal with this problem, we have implemented the same approach that we used to obtain the stress tensor $\bar{\sigma}_l$ components on the Lagrangian mesh in the drag force

computation $\mathbf{F} \approx \sum_l^N \bar{\sigma}_l \cdot \mathbf{n}_l \Delta S_l$. This was detailed in [24]. In this previous work, we

have observed that the velocity and the pressure values were inaccurate in the cells containing the interface. Therefore, we had to extrapolate the stress tensor from the area far from the particle to the particle surface. After a numerical study of all the extrapolation parameters, we have reached the conclusion that the third order Lagrange extrapolation (whose notations are illustrated in Figure 4.1) is the best compromise between accuracy and computational cost [24]. Similarly as for force coefficients, we have the temperature gradient at the center of each Lagrangian mesh element as follows:

$$(\nabla T)(\mathbf{C}_l) = \sum_{i=1}^3 (\nabla T)(\mathbf{P}_i) L_i(\mathbf{C}_l) \quad , \quad \text{where} \quad L_i(\mathbf{C}_l) = \prod_{j \neq i}^3 \frac{|\mathbf{C}_l - \mathbf{P}_j|}{|\mathbf{P}_i - \mathbf{P}_j|} \quad (4.8)$$

Given that the temperature gradient is computed on the Eulerian mesh and that the extrapolation points \mathbf{P}_1 , \mathbf{P}_2 and \mathbf{P}_3 are constructed in the normal direction to the particle surface (see Figure 4.1), the temperature gradient at these points are not known. Once again, we relayed on the work [24] to interpolate the temperature gradient from the Eulerian mesh to the extrapolation point \mathbf{P}_k ($k = 1, 2, 3$) using the third order Taylor interpolation:

$$f(\mathbf{P}_k) = f(\mathbf{E}) + \frac{\partial f}{\partial x_i}(\mathbf{E})((\mathbf{C}_l)_i - \mathbf{E}_i) + \frac{1}{2} \frac{\partial^2 f}{\partial x_i^2}(\mathbf{E})((\mathbf{C}_l)_i - \mathbf{E}_i)^2 + \frac{\partial^2 f}{\partial x_i \partial x_j}(\mathbf{E})((\mathbf{C}_l)_i - \mathbf{E}_i)((\mathbf{C}_l)_j - \mathbf{E}_j) + O(\|\mathbf{C}_l - \mathbf{E}\|^3) \quad (4.9)$$

where \mathbf{E} is the nearest Eulerian point to \mathbf{P}_k .

Another pertinent value to consider when studying the distribution of heat transfers on the surface of the particle, is the local Nusselt number given in the spherical system (see Figure 4.2) by:

$$Nu_{loc}(\theta) = \frac{-\nabla T \cdot \mathbf{n} d}{(T_s - T_f)} \quad (4.10)$$

where for each Lagrangian mesh element center ($\mathbf{C}_l = (x, y, z)$), the azimuthal angle θ , and the polar angle β are given by:

$$\theta = (\pi - \arctan 2(\sqrt{y^2 + z^2}, x)) \frac{180}{\pi}, \quad \beta = \arctan 2(z, y) \frac{180}{\pi} \quad (4.11)$$

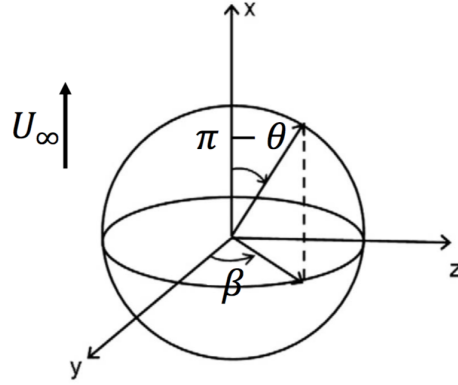


Figure 4.2: Spherical coordinate system around a particle. The flow direction is represented by the undisturbed velocity U_∞ .

4.3 Convective heat transfer forced by a uniform flow around a stationary sphere

The first case considered to validate heat transfers solved with the viscous penalty method, is the convection forced by uniform flow past a hot sphere, illustrated in Figure 4.3. This case was previously used to validate the drag force computation, and all its parameters are detailed in [24]. In the simulations carried out for this

case as well as for all the cases studied in this work, we have imposed that the hydrodynamic boundary layer contains 5 Eulerian cells. This mesh refinement ensures that the hydrodynamic boundary layer contains a sufficient number of extrapolation points to be accurate on force calculations at the particle surface. We have also chosen a Prandtl number $Pr = 0.72$, which means that the thermal boundary layer is larger than the hydrodynamic boundary layer. In this way, we ensure that enough extrapolation points are available in the thermal boundary layer as well (see Figure 4.1).

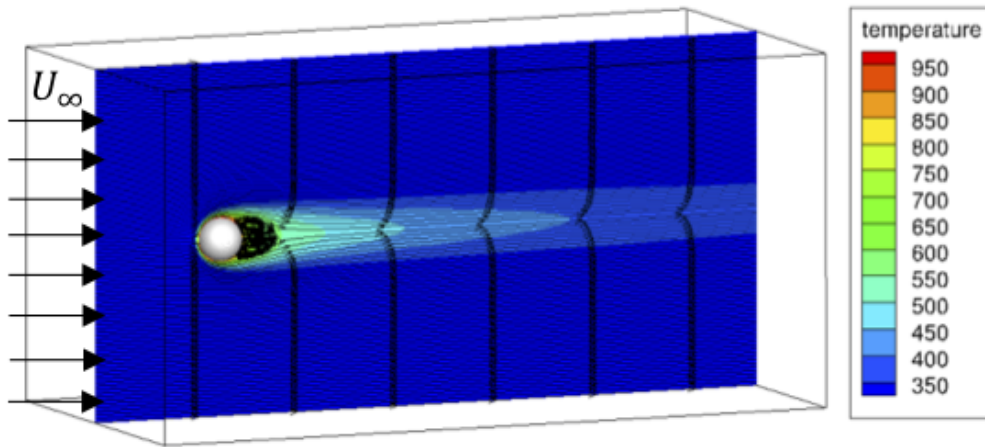


Figure 4.3: Streamlines and temperature field for a uniform flow past a sphere at $Re = 100$.

Effect of the extrapolation distance (δ)

One of the extrapolation parameter studied in the drag force computation work [24] was the distance δ between the Lagrangian mesh and the first extrapolation point \mathbf{P}_1 (see Figure 4.1). Indeed, during that study [24], inaccurate pressure and velocity values were observed in the cells cut by the interface, therefore we had to extrapolate the stress tensor from the fluid area far from the particle to the surface. And as illustrated in (Figure 4.4 left), the accurate drag force is reached at $\delta = \Delta x$.

The temperature being function of the velocity (Eq.4.3), inaccurate temperature gradient values are also expected in the Eulerien cells containing the interface. Thus, we have conducted the same study for the Nusselt number computation to locate the extrapolation area. But unlike the drag force (Figure 4.4 left), the Nusselt number computation does not seem to depend on the distance δ (Figure 4.4 right). Facing this unexpected results, we have compared the distribution of the local Nusselt number to Massol [70] results at $Re = 100$ where the flow is symmetric with respect to its direction, as illustrated in Figure 4.5. The local Nusselt number

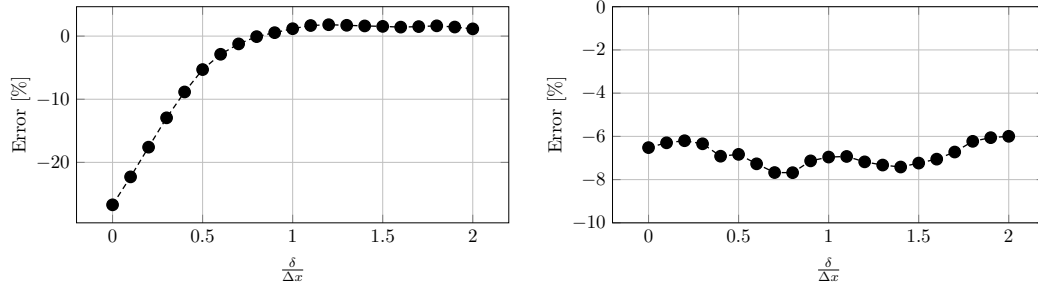


Figure 4.4: Drag force relative error to Schiller & Naumann [97] correlation (left) and Nusselt number relative error to Ranz&Marshall [88] correlation (right), as function of the distance δ at $Re = 100$.

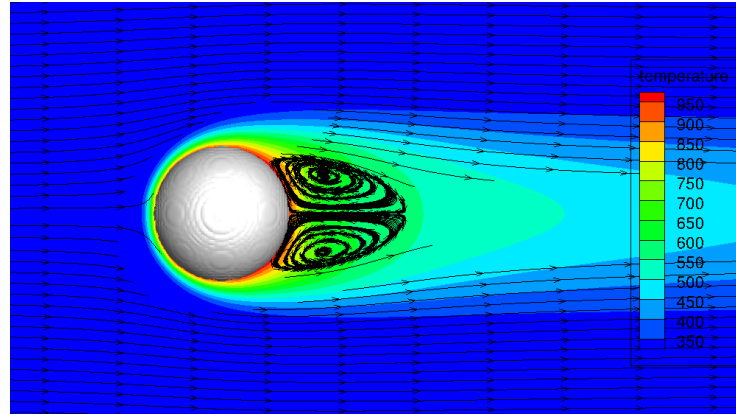


Figure 4.5: Streamlines and temperature field for a uniform flow past a sphere at $Re = 100$.

computed for $\delta = 0$ does not reflect the flow symmetry as illustrated in (Figure 4.6 a), and the error between our result (Nu_{loc}) and Massol's ($Nu_{locMassol}$) given by $\frac{\sum_{i=1}^N |(Nu_{loc})_i - (Nu_{locMassol})_i|}{\sum_{i=1}^N |(Nu_{locMassol})_i|}$ is about 25%. This error decreases as the distance δ increases until being lower than 10% for $\delta \geq 1$ (Figure 4.6 c). It is worth noting that for this distance, the local Nusselt number distribution translates in better way the symmetrical behavior of the flow as it satisfies almost the same distribution for all the polar angle (β) plans (Figure 4.6 b). So, as for the drag force computation [24] and in the rest of this work, the extrapolation distance will always be $\delta = 1$.

Result on the Nusselt coefficient

The numerical parameters of the heat transfer on the particle surface being set up, the global Nusselt number for a uniform flow past a hot sphere at different Reynolds number ($Re = 10, 20, 40, 60, 80, 100, 150, 200, 250, 290$) is computed using the presented method and compared to existing literature results:

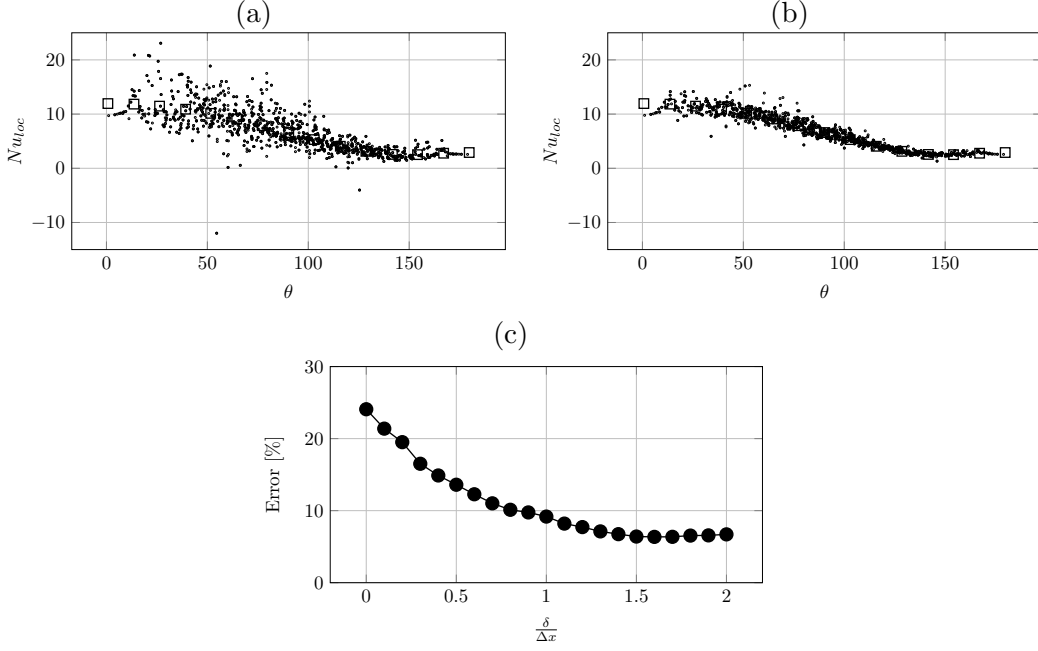


Figure 4.6: Local Nusselt coefficient for a uniform flow past an isolated sphere at $Re = 100$, as function of the azimuthal angle θ , for all points on the particle surface (for all β plans) at (a) $\delta = 0$ and (b) $\delta = 1$: (.) present work, (\square) Massol [70]. (c) is local Nusselt number relative error to Massol’s result [70] as function of the extrapolation distance δ .

- Ranz & Marshall [88]:

$$Nu = 2. + 0.6 Re^{0.5} Pr^{\frac{1}{3}} \quad (4.12)$$

- Feng & Michaelides [43]:

$$Nu = 0.992 + (RePr)^{\frac{1}{3}} + 0.1 Re^{\frac{2}{3}} Pr^{\frac{1}{3}} \quad (4.13)$$

- Whitaker [115]:

$$Nu = 2. + \left(0.4 Re^{0.5} + 0.06 Re^{\frac{2}{3}}\right) Pr^{0.4} \quad (4.14)$$

Figure 4.7 provides the comparisons of our results to literature references. It can be observed that our simulated Nusselt values belong to the same value ensemble as literature works for all considered Reynolds numbers. If we go into more details, the Nusselt numbers simulated with ITPM show a better agreement with Feng & Michaelides and Whitaker correlations than with Ranz & Marshall.

4.4 Face-Centered Cubic periodic arrangement of spheres

The second case studied in this work is a uniform flow past a Face-Centered Cubic (FCC) array of hot spheres illustrated in Figure 4.8. This case was previously used

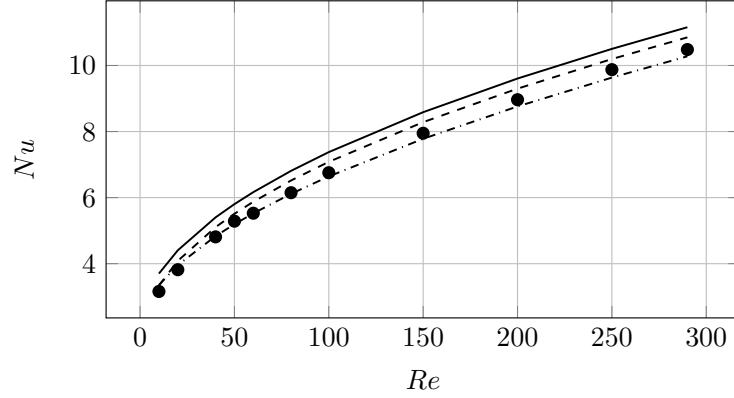


Figure 4.7: Nusselt coefficient for the uniform flow past a hot sphere at different Reynolds numbers: (—) Ranz & Marshall [88], (---) Feng & Michaelides [43], (-·-·) Whitaker [115], (●) present work.

to validate the drag force computation [24]. All its parameters were fully detailed in this reference. In that work, the drag force was computed when the study state of the flow was reached. The simulations considered here take that steady state as initial condition for the momentum equation 'Eq. 4.2'. In addition, the initial temperature conditions for the energy equation 'Eq. 4.3' are $T_s = 1, T_f = 0.5$, respectively the sphere and the fluid temperature. In this problem, the fluid heats up until it reaches the sphere temperature (see Figure 4.9 left). In the meantime and after a time initialization of the temperature gradient around the spheres, a balance is reached between the heat flux and the difference between the fluid and the particle temperature (see Figure 4.8). This results in the apparition of a plateau in the global Nusselt coefficient temporal evolution as illustrated in Figure 4.9 right. The values of the Nusselt number for uniform flow past a FCC array of spheres will be chosen at this stabilized state.

The global and local Nusselt coefficients for a uniform flow past an array of N_p particles are an average of those computed on each sphere such as:

$$\langle Nu \rangle = \frac{1}{N_p} \sum_i^{N_p} Nu_i \quad \langle Nu_{loc} \rangle = \frac{1}{N_p} \sum_i^{N_p} (Nu_{loc})_i \quad (4.15)$$

where $N_p = 4$ for a FCC array.

Using the local Nusselt coefficient distribution presented in figure 4.10, two regimes can be observed, *i.e.* attached (illustrated in Figure 4.8 left) and separated (Figure 4.8 right) flows, that govern the uniform flow past a FCC array of spheres, depending on the Reynolds number and the solid volume fraction α_d :

Attached flows

For low Reynolds numbers, the local Nusselt number is having the same behavior as an isolated sphere (see Figure 4.10 left). The increase of its value is due to the

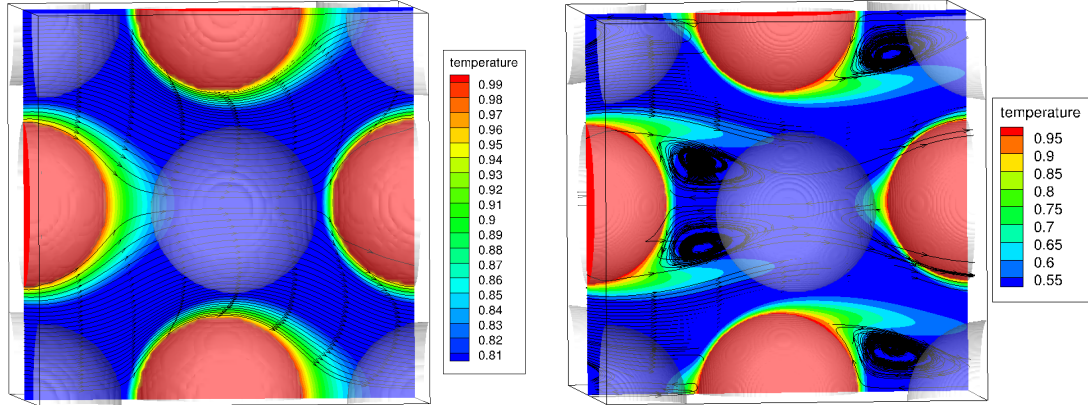


Figure 4.8: Streamlines and temperature field for a steady flow along the x-axis of a Face-Centered Cubic array of spheres at $Re = 50$, $\alpha_d = 0.15$ (left), and at $Re = 300$, $\alpha_d = 0.15$ (right)

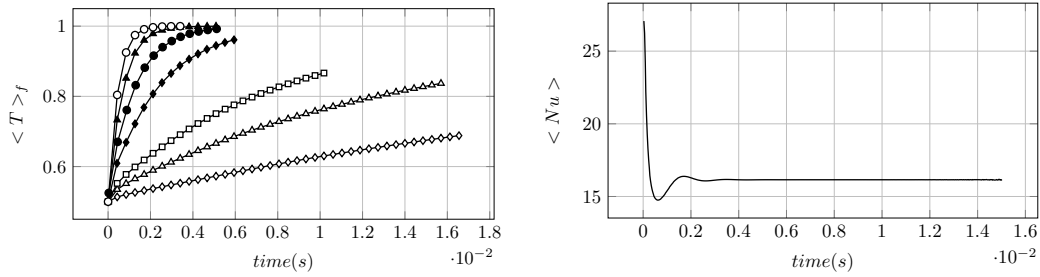


Figure 4.9: Left: Time evolution of fluid temperature for a uniform flow past a Face-Centered Cubic array of spheres at $Re = 50$ and (\diamond) $\alpha_d = 0.05$, (\triangle) $\alpha_d = 0.1$, (\square) $\alpha_d = 0.15$, (\blacklozenge) $\alpha_d = 0.3$, (\bullet) $\alpha_d = 0.4$, (\blacktriangle) $\alpha_d = 0.5$, (\circ) $\alpha_d = 0.6$. Right: Time evolution of averaged Nusselt coefficient for a uniform flow past a Face-Centered Cubic array of spheres at $Re = 50$ and $\alpha_d = 0.4$.

presence of the other spheres (blocking effect) that speed up the flow and therefore flatten the boundary layer which increases the temperature gradient. We can also observe that the presence of surrounding particles breaks the symmetry of the flow. Indeed, (Figure 4.10 left) shows two distinct distribution of the local Nusselt number for two different plans ($\beta = 0$) and ($\beta = 45$), and these results are in good agreement with Massol body fitted simulations [70].

Separated flows downstream of the spheres

By increasing the Reynolds number, a separated flow appears downstream of the spheres together with a fountain effect upstream of the spheres (see Figure 4.8 right). These phenomena can be observed also in the local Nusselt number distribution. Indeed, the higher value of the Nusselt number is no more at the upstream stagnation point $\theta = 0$, due to the fountain effect that induces a low heat flux. With increasing θ , *i.e.* leaving the fountain zone, the Nusselt number increases as the

boundary layer shrinks due to the fluid acceleration in this zone. It then decreases until the separation point, where the fluid temperature is the highest. Finally, the Nusselt increases again in the recirculating zone behind the sphere.

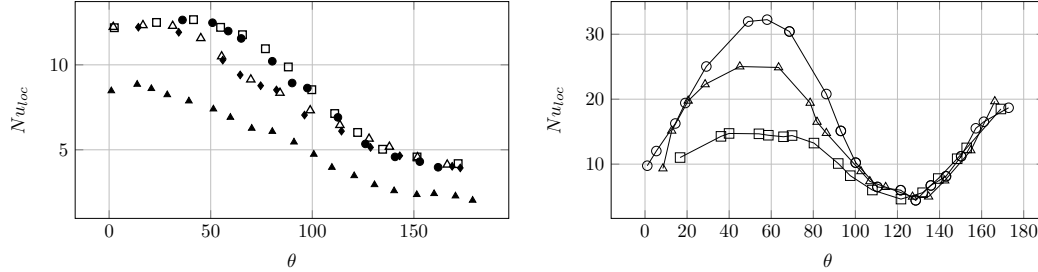


Figure 4.10: Left: Local nusselt number for a uniform flow past an isolated sphere at $Re = 50$ (\blacktriangle) and for a uniform flow past a FCC array of spheres at $Re = 50$, $\alpha_d = 0.15$: $\beta = 0$ (\triangle Massol [70], \blacklozenge present work) and $\beta = 45$ (\square Massol [70], \bullet present work). Right: Local Nusselt number for a uniform flow past a FCC array of spheres at $Re = 300$, $\alpha_d = 0.15$: $\beta = 0$ (\circ), $\beta = 22.5$ (\triangle), $\beta = 45$ (\square).

Global Nusselt coefficient

The Nusselt number of a uniform flow past a FCC array of spheres normalized by the isolated sphere Nusselt number (given by Ranz&Marshall [88]) $Nu_s = 2. + 0.6 Re^{0.5} Pr^{\frac{1}{3}}$, noted $\frac{\langle Nu \rangle}{Nu_s}$, is compared to existing literature results. This comparison, illustrated in Figure 4.11, shows a nice match with Massol [70] results at different Reynolds number and for a large range of solid volume fraction ($0.05 \leq \alpha_d \leq 0.6$). A good agreement is also observed with Gun [47] correlation for low loading of sphere ($\alpha_d \leq 0.15$), which means that for this range of α_d , the FCC configuration is a good approximation of uniform flow past a random assembly of spheres.

This study shows the strong dependence of the global Nusselt number to the solid volume fraction and Reynolds number. Indeed, increasing the solid volume fraction increases the blocking effect which thins the thermal boundary layer and at the same time, increases the temperature gradient and consequently the Nusselt number. This effect is enhanced significantly with solid volume fraction becoming larger. Indeed, Nusselt number for a sphere in FCC configuration can be five times the one of an isolated sphere for high particle concentrations.

4.5 Finite size random arrangement of spheres in a channel

In order to assess the ability of the presented method to deal with more complex particulate flows, the last case studied in this work is a uniform channel flow past

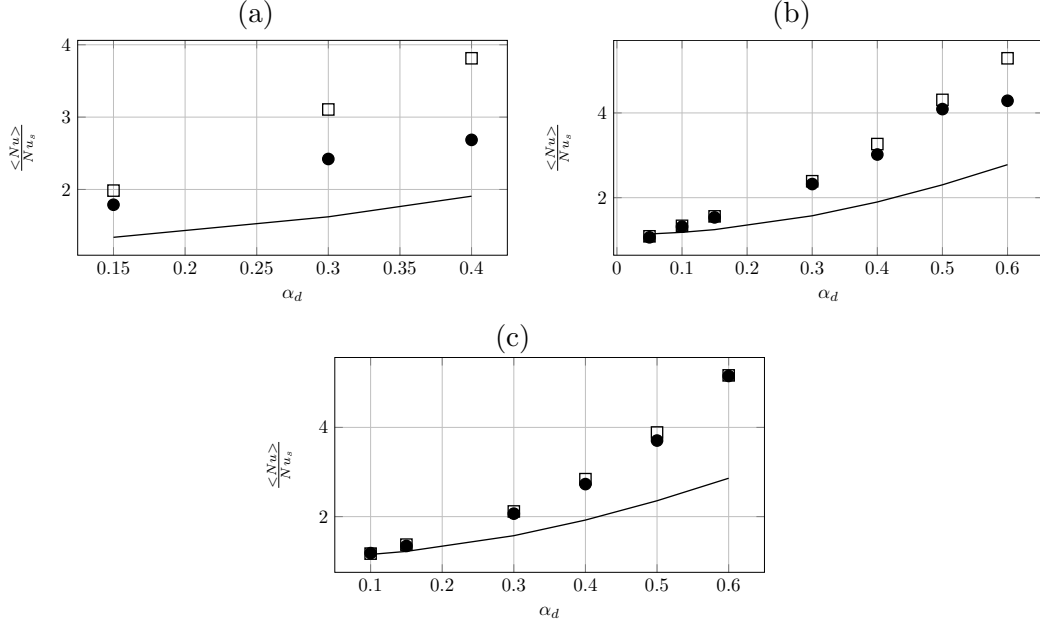


Figure 4.11: Global Nusselt coefficient for a uniform flow past a FCC, normalized by Ranz&Marshall [88] Nusselt coefficient for a uniform flow past an isolated sphere. Evolution as a function of the solid volume fraction α_d at Reynolds numbers (a) $Re = 10$, (b) $Re = 50$, (c) $Re = 100$: (—) Gunn [47], (\square) Massol [70], (\bullet) present work.

a random assembly of fixed hot spheres of diameter d (illustrated in Figure 4.12). The computational domain lengths are $L_x = 9d$ and $L_y = L_z = 5d$, where, given a solid volume fraction α_d , the particles are randomly distributed in the sub-domain $[(2d, 0, 0); (7d, 5d, 5d)]$, using hard sphere collisions model [22] to prevent them from overlapping. A cold fluid flows through the channel in x-direction (streamwise), by imposing at the inlet a temperature T_∞ and a velocity $U_\infty \mathbf{x}$ deduced from the Reynolds number $Re = \frac{U_\infty d}{\nu}$. Periodic boundary conditions are imposed in cross-wise directions. The N_p spheres are maintained at a constant temperature T_s , the number of spheres is deduced from the solid volume fraction by $N_p = \frac{6}{\pi} \left(\frac{L_y}{d}\right)^3 \alpha_d$.

A fixed bed Nusselt number is considered here. It is defined as an average of individual particle Nusselt numbers:

$$\langle Nu \rangle = \frac{1}{N_p} \sum_i^{N_p} \frac{(Q_p)_i}{(T_s - \langle T \rangle_f)_i \pi d^2} \quad (4.16)$$

where $(Q_p)_i$ is the i^{th} sphere heat flux given by 'Eq. 4.7'. Estimating the local average temperature of the fluid $\langle T \rangle_f)_i$ is not straightforward. As suggested by

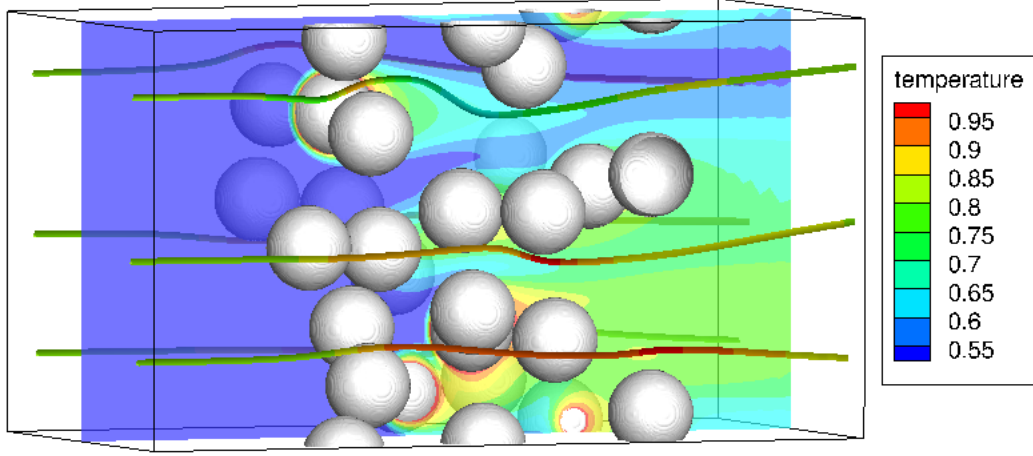


Figure 4.12: Streamlines and temperature field of a channel steady flow along the x-axis of a random array of spheres at $Re = 100$ and $\alpha_d = 0.1$.

Deen *et al.* [36], a good estimate is given by:

$$\langle T \rangle_f = \frac{\iiint (1 - C) T g_i(r)}{\iiint (1 - C) g_i(r)} \quad (4.17)$$

where T , C are the temperature field and color function respectively, and $g_i(r)$ is the filter that cover the fluid volume in a $4d$ length box containing the i^{th} sphere, both having the same center. It is given by:

$$g_i(r) = \exp\left(\frac{-2r}{d}\right), \quad 0 < r < 2d \quad (4.18)$$

Simulations of uniform flow past a random hot spheres were performed for low solid volume fractions $\alpha_d = 0.05, 0.1$ at different Reynolds numbers $Re = 10, 50, 100$. Their results are compared to the following correlations:

- Gun [47]:

$$Nu = \left(7 - 10(1 - \alpha_d) + 5(1 - \alpha_d)^2\right) \left(1 + 0.7Re^{0.2}Pr^{\frac{1}{3}}\right) + \left(1.33 - 2.4(1 - \alpha_d) + 1.2(1 - \alpha_d)^2\right) Re^{0.7}Pr^{\frac{1}{3}}$$

- Deen *et al.* [37]:

$$Nu = \left(7 - 10(1 - \alpha_d) + 5(1 - \alpha_d)^2\right) \left(1 + 0.17Re^{0.2}Pr^{\frac{1}{3}}\right) + \left(1.33 - 2.31(1 - \alpha_d) + 1.16(1 - \alpha_d)^2\right) Re^{0.7}Pr^{\frac{1}{3}}$$

- Sun *et al.* [99]:

$$Nu = \frac{\left(-0.46 + 1.77(1 - \alpha_d) + 0.69(1 - \alpha_d)^2\right)}{(1 - \alpha_d)^3} + \left(1.37 - 2.4(1 - \alpha_d) + 1.2(1 - \alpha_d)^2\right) Re^{0.7}Pr^{\frac{1}{3}}$$

Figure 4.13 shows that our results are in the same range of values than the results given in the literature, which is very encouraging as first results of real particle flow arrangements.

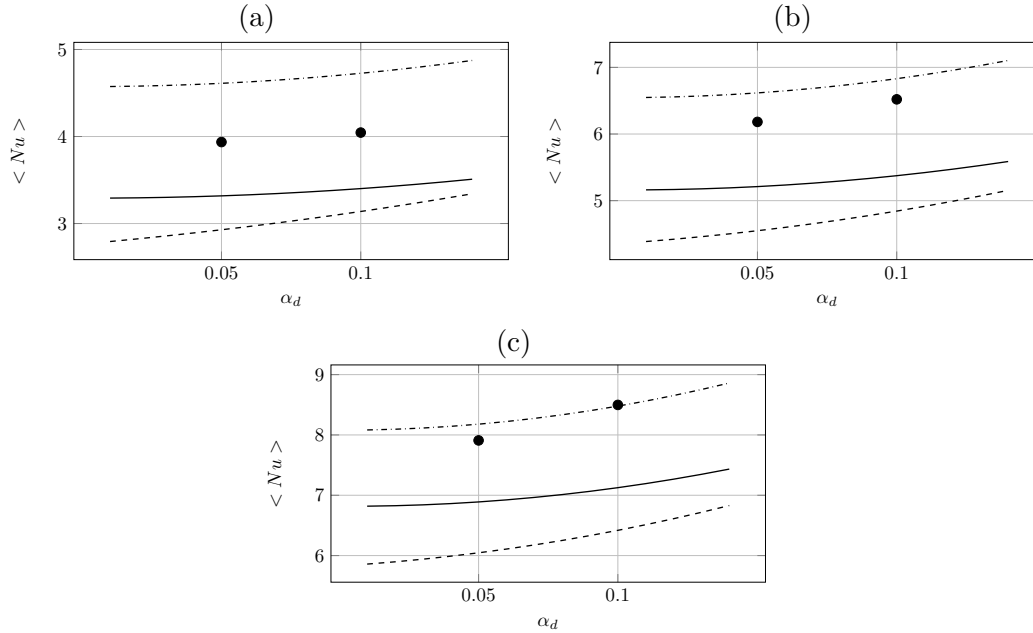


Figure 4.13: Nusselt coefficient for a uniform flow past a random arrangement of hot spheres as a function of the solid volume fraction α_d at the Reynolds numbers (a) $Re = 10$, (b) $Re = 50$, (c) $Re = 100$: (---) Gunn [47], (—) Deen *et al.* [37], (---) Sun *et al.* [99] and (●) present work.

4.6 Conclusion

In the framework of a finite-size particle approach, an accurate procedure for the calculation of heat transfer coefficients for motions around fixed particles has been proposed based on third order Lagrange extrapolation coupled to third order Taylor interpolation methods. This method is an extension of the techniques proposed for drag force estimates published in [24]. The procedure allowing the estimate of heat transfer coefficients at a particle surface has been validated with success on fixed isolated spheres, FCC and random arrangements of spheres. Comparisons have been presented to reference Nusselt correlation of the literature.

Future works will be devoted to applying our heat transfer calculation method to arrangements of ellipsoidal particles and extracting correlation laws for these configurations. Other interesting lines of work concern the use of our method in the context of other resolved-scale particle methods such as IBM.

Chapter 5

Drag, lift and Nusselt coefficients for ellipsoidal particles using particle-resolved direct numerical simulations

This chapter is the article [25] authored by M.-A. Chadil, S. Vincent and J.-L. Estivalezes

Abstract

Particle-Resolved Direct Numerical Simulations has been performed using an implicit tensorial viscous penalty method applied to ellipsoidal particles. Based on the simulations, the drag and lift forces exerted by the fluid on the particles and the Nusselt number of the particles has been extracted. The simulations results are compared to existing correlations for a single ellipsoid by changing the incident angle at different Reynolds number. A new Lagrange extrapolation coupled to a Taylor interpolation of high order are used to calculate the drag and lift forces as well as the heat flux. This work is an extension of preliminary studies for a spherical particle [23, 24]. A simple correlation is proposed for the Nusselt number of a prolate spheroid with aspect ratio of 2.5 and Reynolds number between 10 and 100.

5.1 Introduction

Multiphase flows involving solid particles can be met in various natural phenomena such as volcanic eruptions [10, 33] but also in numerous industrial processes such as petroleum refining, blast furnaces or chemical looping combustion [2, 67, 71], fluid catalytic cracking reactors [3], gas phase polymerization reactors [46] and fluidized beds [77, 109].

The simulation of such particulate motions is based, at the real problem scale, on statistical approaches due to the huge disparity of scales between the particle

and the macroscopic size of the process. These simulations are carried out using macroscopic Eulerian-Eulerian or mesoscopic Eulerian-Lagrangian models for which the average interphase transfer of momentum and energy between the fluid and the particles need to be modeled.

Numerous well-known drag force laws are classically used in large scale models. Among them, we can cite Schiller and Naumann [97] correlation for a single sphere whereas for fixed and fluidized beds of spheres, the correlations proposed by Ergun [42] and Wen&Yu [114] are often utilized. Heat transfers have also extensively been modeled for a single sphere using Ranz & Marshall [88] correlation, as well as for random arrangements of spheres with Gunn [47] law, to name the most famous of them. However, spherical particles are rarely encountered in both natural and industrial processes, and particle non-sphericity can affect not only the structure of the particle aggregates but also the velocity and the temperature of the fluid by changing the momentum and heat transfer between the fluid and the particles [50]. Therefore, many studies were conducted in the past decades in order to characterize the non-sphericity effect on gas-solid flows and to adapt existing hydrodynamic force and heat transfer correlations for non-spherical particles at larger scales.

Since the nineteenth century, many theoretical and experimental works on the hydrodynamic forces acting on non-spherical particles have been conducted. Indeed, Oberbeck (1876) [75], Jeffery (1922) [58], Venkates (1961) [107], Breach (1961) [15] and Brenner (1963)[16] theoretically derived the forces acting on particles of different shapes in Stokes regime. Although these studies have to be restricted to low Reynolds numbers [69], they are often used to model the motion of non-spherical particles. The use of these models for estimating the forces acting on non-spherical particles is almost unavoidable since there are few available correlations which predict all the coefficients (drag, lift and torque) as a function of the particle orientation at higher Reynolds number regimes. Chhabra *et al.* (1999) [28] were the first to compile and classify the most used of these correlations. They showed that some discrepancies exist between them. Recently, several studies based on Particle-Resolved Direct Numerical Simulations (PR-DNS) have been conducted in order to propose new hydrodynamic force coefficients for different particle shapes and a large range of particle Reynolds number. Hölzer and Sommerfeld (2008) [55] derived a correlation for the drag coefficient of arbitrary shaped particles using a large number of experimental data and their Lattice Boltzmann (LBM) simulation results [54]. Later, Zastawny *et al.* (2011) [116] proposed correlations for drag, lift and torque coefficients extracted from Immersed Boundary Method (IBM) simulations. More recently, Ouchene *et al.* [76] proposed a correlation for these coefficients as well. They used body fitted simulations conducted with ANSYS FLUENT commercial code. To our knowledge, the last work proposed in this purpose was Sanjeevi *et al.* [92] correlations extracted from LBM simulations.

Otherwise, rare are the studies for which a correlation for the Nusselt number or the heat transfer coefficient between non-spherical particles and fluid is considered. Indeed, Kishore *et al.* [61] and Richer *et al.* [89] proposed a correlation for an aver-

aged Nusselt number over the attack angle α for a uniform flow past an ellipsoidal particle. Later, Richer *et al.* [90] suggested a correlation for the Nusselt number of an isolated ellipsoidal particle as function of its attack angle α with respect to the flow direction.

The main purpose of the present work is to use a particle-resolved Implicit Tensorial Penalty Method (ITPM) [21, 26, 86, 109] to simulate flows and heat transfers interacting with ellipsoidal particles in various flow regimes. Once these small scale simulations have been conducted, the accurate estimate of forces and heat transfers acting at the ellipsoidal particle surface will be accurately estimated by means of high order Taylor interpolations and Lagrange extrapolations of third order first proposed for spheres in [23, 24]. If possible, correlations of drag, lift or Nusselt will be proposed according to ellipsoidal particle orientation or Reynolds number.

The structure of this manuscript is as follows. In section 5.2, the model and numerical methods used in the ITPM are briefly recalled and an extension of the force and Nusselt calculation to ellipsoidal particles is proposed. Thereafter, section 5.3 is devoted to estimating drag, lift and Nusselt for uniform flows around an isolated ellipsoidal particle. Comparisons to existing correlations of the literature are investigated and a new Nusselt correlation is considered for various Reynolds and attack angles. Conclusions are finally drawn in section 5.4.

5.2 Numerical Methodology

Conservation equations

Following the work of Vincent and co-workers on the generalization of the two-phase Navier-Stokes equations [63, 109] for particulate flows, the non-isothermal motion equations for incompressible flows interacting with resolved-scale particles are

$$\nabla \cdot \mathbf{u} = 0 \quad (5.1)$$

$$\rho \left(\frac{\partial \mathbf{u}}{\partial t} + (\mathbf{u} \cdot \nabla) \mathbf{u} \right) = -\nabla p + \rho \mathbf{g} + \nabla \cdot \left[\mu (\nabla \mathbf{u} + \nabla^t \mathbf{u}) \right] \quad (5.2)$$

$$\rho C_p \left(\frac{\partial T}{\partial t} + \mathbf{u} \cdot \nabla T \right) = \nabla \cdot (k_f \nabla T) \quad (5.3)$$

where \mathbf{u} is the velocity, p the pressure, T the temperature, t the time, \mathbf{g} the gravity vector, ρ , μ , C_p and k_f respectively the density, the viscosity, the specific heat and the thermal conductivity of the equivalent fluid. By equivalent fluid, we mean that the Eulerian simulation mesh will be fixed and that the local cells properties ρ , μ , C_p and k_f will potentially change according time (moving particles not considered in this work) depending on a local solid fraction C . This phase function is obtained by projecting the shape of the particles on the Eulerian fixed mesh.

In a first approach, only motionless particles are considered in this work. On a numerical point of view, they are fixed by imposing the velocity of the Eulerian cells

near their centroids to zero, and the viscous penalty method propagates the zero velocity in the whole solid medium. The particle temperatures will be considered constant over time, they are imposed at a fixed value in the whole solid medium.

Ellipsoidal particles

Ellipsoids are shaped using the solid fraction or phase function C which is computed by browsing the Eulerian mesh and assessing each point whether it is in the ellipsoid ($C = 1$) or not ($C = 0$). To project the particle shape on the Eulerian solving grid, an equation for the ellipsoid is used: lets have an ellipsoid E centred at \mathbf{x}_0 , Σ a diagonal matrix such that $\Sigma_{ii} = \frac{1}{\sigma_i}$, σ_i being the length of the ellipsoid i^{th} semi-axis, thus all points belonging to the ellipsoid E verify [82]:

$$E = \left\{ \mathbf{x} \mid \|\Sigma R(q)^T (\mathbf{x} - \mathbf{x}_0)\| \leq 1 \right\} \quad (5.4)$$

where :

$$R(q) = \begin{pmatrix} 1 - 2(q_2^2 + q_3^2) & 2q_1q_2 - 2q_0q_3 & 2q_0q_2 + 2q_1q_3 \\ 2q_1q_2 + 2q_0q_3 & 1 - 2(q_1^2 + q_3^2) & 2q_2q_3 - 2q_0q_1 \\ 2q_0q_2 + 2q_1q_3 & 2q_2q_3 + 2q_0q_1 & 1 - 2(q_1^2 + q_2^2) \end{pmatrix} \quad (5.5)$$

is the rotation matrix based on the quaternion $q = [q_0, q_1, q_2, q_3]$. Quaternions, introduced by Sir Hamilton[49], are used to characterize a rotation and to prevent the Gimbal Lock problem [52] encountered when Euler angles are used. So, given a rotation of an angle α and a direction $\mathbf{e} = (e_1, e_2, e_3)$, its quaternion is:

$$q = \left[\cos\left(\frac{\alpha}{2}\right), \sin\left(\frac{\alpha}{2}\right) e_1, \sin\left(\frac{\alpha}{2}\right) e_2, \sin\left(\frac{\alpha}{2}\right) e_3 \right]$$

Hydrodynamic force and Heat flux computation for immersed boundary methods

The computation for a spherical particles of the hydrodynamic force $\mathbf{F} = \oint_S \bar{\bar{\sigma}} \cdot \mathbf{n} \, dS$ and the heat flux $Q_p = \oint_S -k_f \nabla T \cdot \mathbf{n} \, dS$, was fully detailed in [24] and [23] respectively. It consists in discretizing the particle surface S by a set of N elements called Lagrangian mesh (see figure 5.1), such that:

$$\mathbf{F} \approx \sum_l^N \bar{\bar{\sigma}}_l \cdot \mathbf{n}_l \, dS_l \quad (5.6)$$

$$Q_p \approx \sum_l^N -K_f (\nabla T)_l \cdot \mathbf{n}_l \, \Delta S_l \quad (5.7)$$

where the ongoing normal to the l^{th} element \mathbf{n}_l and its area ΔS_l are deduced from its node coordinates. On the other hand, the stress tensor $\bar{\sigma}_l$ and the temperature gradient $(\nabla T)_l$ are not known at the l^{th} element center C_l given that the pressure p , the velocity \mathbf{u} and the temperature T are located on the fixed structured Eulerian mesh. Moreover, we have observed that the velocity and the pressure values [24] as well as the temperatures [23] are inaccurate in the cells cut by the fluid/solid interface, therefore we have to extrapolate the stress tensor and the temperature gradient from the Eulerian mesh nodes far from the particle to the surface. A third order Lagrange extrapolation (illustrated in 5.1 left) is used to achieve that [23, 24]:

$$f(\mathbf{C}_l) = \sum_{i=1}^3 f(\mathbf{P}_i) L_i(\mathbf{C}_l) \quad , \quad \text{where} \quad L_i(\mathbf{C}_l) = \prod_{j \neq i} \frac{|\mathbf{C}_l - \mathbf{P}_j|}{|\mathbf{P}_i - \mathbf{P}_j|} \quad (5.8)$$

f being the stress tensor components in the force computation $\bar{\sigma}_{ij}$ or the temperature gradient components $(\nabla T)_i$ in the heat transfer computation. A third order Taylor interpolation (illustrated in 5.1 right) is used to interpolate them at the extrapolation points P_1 , P_2 and P_3 [23, 24]:

$$\begin{aligned} f(\mathbf{P}_k) = & f(\mathbf{E}) + \frac{\partial f}{\partial x_i}(\mathbf{E})((\mathbf{C}_l)_i - \mathbf{E}_i) + \frac{1}{2} \frac{\partial^2 f}{\partial x_i^2}(\mathbf{E})((\mathbf{C}_l)_i - \mathbf{E}_i)^2 \\ & + \frac{\partial^2 f}{\partial x_i \partial x_j}(\mathbf{E})((\mathbf{C}_l)_i - \mathbf{E}_i)((\mathbf{C}_l)_j - \mathbf{E}_j) + O(\|\mathbf{C}_l - \mathbf{E}\|^3) \end{aligned} \quad (5.9)$$

where \mathbf{E} is the nearest Eulerian point to \mathbf{P}_k .

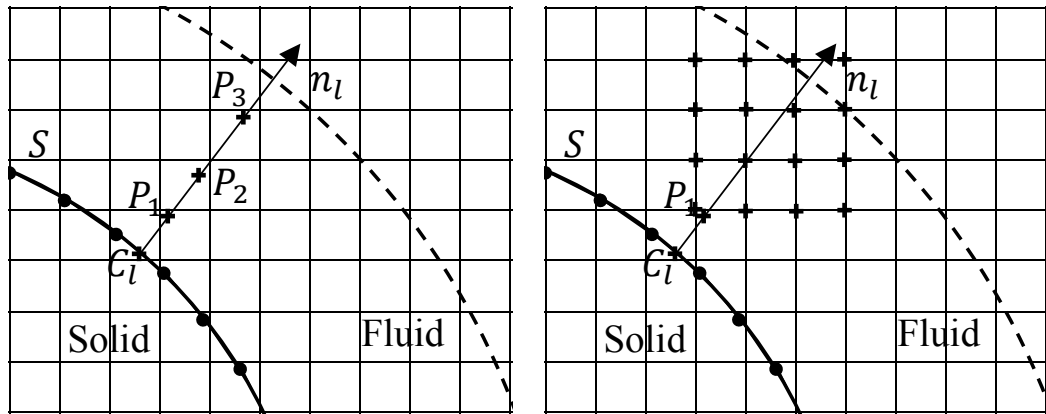


Figure 5.1: Details of the third order Lagrange extrapolation (left) and the third order Taylor interpolation (right), used in heat flux computation.

5.3 Drag, Lift and Nusselt for an isolated stationary ellipsoid past by a uniform flow

The hydrodynamic force \mathbf{F} exercised by the fluid on the ellipsoid is extracted from the pressure and the velocity fields, solution of the Navier-Stokes equations 5.1,5.2, using the method presented in the previous section 5.2. Two non-dimensional coefficients are introduced to characterize this force: the drag coefficient $C_d = \frac{\mathbf{F} \cdot \mathbf{x}}{0.5\rho U_\infty^2 A_p}$

and lift coefficient $C_l = \frac{\mathbf{F} \cdot \mathbf{x}^\perp}{0.5\rho U_\infty^2 A_p}$, with U_∞ the velocity of the undisturbed fluid

far from the particle, ρ the fluid density and $A_p = \frac{\pi d_{eqV}^2}{4}$ the cross-sectional area of the sphere, of diameter d_{eqV} , having the same volume than the ellipsoid, as in previous studies [55, 76, 93, 116]. On the other hand, the heat transfer between the hot ellipsoid and the fluid, considered across the particle surface, is characterized by the non-dimensional Nusselt number $Nu = \frac{Q_p d_{eqS}}{k_f (T_s - T_f) S_p}$, where Q_p is the heat flux extracted from the temperature field using the method of the previous section 5.2. Here, T_s and T_f are the temperatures of the particle and the fluid respectively and $S_p = \pi d_{eqS}^2$ is the sphere, of diameter d_{eqS} . Attention, a nuance is introduced here, we propose that the sphere used to estimate Nu is having the same surface than the ellipsoid instead of the same volume. This choice is due to the fact that the heat flux is linked to the particle surface in contrary to the hydrodynamic force which is linked to the particle volume.

Simulation setup

A hot Spheroid of semi-axis a and b ($a > b$) and aspect ratio $r = \frac{a}{b} = 2.5$ (illustrated in Fig. 5.2) is immersed in a cold fluid for different attack angles α , *i.e.* rotation angle of the spheroid with respect to z axis. The simulations at different Reynolds number $Re = \frac{U_\infty d_{eqV}}{\nu}$ are driven with a computational domain whose lengths are $L_x = 16d_{eqV}$ and $L_y = L_z = 8d_{eqV}$ in each Cartesian direction. The Eulerian mesh refinement is constant in a box of extension $[(2d_{eqV}, 2d_{eqV}, 3d_{eqV}); (6d_{eqV}, 6d_{eqV}, 5d_{eqV})]$ centered around the particle position. Outside this box, the Eulerian mesh is exponentially coarsen from the box to the boundaries of the simulation domain. The inlet boundary conditions are $\mathbf{u} = U_\infty \mathbf{e}_x$, $T = T_\infty$ and Neumann conditions are applied elsewhere. As an example, the flow around a spheroid at $Re = 100$ and two different attack angle, $\alpha = 0$ and $\alpha = 90$, is shown in Figure 5.3.

As for the simulations of spherical particle [23, 24], the Eulerian mesh resolution is chosen so that the dynamic boundary layer contains 5 cells in order to ensure that the extrapolation points are in it (see in Fig. 5.1 left). This is a necessary condition to accurately compute the hydrodynamic force. Moreover, Prandtl number is imposed here at $Pr = 1$, to ensure that the thermal boundary layer has the same

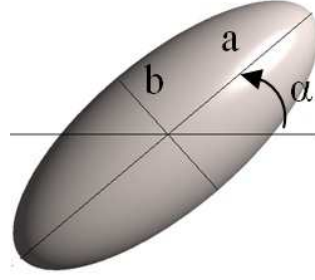


Figure 5.2: Illustration of an ellipsoid of aspect ratio $r = 2.5$ and attack angle $\alpha = 45$. The flow comes from the left.

width as the dynamic one. This way, it contains the extrapolation points as well. Therefore, the mesh resolution changes with the Reynolds number $\Delta x = \frac{d_{eq}V}{5\sqrt{Re}}$ according to scaling laws for laminar dynamic boundary layers.

Drag coefficient

The drag coefficient for an uniform flow past a hot spheroid is compared to various existing correlations, written as:

$$C_d = C_{d,\alpha=0} + (C_{d,\alpha=90} - C_{d,\alpha=0}) \sin^2 \alpha \quad (5.10)$$

with

- Sanjeevi *et al.* [92]:

$$C_{d,\alpha=0} = \left(\frac{23.1}{Re} + \frac{3.397}{Re^{0.364}} \right) e^{-0.0008Re} + 0.169 \left(1 - e^{-0.0008Re} \right) \quad (5.11)$$

$$C_{d,\alpha=90} = \left(\frac{27.93}{Re} + \frac{4.286}{Re^{0.234}} \right) e^{-0.0018Re} + 0.815 \left(1 - e^{-0.0018Re} \right) \quad (5.12)$$

- Zastawny *et al.* [116]:

$$C_{d,\alpha=0} = \frac{5.1}{Re^{0.48}} + \frac{15.52}{Re^{1.05}} \quad (5.13)$$

$$C_{d,\alpha=90} = \frac{24.68}{Re^{0.98}} + \frac{3.19}{Re^{0.21}} \quad (5.14)$$

- Ouchene *et al.* [76] found in [7] due to typographical errors in [76]:

$$C_{d,\alpha=0} = \frac{24}{Re} \left(K_{\alpha=0}(r) + 0.15r^{-0.8}Re^{0.687} + \frac{(r-1)^{0.63}}{24}Re^{0.41} \right) \quad (5.15)$$

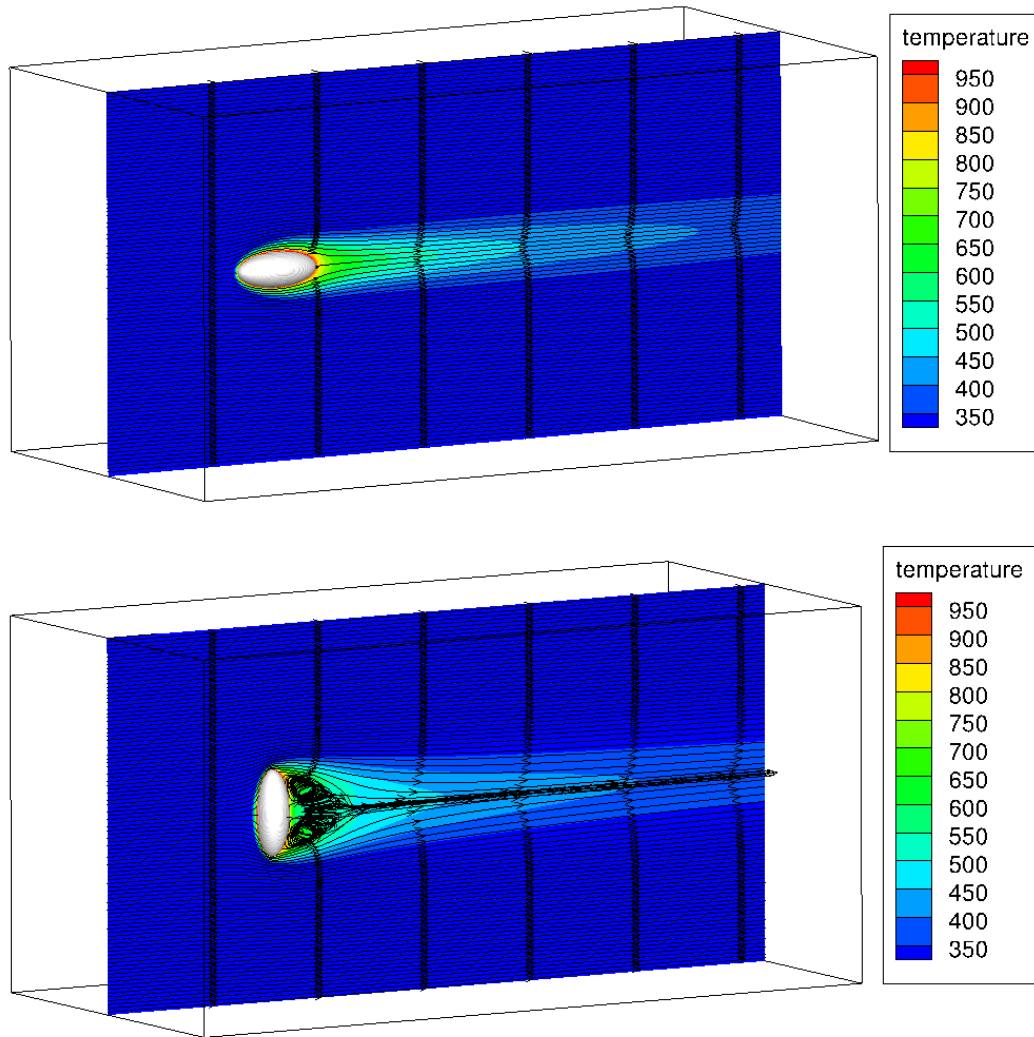


Figure 5.3: Illustration of instantaneous stream lines and temperature field obtained for an uniform flow past a hot isolated spheroid at $Re = 100$ for attack angles $\alpha = 0$ (top) and $\alpha = 90$ (bottom). The upstream unperturbed velocity U_∞ is imposed at the left boundary condition. Aspect ratio $r = 2.5$.

$$C_{d,\alpha=90} = \frac{24}{Re} \left(K_{\alpha=90}(r) + 0.15r^{-0.54} Re^{0.687} + \frac{r^{1.043}(r-1)^{-0.17}}{24} Re^{0.65} \right) \quad (5.16)$$

where:

$$K_{\alpha=0}(r) = \frac{\frac{8}{3}r^{-\frac{1}{3}}}{\frac{-2r}{r^2-1} + \frac{2r^2-1}{(r^2-1)^{\frac{3}{2}}} \ln \left(\frac{r+\sqrt{r^2-1}}{r-\sqrt{r^2-1}} \right)}$$

$$K_{\alpha=90}(r) = \frac{\frac{8}{3}r^{-\frac{1}{3}}}{\frac{r}{r^2-1} + \frac{2r^2-3}{(r^2-1)^{\frac{3}{2}}} \ln \left(r + \sqrt{r^2-1} \right)}$$

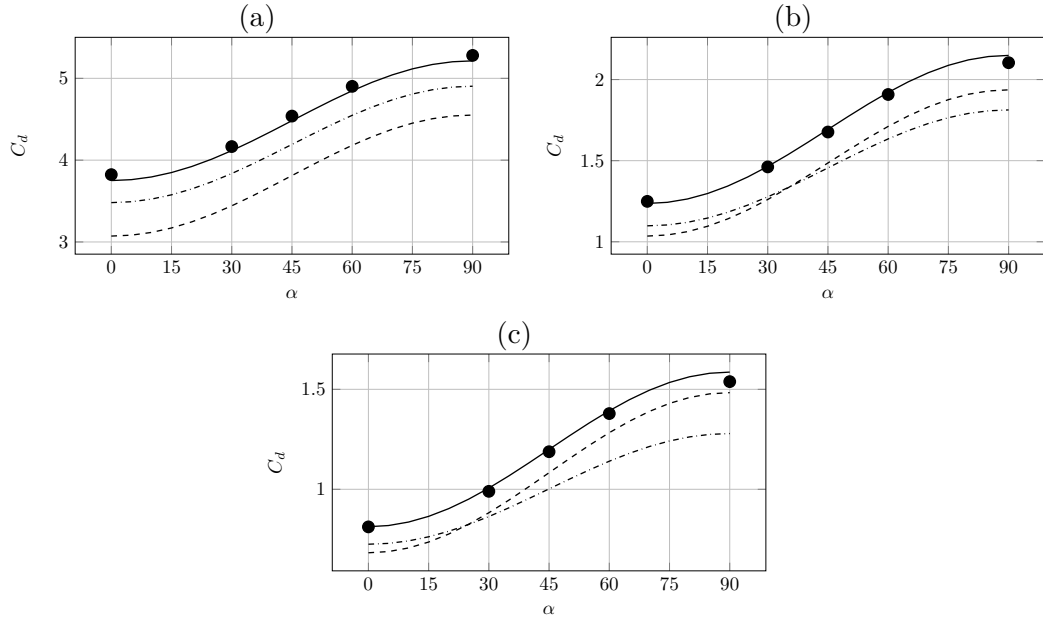


Figure 5.4: Drag coefficient for an uniform flow past a spheroid as a function of the attack angle α at different Reynolds numbers: (a) $Re = 10$, (b) $Re = 50$, (c) $Re = 100$. (—) Sanjeevi *et al.* [92], (---) Zastawny *et al.* [116], (-.-) Ouchene *et al.* [76] and (●) present work.

Figure 5.4 shows the drag force for an uniform flow past a spheroid as a function of the attack angle α at different Reynolds numbers. It can be observed that our results matches nicely the correlation of Sanjeevi *et al.* [92], extracted from LBM simulations. Sanjeevi *et al.* [92] simulations were carried out after a grid resolution and a domain independence studies. Moreover, our results are in good agreement with the correlation of Zastawny *et al.* [116], extracted from IBM simulations, for high Reynolds number. However, this correlation seems to be less adapted for lower Reynolds number. This was also observed by Sanjeevi *et al.* [92] for $R = 0.1$. To finish with, the results of Ouchene *et al.* [76], extracted from ANSYS FLUENT simulations, seems to be less accurate especially for $\alpha = 90^\circ$, which certainly affects the obtained values for α smaller than 90° through Eq. (5.10).

The present study validates the drag force computation for ellipsoidal particles simulated using a viscous penalty method.

Lift coefficient

The lift coefficient for an uniform flow past a hot spheroid, extracted from the previous simulations, is compared to the following correlations:

- Sanjeevi *et al.* [92]:

$$C_l = \left(\frac{4.484}{Re} + \frac{1.326}{Re^{0.122}} \right) \sin \alpha^{(1+0.016Re^{0.286})} \cos \alpha^{(1-0.01Re^{0.332})} \quad (5.17)$$

- Zastawny *et al.* [116]:

$$C_l = \left(\frac{6.079}{Re^{0.898}} + \frac{0.704}{Re^{-0.028}} \right) \sin \alpha^{(1.067+0.0025Re^{0.818})} \cos \alpha^{1.049} \quad (5.18)$$

- Ouchene *et al.* [7, 76]:

$$C_l = \left(F(r)Re^{0.25} + \frac{G(r)}{Re^{0.755}} \right) \sin \alpha^{(1.002Re)} \cos \alpha \quad (5.19)$$

where:

$$F(r) = 0.1944 \left(r^{-0.93} - 1 \right) \ln(r) + 0.2127(r - 1)^{0.47}$$

$$G(r) = 1.9183r^{\ln(r)} - 4.0573 \left(r^{-1.61} - 1 \right)$$

The lift coefficient results are compared in Figure 5.5 for an uniform flow past a spheroid. They are presented at different Reynolds numbers as function of the attack angle α . It can be observed, as in Drag coefficient results (see Figure 5.4), that our results are in good agreement with those of Sanjeevi *et al.* [92] and those of Zastawny *et al.* [116]. However, the Ouchene *et al.* [76] correlation seems, as for drag correlation, less accurate. This could be due to inaccurate results or insufficient mesh resolution for some cases simulated to extract their correlations or, as suggested by Sanjeevi *et al.* [92], it could be an effect of their method to fit the body fitted simulation data.

Nusselt coefficient

The Nusselt number for an uniform flow past a hot ellipsoid was rarely studied and few correlations exist for it: [61] and [89] gave a correlation for a Nusselt number averaged over the attack angle α and [90] proposed a correlation of the Nusselt number for an aspect ratio $r = 2$, which makes a comparison with this correlation impossible given that $r = 2.5$ in our work.

In a preliminary approach, a first order correlation of the Nusselt number is proposed for a uniform flow past a spheroid of aspect ratio $r = 2.5$ at Prandlt

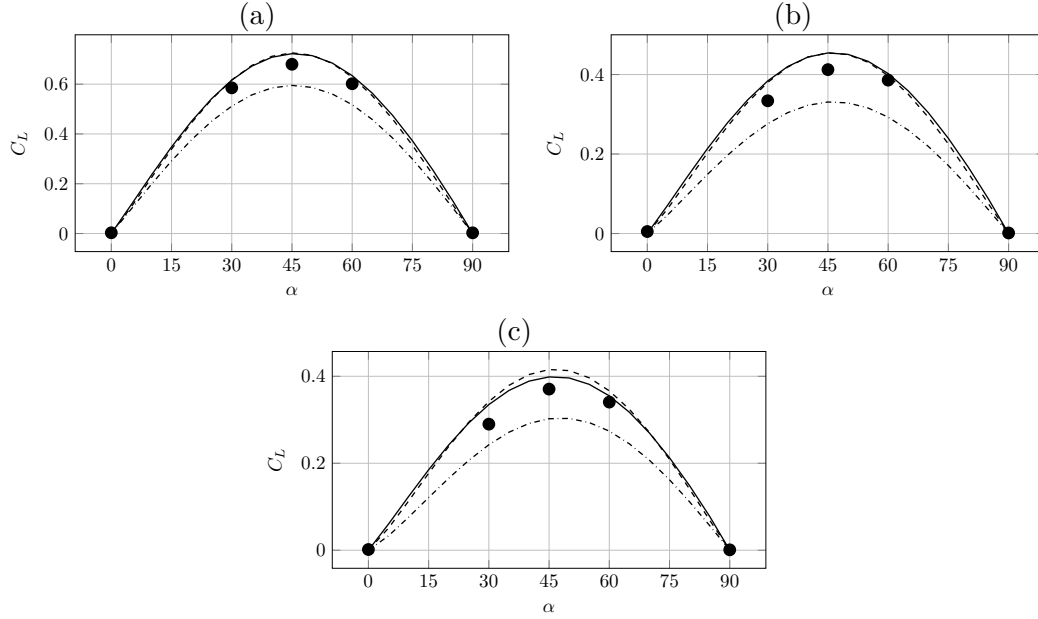


Figure 5.5: Lift coefficient for an uniform flow past a spheroid as a function of the attack angle α at different Reynolds numbers: (a) $Re = 10$, (b) $Re = 50$, (c) $Re = 100$. (—) Sanjeevi *et al.* [92], (---) Zastawny *et al.* [116], (-.-) Ouchene *et al.* [76] and (●) present work.

number $Pr = 1$. Our correlation is expressed according to the Ranz & Marshall [88] Nusselt number correlation for a sphere having the same surface than the ellipsoid. Ranz & Marshall [88] correlation is given by:

$$Nu_s = 2. + 0.6 Re^{0.5} Pr^{\frac{1}{3}} \quad (5.20)$$

Our proposed correlation is written as:

$$Nu = Nu_s \left(8.53 \cdot 10^{-1} + 3.68 \cdot 10^{-4} Re + \alpha \left(4.2 \cdot 10^{-4} + 1.24 \cdot 10^{-5} Re \right) \right) \quad (5.21)$$

Figure 5.6 shows the simulated Nusselt number for an uniform flow past a hot spheroid compared to the proposed correlation Eq. 5.21. The maximum error to the correlation is 2.5% for a spheroid oriented with $\alpha = 60^\circ$ at Reynolds number $Re = 50$.

5.4 Conclusion

The viscous penalty method was utilized to perform resolved scale particle simulation of the flow and associated heat transfers past a spheroid at various Reynolds numbers and attack angles. For all considered quantities (drag and lift coefficients, Nusselt numbers), our simulations are validated favorably against correlations of the literature. It has been demonstrated that the results of Sanjeevi *et al.* [92]

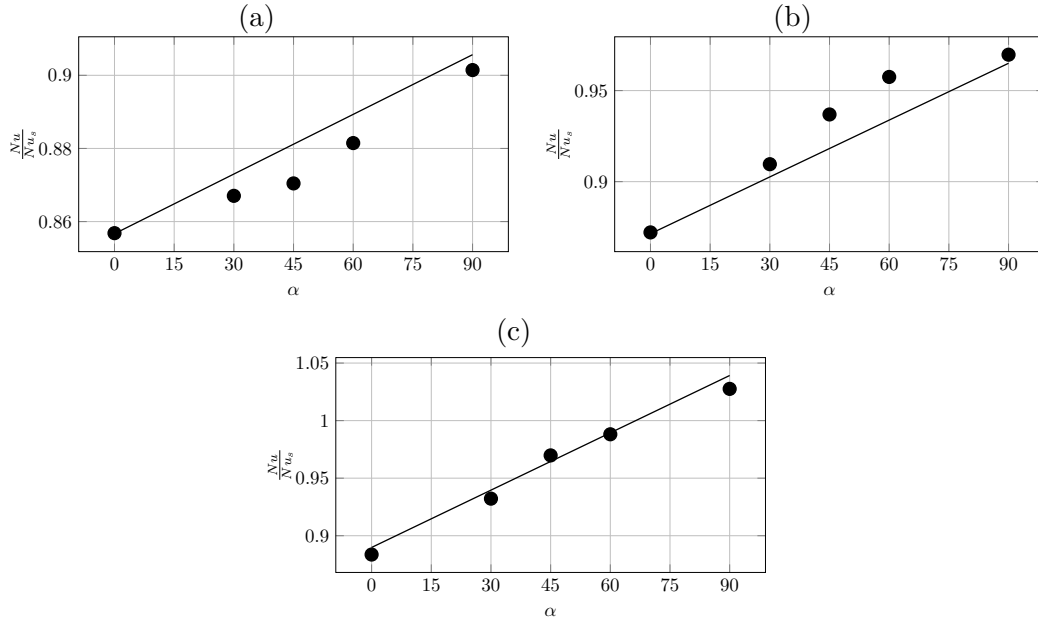


Figure 5.6: Nusselt coefficient for an uniform flow past a spheroid as a function of the attack angle α at different Reynolds numbers: (a) $Re = 10$, (b) $Re = 50$, (c) $Re = 100$. (●) simulation results and (—) proposed correlation Eq. (5.21).

and Zastawny *et al.* [116] are in good agreement with our simulations while the correlation of Ouchene *et al.* [76] under predicts force coefficients.

A new Nusselt correlation has been proposed for ellipsoids. IT fits nicely the resolved scale particle simulations. This work has to be completed and extended to various flow configurations, Reynolds numbers and attack angle in order to generalize the Nusselt correlation. We have illustrated the interest of leading fully resolved particle simulations to extract macroscopic physical correlations such as on Nusselt.

Chapter 6

Novel method to compute drag force and heat transfer for motions around spheres

This chapter is the article [27] authored by M.-A. Chadil, S. Vincent and J.-L. Estivalezes

Abstract

A viscous penalty method is used to simulate the interaction between spheres and flows with Particle-Resolved Direct Numerical Simulations. An original method has been developed and validated in order to extract from these simulations the hydrodynamic forces and heat transfers on immersed boundaries representing the particles thanks to Aslam extensions [9]. This method is an improvement of a previous work based on Lagrange extrapolations [23, 24]. Comparisons between these two approaches are considered on various incompressible motions such as the flow around an isolated particle at various Reynolds numbers and flows across packed spheres under Faced-Centered Cubic mono- and bi-disperse arrangements.

6.1 Introduction

Fluid/Solid flows are widely encountered in nature as well as in various industrial processes. Among the wide variety of applied problems, we can cite volcanic eruptions [10, 33], oil refining, blast furnaces or chemical looping combustion [2, 67, 71], fluid catalytic cracking reactors [3], gas phase polymerization reactors [46] and fluidized beds [77, 109]. Their modeling and simulation at the application scale are generally based on statistical approaches where macroscopic Eulerian-Eulerian or mesoscopic Eulerian-Lagrangian models (the average interphase transfer of momentum and energy between the fluid and the particles) are needed to be modeled.

Numerous well-known drag force laws are classically used in large scale models. The most popular are Schiller and Naumann [97] correlation for a single sphere

whereas for fixed and fluidized beds of spheres, the correlations proposed by Ergun [42] and Wen and Yu [114] are often utilized. Heat transfers have also extensively been modeled for a single sphere using Ranz and Marshall [88] correlation, as well as for random arrangements of spheres with Gunn [47] law, to name the most famous of them.

Particle-Resolved Direct Numerical Simulation (PR-DNS) has been the privileged tool of many researchers in order to model unclosed terms in macroscopic statistical equations. Many numerical approaches have been developed to perform PR-DNS of gas-solid flows. These can be classified in two types of approaches. The first one rely on body-fitted mesh to impose boundary conditions at particle surface. Many codes use this technique, as for instance AVBP code [98] used by Massol [70] to conduct his work. The second type of approaches is called Fictitious domain methods. They employ a fixed Cartesian grid in the whole domain, where each phase is located thanks to phase or color function $C = 1$ in the solid phase and $C = 0$ in the fluid phase. It is utilized in Lattice Boltzmann approach [12, 51, 53, 64, 65]. Another class of very popular fictitious domain method for handling finite-size particle on fixed meshes is the Immersed Boundary Method (IBM) [36, 102, 105, 106, 113, 116]. The approach used in this work is the Viscous Penalty Method [26, 109]. We have recalled here the most used methods in the literature.

The treatment of the fluid/solid interface in Navier-Stokes equations results in contaminated solution fields that do not correspond to unmodified Navier-Stokes equations. Tenneti *et al.* [103] proposed what they called the PUReIBM method where the immersed boundary (IB) forcing is restricted to the Eulerian grid points that lie in the solid phase, ensuring that the flow solution in the fluid phase is uncontaminated by the IB forcing. This allows them to easily compute drag forces [103] and heat transfers [99, 104]. In the case of VPM that we consider, we proposed, in a previous work [24], a Lagrange extrapolation for the drag force computation in order to reach the uncontaminated fluid area far from the particle/fluid interface ensuring in that way accurate results for drag coefficients. This method was used also in the heat transfer computation [23], and extended to ellipsoidal particles [25].

The purpose of this work is to propose an original alternative to Lagrange extrapolation in the hydrodynamic force and heat transfer computation in order to avoid contaminated solution of the Navier-Stokes equations near the solid-fluid interface. This original method is based on Aslam extension [9] to extrapolate velocity, pressure and temperature from the uncontaminated fluid area to the interface.

This paper is structured as follows. In section 6.2, the model and numerical methods used in the VPM are briefly recalled and a description as well as a validation of Aslam extension are detailed. Thereafter, section 6.3 is devoted to setting up Aslam extension numerical parameters and estimating drag and Nusselt coefficient for uniform flows around an isolated sphere and comparing them to those given by Lagrange extrapolation in order to assess the improvements made by Aslam extension. The same study is presented in section 6.4 for flows through fixed ar-

rangements of mono- and bi-dispersed spheres. Conclusions are finally drawn in section 6.5.

6.2 Numerical Methodology

6.2.1 Conservation equations

As explained by [26, 109], the motion equations describing incompressible two-phase flows that involve a carrier fluid and a solid particle phase are based on the one-fluid model. Their formulation is given by:

$$\nabla \cdot \mathbf{u} = 0 \quad (6.1)$$

$$\rho \left(\frac{\partial \mathbf{u}}{\partial t} + (\mathbf{u} \cdot \nabla) \mathbf{u} \right) = -\nabla p + \rho \mathbf{g} + \nabla \cdot \left[\mu (\nabla \mathbf{u} + \nabla^t \mathbf{u}) \right] \quad (6.2)$$

$$\rho C_p \left(\frac{\partial T}{\partial t} + \mathbf{u} \cdot \nabla T \right) = \nabla \cdot (k_f \nabla T) \quad (6.3)$$

where \mathbf{u} is the fluid or solid velocity, p the pressure, T the temperature, t the time, \mathbf{g} the gravity vector, ρ , μ , C_p and k_f respectively the density, the viscosity, the specific heat and the thermal conductivity of the equivalent fluid depending on a local solid fraction C . This phase function is obtained by projecting the shape of the particles on the Eulerian fixed mesh. The advection equation on C is not reported in the one-fluid model as only fixed particles are considered in the present work.

6.2.2 Fictitious domain approach and viscous penalty method

In the present work, fixed staggered Cartesian grids are used to discretized both fluid and solid media. The particles are viewed as fictitious domains sliding with their own Lagrangian surface mesh onto the fixed mesh used to solve the conservation equations (6.1-6.3). The details of the viscous penalty method and fictitious domain approach considered here are provided in [24, 87, 109].

In a first approach, only motionless particles are considered in this work. On a numerical point of view, they are fixed by imposing the velocity of the Eulerian cells near their centroids to zero, and the viscous penalty method propagates the zero velocity in the whole solid medium. The particle temperatures will be considered constant over time, they are imposed at a fixed value in the whole solid medium also thanks to a penalty method used in the energy equation (6.3) [63].

6.2.3 Drag force and heat flux computation using Aslam extension

As mentioned in the introduction, the aim of this work is to propose an original method to compute the hydrodynamic force \mathbf{F} and the heat flux Q_p of a particulate

flow from the velocity, pressure and temperature fields extracted from PR-DNS simulations. They are given by:

$$\mathbf{F} = \oint_S \bar{\boldsymbol{\sigma}} \cdot \mathbf{n} \, dS \quad \text{and} \quad Q_p = \oint_S -K_f \nabla T \cdot \mathbf{n} \, dS$$

The computation of \mathbf{F} and Q_p consists in discretizing the particle surface S on a set of N elements called Lagrangian mesh (see figure 6.1), such that:

$$\mathbf{F} \approx \sum_l^N \bar{\boldsymbol{\sigma}}_l \cdot \mathbf{n}_l \, \Delta S_l \quad \text{and} \quad Q_p \approx \sum_l^N -k_f (\nabla T)_l \cdot \mathbf{n}_l \, \Delta S_l \quad (6.4)$$

where k_f is the thermal conductivity, $\bar{\boldsymbol{\sigma}}_l$ and $(\nabla T)_l$ are the fluid stress tensor and the temperature gradient located at the l^{th} element center C_l , \mathbf{n}_l is the ongoing normal to the l^{th} element and ΔS_l its area.

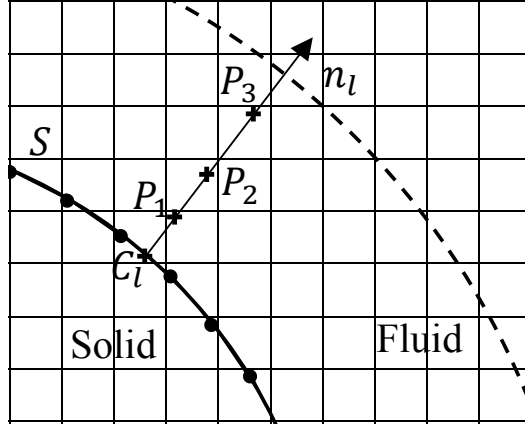


Figure 6.1: Details of a 2D discretization of the particle surface S and extrapolation points P_i of the third order Lagrange method used in drag force and heat flux computation.

When \mathbf{n}_l and ΔS_l are easily deduced from the nodes coordinates of the l^{th} element, getting the stress tensor $\bar{\boldsymbol{\sigma}}_l$ and the temperature gradient $(\nabla T)_l$ at the l^{th} element center C_l is not straightforward when viscous penalty method is used to simulate fluid-solid flows. Indeed, velocity, pressure and temperature values, solution of Eqs (6.1-6.3), are inaccurate in the Eulerian cells cut by the interface [23, 24]. To address this numerical issue, a Lagrange extrapolation coupled to a Taylor interpolation of third order was proposed to extrapolate the stress tensor [24] and the temperature gradient [23] from the fluid area far from the interface to the Lagrangian mesh (see figure 6.1). This approach was fully detailed and validated in [23, 24]. These validations showed the efficiency of the method in the computation of the drag force and heat flux. Indeed the drag coefficient and the Nusselt number, both given bellow, were found in good agreement with many reference results of the literature.

The force and heat transfer coefficients at the particle surface are defined as follows:

- Drag coefficient:

$$C_d = \frac{|\mathbf{F}|}{\frac{1}{2}\rho\tilde{U}^2A_p} \quad (6.5)$$

where $\tilde{U} = |U_\infty \mathbf{e}_x - \mathbf{U}_p|$ is the relative velocity between the particle and the fluid velocity at infinity, $U_\infty \mathbf{e}_x$ is the fluid velocity in the mean flow direction far from the particle, \mathbf{U}_p is the particle velocity, ν is the fluid kinematic viscosity and $A_p = \frac{\pi}{4}d^2$ the cross-sectional area of the particle.

- Nusselt number:

$$Nu = \frac{Q_p d}{k_f (T_s - T_f) S_p} \quad (6.6)$$

where Q_p is the heat flux, k_f the thermal conductivity and $S_p = \pi d^2$ the area of the sphere. The temperatures of the particle and the fluid are respectively T_s and T_f .

By using the Lagrange extrapolation coupled to the Taylor interpolation of 3rd order, some oscillations were observed in the distribution of both the pressure coefficient given in the spherical system (see the figure 6.2) by:

$$C_p(\theta) = \frac{p(\theta)}{\frac{1}{2}\rho U_\infty^2} \quad (6.7)$$

and the local Nusselt number

$$Nu_{loc}(\theta) = \frac{-\nabla T \cdot \mathbf{n} d}{(T_s - T_f)} \quad (6.8)$$

especially at low Reynolds number [23, 24]. These oscillations could be an explanation of some differences observed between our results and literature references, even if these oscillations were observed only for a few cases among the multitude conducted in [23, 24].

Another way to extrapolate the velocity, pressure and temperature from the fluid area, where they are not contaminated by the viscous penalty, to the region containing the interface, is proposed here to improve the accuracy of the current hydrodynamic force and the heat flux computations results. It is based on Aslam extensions [9].

Description of Aslam extension

Lets consider a sphere of diameter d circumscribed by a surface S , and a domain Ω divided in three sub-domains as illustrated in Fig. 6.3:

- Ω_1 the area inside the sphere of radius $(\frac{d}{2} - \Delta x)$, where Δx is the Eulerian cell mesh size.

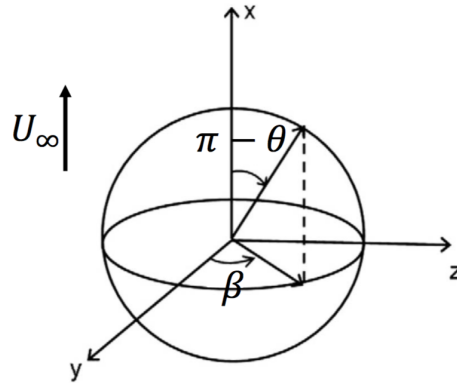


Figure 6.2: Spherical coordinate system around a particle. The flow direction is represented by the undisturbed velocity U_∞ .

- Ω_2 the area outside the sphere of radius $(\frac{d}{2} + \delta)$. This is the region where the velocity, pressure and temperature are not contaminated by the viscous penalty. δ is then the distance between Ω_2 and the interface.
- a band \mathcal{B} bounded by the surfaces of the two sphere of radius $(\frac{d}{2} - \Delta x)$ and $(\frac{d}{2} + \delta)$ respectively. It contains the interface S . It is represented as the grey area in Fig. 6.3.

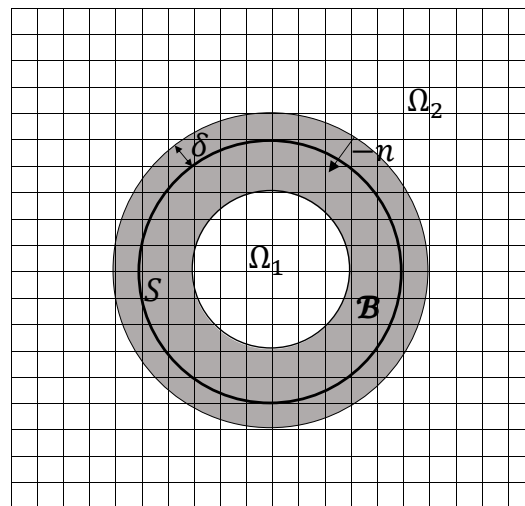


Figure 6.3: Details of the domain subdivision for Aslam extension [9]

Consider also a function g defined in Ω_2 . For example, g is a velocity component or the pressure used to compute the hydrodynamic force or either the temperature

utilized to estimate the heat flux coefficient at the particle surface. Applied to these quantities, the Aslam extension [9] consists then in extrapolating g from Ω_2 to \mathcal{B} by solving a series of advection equations given by (6.9).

Assuming a signed distance level set function ψ is available on \mathcal{B} ($\psi > 0$ inside the particle), a normal field to S inside the band can be defined as:

$$\mathbf{n} = \frac{\nabla\psi}{\|\nabla\psi\|}$$

In our approach and for a particle of any form, ψ is computed by a Ray-casting Method [94] based on the use of the Lagrangian mesh describing the particle surface S . However, for a spherical particle of diameter d and centred in \mathbf{x}_0 , \mathbf{n} and ψ are given by:

$$\forall \mathbf{x} \in \mathcal{B} \quad \mathbf{n} = \frac{\mathbf{x} - \mathbf{x}_0}{\|\mathbf{x} - \mathbf{x}_0\|} \quad \psi = \frac{d}{2} - \|\mathbf{x} - \mathbf{x}_0\|$$

To perform a m^{th} order Aslam extrapolation, the equations (6.9) are successively resolved for decreasing values of $k = m, m-1, \dots, 1$:

$$\frac{\partial g_k}{\partial \sigma} + H \nabla g_k \cdot (-\mathbf{n}) = g_{k+1} \quad (6.9)$$

where σ is a fictitious time, H is a Heaviside function defined by:

$$H(\mathbf{x}) = \begin{cases} 1 & \text{if } \mathbf{x} \in \mathcal{B} \\ 0 & \text{otherwise} \end{cases}$$

and g_k is the projection on the normal field of the k^{th} order differential of the function g :

$$\begin{aligned} g_1 &= g \\ g_2 &= \nabla g_1 \cdot (-\mathbf{n}) \\ g_3 &= \nabla g_2 \cdot (-\mathbf{n}) \\ &\vdots \\ g_m &= \nabla g_{m-1} \cdot (-\mathbf{n}) \\ g_{m+1} &= 0 \end{aligned}$$

these derivatives are computed in Ω_2 using a second-order upwind finite difference scheme:

$$(g_k)_i = \frac{3(g_{k-1})_i - 4(g_{k-1})_{i-1} + (g_{k-1})_{i-2}}{2\text{sgn}(\mathbf{n}_i)\Delta\mathbf{x}_i} \mathbf{n}_i \quad (6.10)$$

Using an upwind scheme rather than a Central finite difference scheme as proposed in Aslam [9] allows the use of the same Heaviside function H for all m equations (6.9) resolved for the m^{th} order Aslam extension, and not a specific Heaviside function H_k for each equation as proposed by Aslam [9].

The equations (6.9) are resolved until steady state is reached, using a first-order upwind finite difference scheme for the time derivative and a second-order TVD

"SuperBee" scheme [100] for the space derivative. It is worth noting that when the steady state is reached in the \mathcal{B} band, g verifies in \mathcal{B} :

$$\begin{aligned} \nabla g_m \cdot (-\mathbf{n}) &= 0 \\ \nabla g_{m-1} \cdot (-\mathbf{n}) &= g_m \\ &\vdots \\ \nabla g_2 \cdot (-\mathbf{n}) &= g_3 \\ \nabla g \cdot (-\mathbf{n}) &= g_2 \end{aligned}$$

Once the velocity and pressure fields for hydrodynamic force computation and temperature for heat flux computation, are extrapolated in the band \mathcal{B} using the m^{th} order Aslam extension, the stress tensor and the temperature gradient are computed in \mathcal{B} and then interpolated onto the Lagrangian mesh using a m^{th} order Taylor interpolation which was fully detailed in [24]. This interpolation is formulated as:

$$g(\mathbf{C}_l) = \sum_{|\alpha|=0}^{m-1} \frac{1}{\alpha!} \frac{\partial^\alpha g}{\partial x^\alpha}(\mathbf{E})(\mathbf{C}_l - \mathbf{E})^\alpha + O(\|\mathbf{C}_l - \mathbf{E}\|^m)$$

where $\alpha = (\alpha_1, \alpha_2, \alpha_3) \in \mathbb{N}^3$ is the sum multi-index and \mathbf{E} denotes the nearest Eulerian point to the point \mathbf{C}_l , as illustrated in Fig. 6.4 for a third order Taylor interpolation.

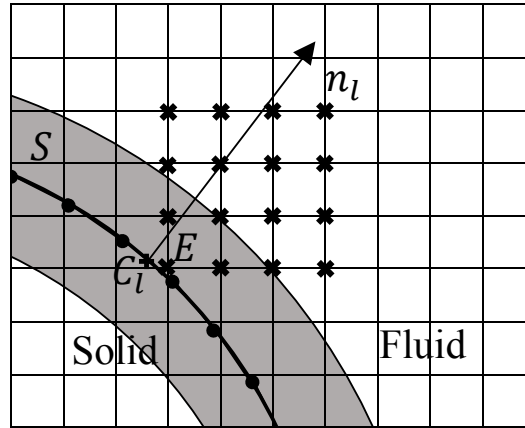


Figure 6.4: Details of Taylor interpolation points for drag force/heat flux computation at point \mathbf{C}_l of the surface Lagrangian mesh. \mathbf{E} is the nearest fluid point to the particle/fluid interface. The crosses represent the discrete compact support of the fluid points required for a 3^{rd} order Taylor interpolation.

Validation of Aslam extension

To validate these extension we used the same example as Aslam [9] *i.e.* a $[-\pi, \pi]^2$ 2D domain with a particle located at the center of the domain and a function g to

be extrapolated given by:

$$g(\mathbf{x}) = \begin{cases} \cos(\mathbf{x}_1) \sin(\mathbf{x}_2) & \text{if } \psi(\mathbf{x}) > 0 \quad (\text{i.e. inside the particle}) \\ 0 & \text{otherwise} \end{cases}$$

In this example the function g is defined inside the particle *i.e.* in Ω_1 . It has to be extrapolated in the band \mathcal{B} as illustrated in Figure 6.5.

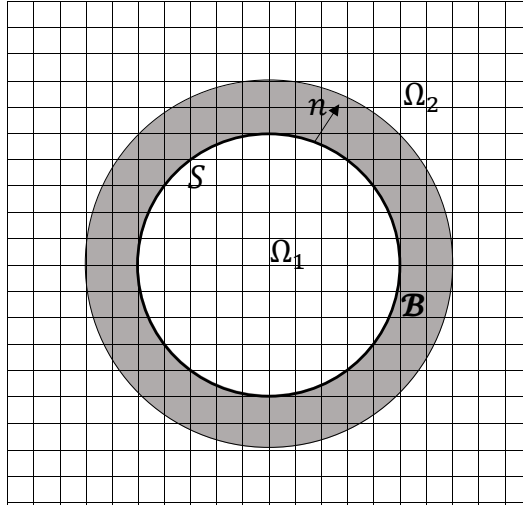


Figure 6.5: Details of the Aslam extension validation example.

This example was extended to non-spherical particles, with an ellipse and a square. Figure 6.6 shows the contours of g inside (a) a circle, (b) an ellipse and (c) a square which will be extrapolated in \mathcal{B} *i.e.* the delimited white zone outside the particle, using equations (6.9).

The function g is extrapolated using Aslam extension, *i.e.* resolving equations (6.9), for four different orders:

- Constant Aslam extension $m = 1$: it consists in resolving equation $\frac{\partial g}{\partial \sigma} + H \nabla g \cdot \mathbf{n} = 0$ in \mathcal{B} until g reaches a steady state *i.e.* $\frac{\partial g}{\partial \sigma} = 0$, *i.e.* $\frac{\partial g}{\partial \mathbf{n}} = \nabla g \cdot \mathbf{n} = 0$, which means that extrapolated g is constant on the normal direction to the particle surface in the extrapolation region \mathcal{B} as illustrated in Figure 6.7.
- Linear Aslam extension $m = 2$: it consists in extrapolating the first normal derivative $g_2 = \frac{\partial g}{\partial \mathbf{n}}$ from Ω_1 , where it is computed from g using (6.10), to the band \mathcal{B} using Constant Aslam extension. Then g is extrapolated from Ω_1 to \mathcal{B} by resolving equation $\frac{\partial g}{\partial \sigma} + H \nabla g \cdot \mathbf{n} = g_2$ until g reaches a steady state. An illustration of such function is given in Figure 6.8 where one can observe

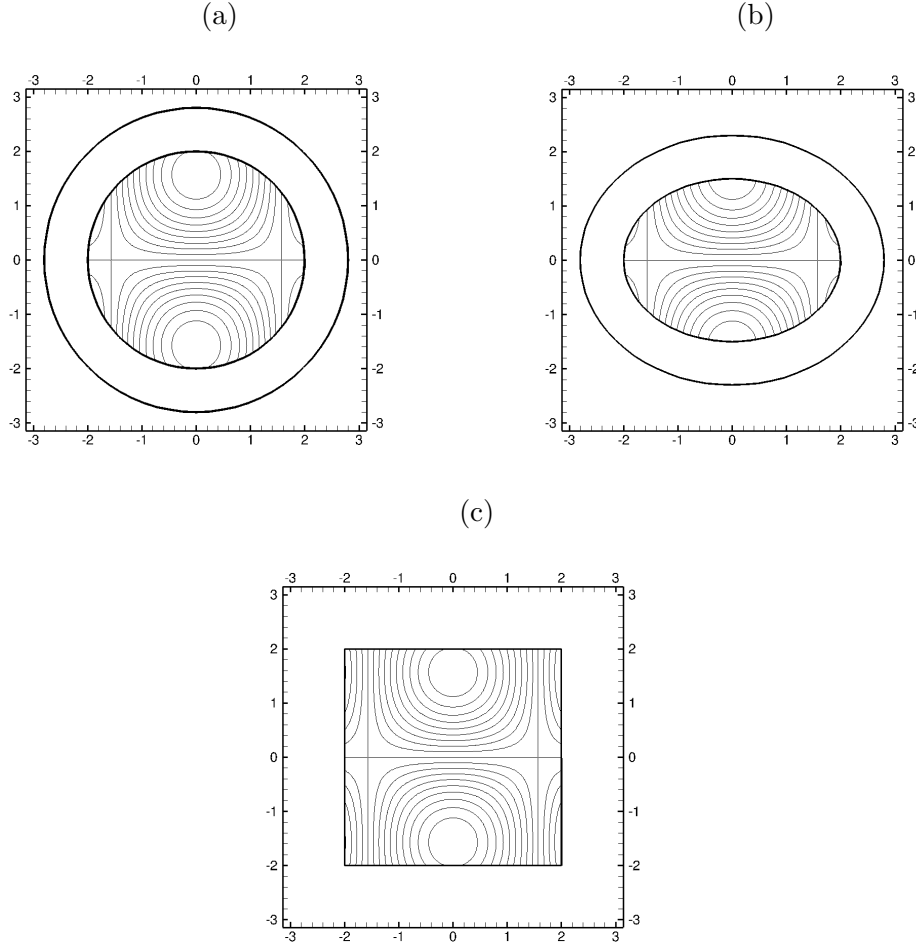


Figure 6.6: Contour (with a 0.2 increment) of the initials conditions of g for Aslam extension from: (a) a circle, (b) an ellipse and (c) a square.

that g is no more constant on the normal direction to the particle surface in \mathcal{B} ($\nabla g \cdot \mathbf{n} = g_2$).

- Quadratic Aslam extension $m = 3$: it consists in extrapolating the second normal derivative $g_3 = \frac{\partial g_2}{\partial \mathbf{n}} = \frac{\partial^2 g}{\partial \mathbf{n}^2}$ from Ω_1 , where it is computed from g_2 using (6.10), to the band \mathcal{B} using Constant Aslam extension. Then, g_2 is extrapolated using Linear Aslam extension with g_3 as second member of the extrapolation equation. And finally g is extrapolated by resolving in \mathcal{B} $\frac{\partial g}{\partial \sigma} + H \nabla g \cdot \mathbf{n} = g_2$ until g reaches a steady state. In Figure 6.9, the extrapolated part of g seems to converge toward the initial function g . Note that the incoherent values of the extrapolated g in the corner region for the square case are the consequence of the fact that the normal is unknown in this region.

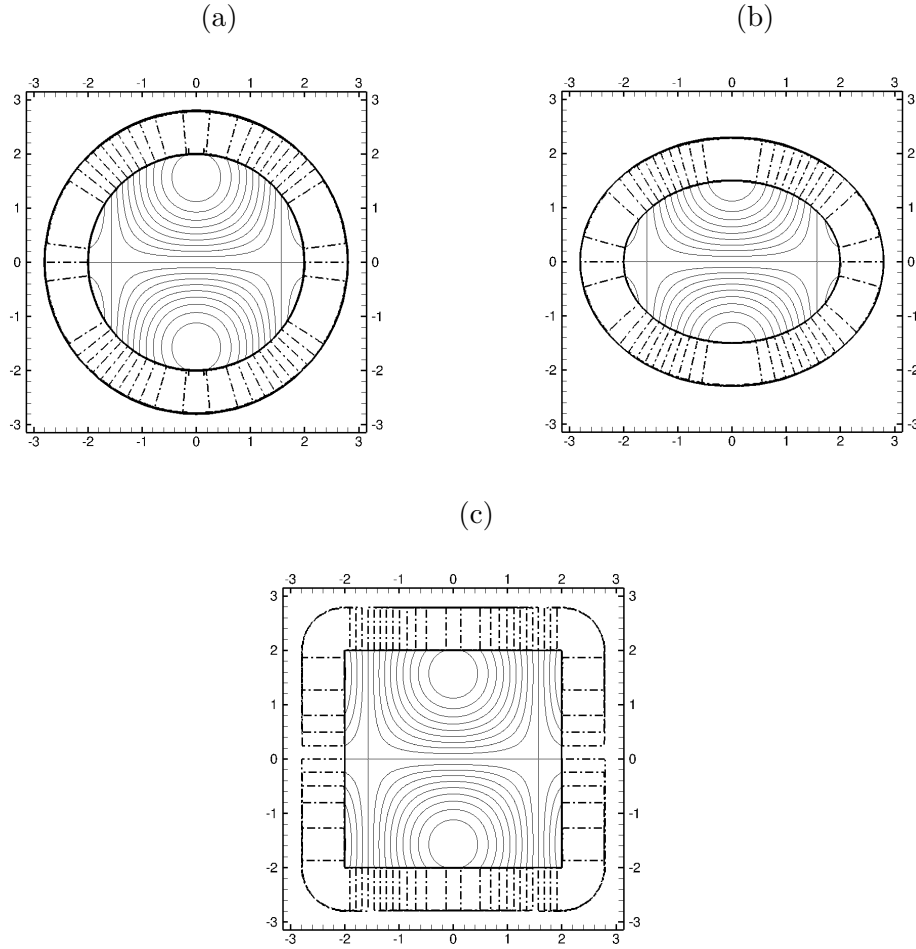


Figure 6.7: Contour (with a 0.2 increment) of the function g extrapolated using Constant Aslam extension ($m = 1$) from: (a) a circle, (b) an ellipse and (c) a square.

- Cubic Aslam extension $m = 4$: it consists in extrapolating the third normal derivative $g_4 = \frac{\partial g_3}{\partial \mathbf{n}}$ from Ω_1 , to the band \mathcal{B} using Constant Aslam extension. In a second step, g_3 is obtained using Linear Aslam extension with g_4 as second member of the extrapolation equation. Then g_2 is extrapolated using Quadratic Aslam extension with g_3 as second member of the extrapolation equation. Finally g is approximated by resolving $\frac{\partial g}{\partial \sigma} + H \nabla g \cdot \mathbf{n} = g_2$ until g reaches a steady state. The results obtained with this extrapolation are illustrated in Figure 6.10.

A convergence study was conducted for these four Aslam extension orders using

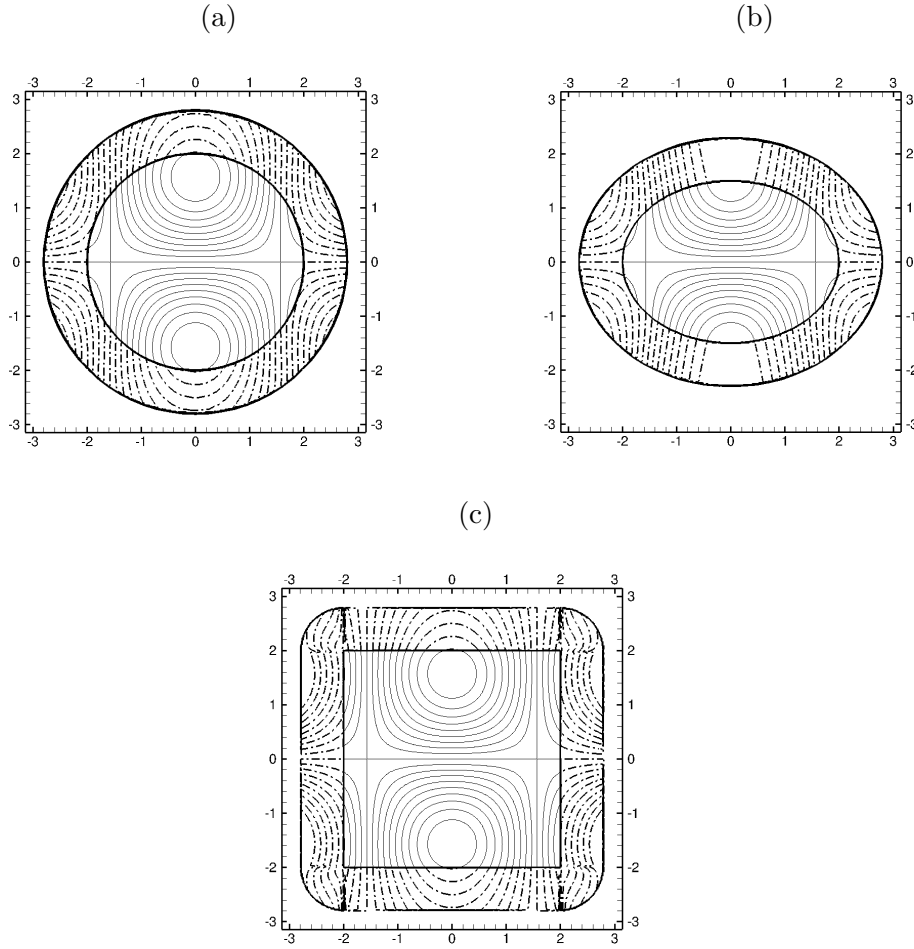


Figure 6.8: Contour (with a 0.2 increment) of the function g extrapolated using Linear Aslam extension ($m = 2$) from: (a) a circle, (b) an ellipse and (c) a square.

the relative error, in the band \mathcal{B} , between exact g values and those obtained with extrapolation Aslam procedures. It can be observed in Figure 6.11 that these errors are always small (from 0.1 to 10^{-8} %), and that the expected orders are found for extensions of the circle and the ellipse shape. However, in the case of an extension from a square surface, the order could not be reached because of the inaccurate values in the region near the square corner, where the normal to the surface is not defined.

The exact same study was conducted for three dimensional cases. Indeed, a $[-\pi, \pi]^3$ 3D domain with a particle (sphere, ellipsoid, cube) located at the center of the domain and a function g to be extrapolated are considered here to validate Aslam extension in 3D. Now, the function g is defined by:

$$g(\mathbf{x}) = \begin{cases} \cos(\mathbf{x}_1) \sin(\mathbf{x}_2) \cos(\mathbf{x}_3) & \text{if } \psi(\mathbf{x}) > 0 \text{ (i.e. inside the particle)} \\ 0 & \text{otherwise} \end{cases}$$

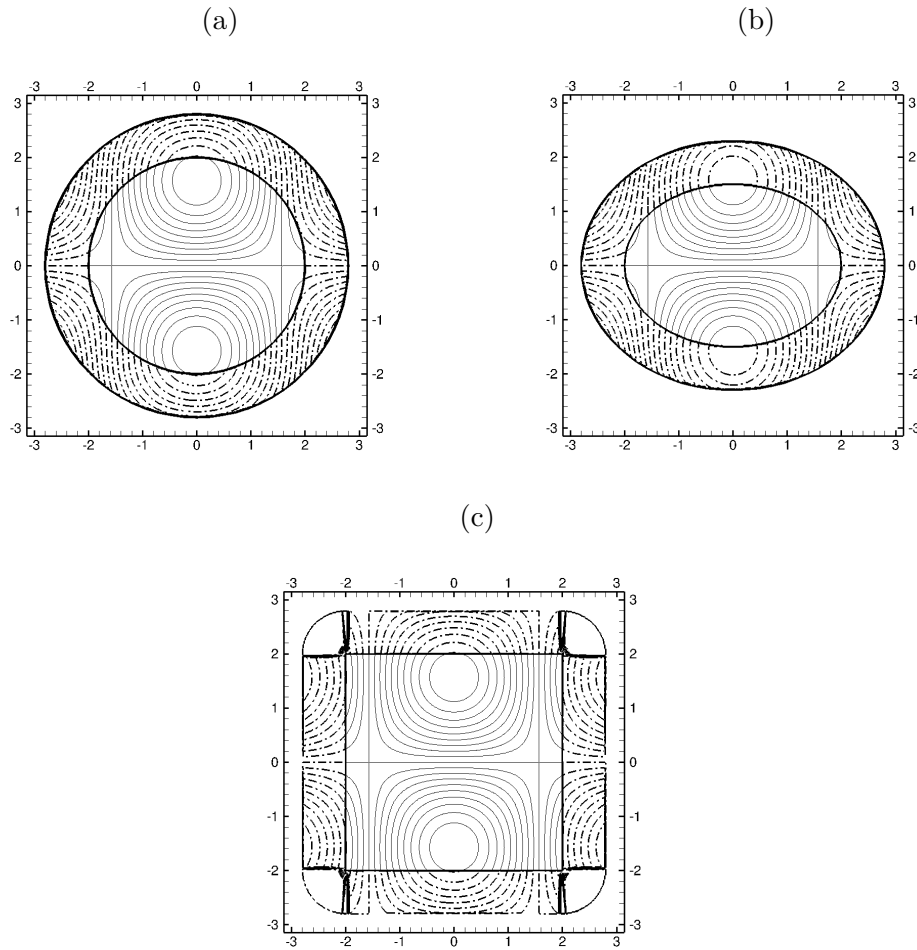


Figure 6.9: Contour (with a 0.2 increment) of the function g extrapolated using Quadratic Aslam extension ($m = 3$) from: (a) a circle, (b) an ellipse and (c) a square.

Figure 6.12 shows that, similarly as in the 2D cases, the expected extension orders are found for the sphere and the ellipsoid, even if the relative errors are two orders of magnitude greater than in 2D cases. As for the 2D case, the non-definition of the normal to the cube in the vicinity of its corners lead to inaccurate values of the extrapolated function in the region near to these corners. This explains the errors behavior that makes the extension order computation impossible in this case.

6.3 Isolated stationary sphere past by a uniform flow

The aim of this work is to assess how Aslam extension could improve the computation of the hydrodynamic force and the heat flux compared to the results obtained using Lagrange extrapolation. To do that, we conducted the same simulations

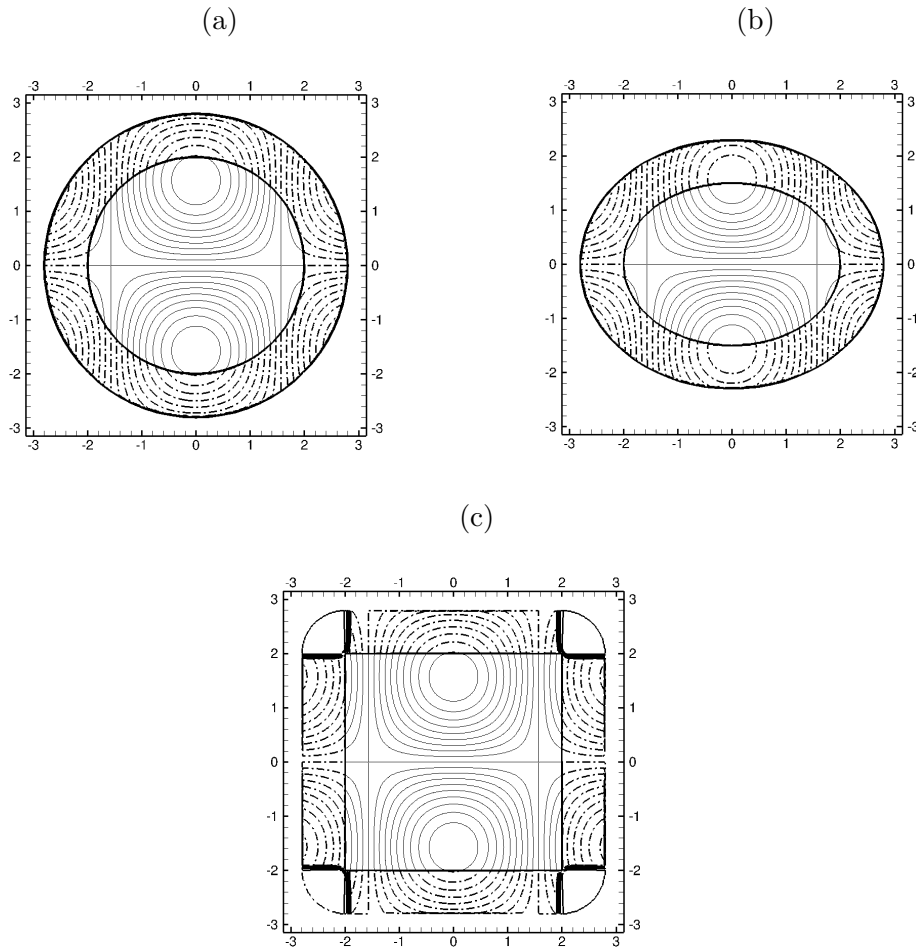


Figure 6.10: Contour (with a 0.2 increment) of the function g extrapolated using Cubic Aslam extension ($m = 4$) from: (a) a circle, (b) an ellipse and (c) a square.

carried out in [23, 24] to validate the force and heat transfer computation using Lagrange extrapolation. The first case considered here is a forced convection by uniform flow past a hot stationary sphere, illustrated in figure 6.13. All the details and description of this problem are reported in [23, 24].

6.3.1 Drag force computation

Following the steps of the study of the drag force computation using Lagrange extrapolation [24], we will first determine how far we have to go from the particle to reach uncontaminated velocity and pressure of the fluid to extrapolate them to the interface in order to get accurate values of drag force. The effect of Aslam extrapolation order will be studied at the same time on these values. Moreover, some perturbations were observed in the local pressure distribution on the particle surface

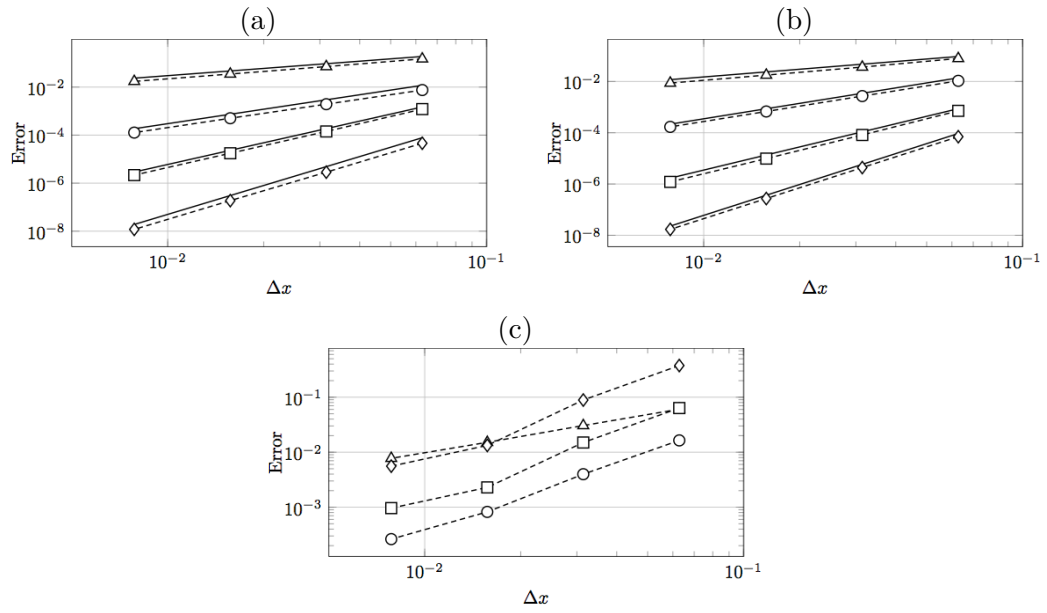


Figure 6.11: Convergence orders in 2 dimensions for Aslam extension from: (a) a circle, (b) an ellipse and (c) a square. (Δ) $m = 1$, (\circ) $m = 2$, (\square) $m = 3$ and (\diamond) $m = 4$.

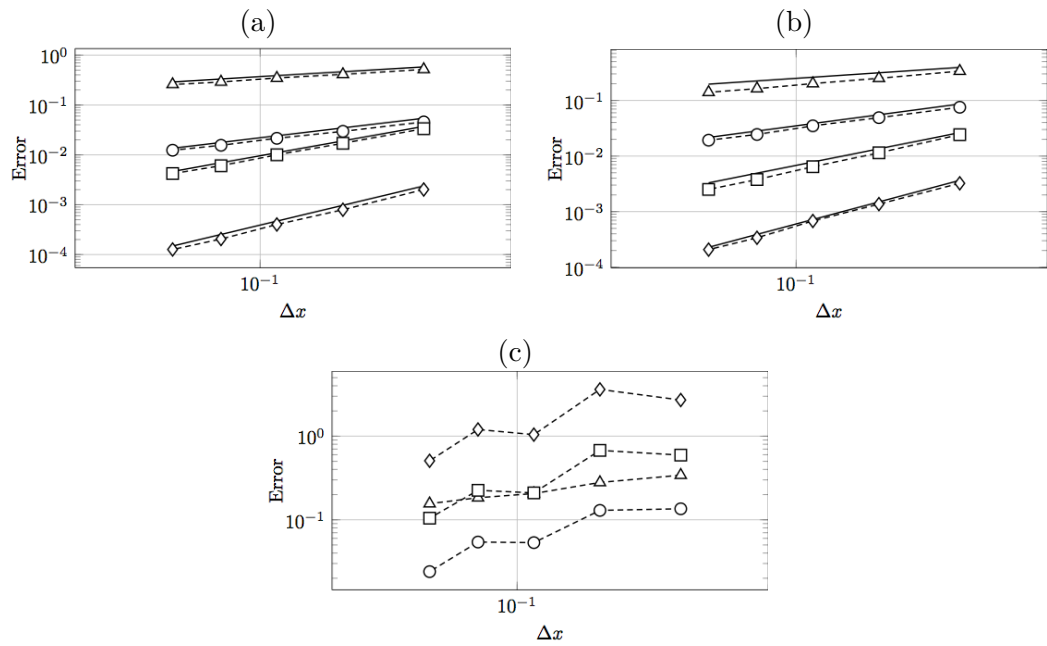


Figure 6.12: Convergence orders in 3 dimensions for Aslam extension from: (a) a sphere, (b) an ellipsoid and (c) a cube. (Δ) $m = 1$, (\circ) $m = 2$, (\square) $m = 3$ and (\diamond) $m = 4$.

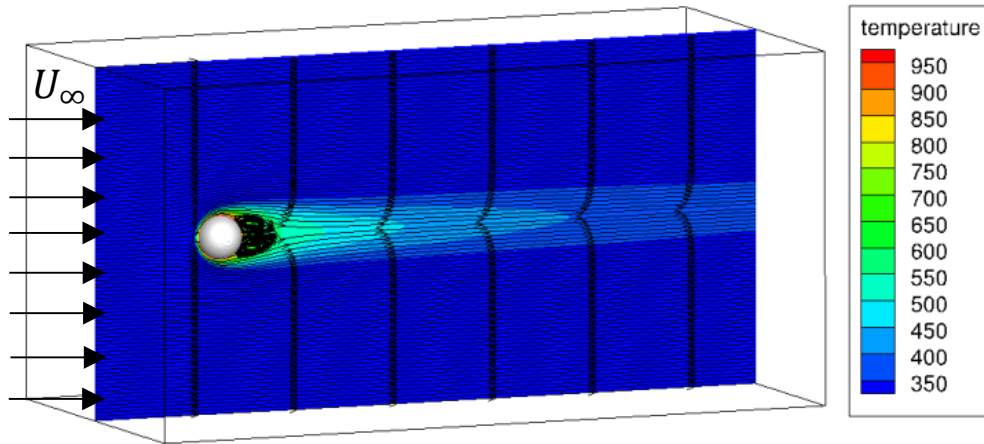


Figure 6.13: Streamlines and temperature field for a uniform flow past a sphere at $Re = 100$.

in [24]. We will see how Aslam extension could prevent these oscillations. Finally, we will compare the drag coefficient values computed with Lagrange extrapolation [24] with those computed with Aslam extension.

Effect of the extrapolation distance δ

One of the main drag force computation parameter using Lagrange extrapolation, studied in [24], was the distance (δ) between the particle and the first point of extrapolation \mathbf{P}_1 (see Figure 6.1). Indeed, as reported in [24] and as illustrated in Figures (6.14 a) at Stokes regime and (6.14 c) at $Re = 100$, the drag force values, computed using Lagrange extrapolation, are inaccurate for $\delta \leq 1$. This is due to contaminated values of velocity and pressure induced by the viscous penalty method [26] in the Eulerian cells cut by the interface. The study of the effect of this distance δ (illustrated in Figure 6.3) is conducted for drag force computation using Aslam extension as well. The Figures (6.14 b) (6.14 d) show that, in order to get an accurate drag force using Aslam extensions, a third order is required. Therefore, for the rest of this work, a third order Aslam extension coupled with a third order Taylor interpolation will be used in the drag force computation. One can also observe in these figures that the distance to go far from the interface is reduced to $\delta = 0.5$ with Aslam approach. One possible explanation of this improvement is that, it is actually the pressure and the velocity that are extrapolated by Aslam extension in the drag force computation rather than the stress tensor components, *i.e.* the gradients of these variables, as it is the case when the Lagrange extrapolation is used. Indeed, the stress tensor is computed using centered difference schemes which utilizes contaminated values of velocity and pressure for $\delta \leq 1$ (and even solid values for $\delta = 0$). On the other hand, extrapolating directly the velocity components and the pressure using Aslam extension and then computing the stress tensor from these extrapolated values reduces the distance to which how far we have to move

away from the particle to reach accurate drag force values.

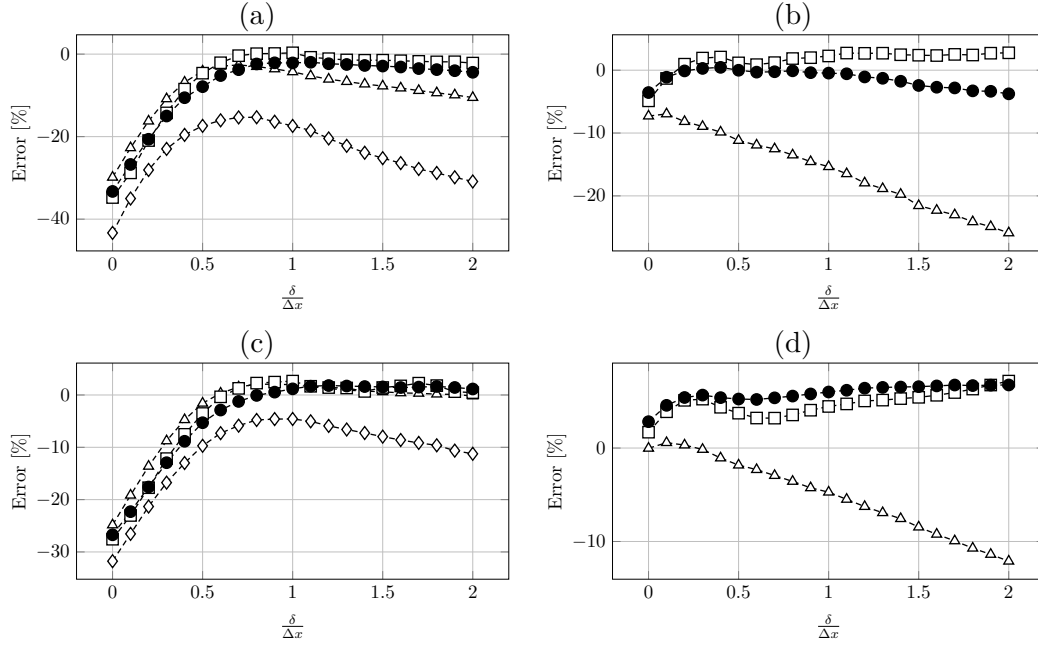


Figure 6.14: Drag force relative error (%) for the uniform flow past a sphere in Stokes regime (a) for Lagrange extrapolation and (b) for Aslam extrapolation and at $Re = 100$ for (c) Lagrange extrapolation and (d) Aslam extrapolation. Different extrapolation orders are considered: (\diamond) first, (\triangle) second, (\bullet) third, and (\square) fourth order. The distance between the first Eulerian point used to extrapolate forces and the particle surface is δ .

Pressure coefficient

The analysis of local pressure profiles in [24] was used to better understand the behavior of the pressure on the sphere depending on the Reynolds number. The local pressure coefficients are defined by equation (6.7) in a spherical coordinate system (see figure 6.2).

The pressure coefficient distribution according to θ was compared in [24] to some available body fitted simulations results conducted by Magnaudet *et al.* [68], Dennis and Walker [38], LeClair *et al.* [30] and Massol [70] at different Reynolds numbers. The results are presented in Figures (6.15 a), (6.15 c) and (6.15 e) for $Re = 1, 10, 100$ respectively.

It is well-known that, for this range of Reynolds number, the flow is symmetric with respect to its direction, as illustrated in Figure 6.16. Therefore, the pressure coefficient distribution must be the same for all the polar angle (β) plans, translating by that the flow symmetry. This expected behavior was mostly observed when

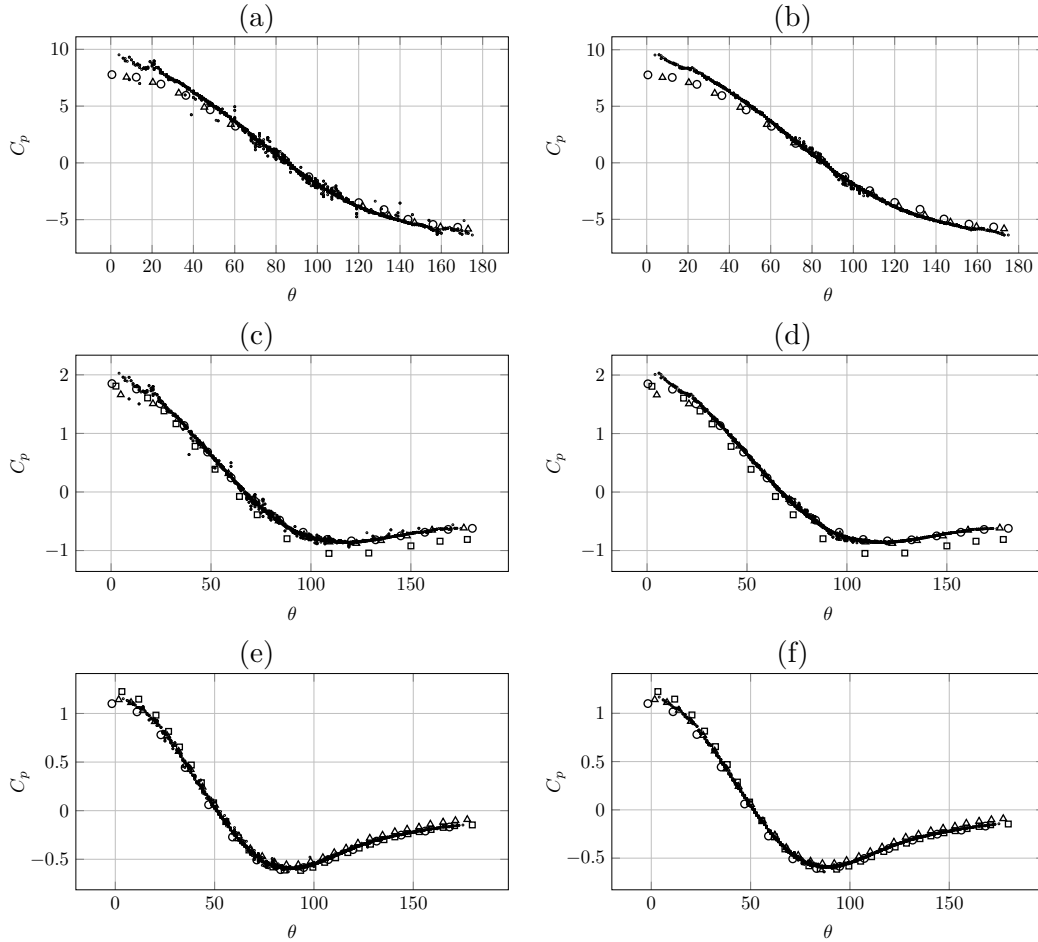


Figure 6.15: Pressure coefficient for a uniform flow past an isolated sphere at $Re = 1$: (a) for Lagrange extrapolation, (b) for Aslam extrapolation, $Re = 10$: (c) for Lagrange extrapolation, (d) for Aslam extrapolation, $Re = 100$: (e) for Lagrange extrapolation, (f) for Aslam extrapolation. (\diamond) Dennis *et al.* [38], (Δ) Magnaudet *et al.* [68], (\circ) LeClair *et al.* [30], (\square) Massol [70], and (\cdot) present work.

Lagrange extrapolation was used in the drag force computation [24] (see Figures (6.15 a), (6.15 c), (6.15 e)). However, some local pressure values diverge from the expected ones, especially for low Reynolds number ($Re = 1, 10$) as illustrated in Figures (6.15 a), (6.15 c).

The use of Aslam extension in the drag force computation seems to reduce the pressure oscillations, which is a good point of the method, although only few pressure points exhibited values far from expected ones when Lagrange extrapolation is used. Indeed, the same distribution of the pressure coefficient is observed for all β plans in Figures (6.15 b), (6.15 d), (6.15 f).

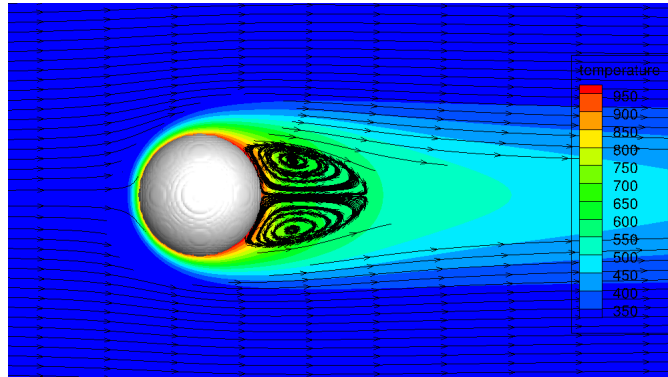


Figure 6.16: Streamlines and temperature field for a uniform flow past a sphere at $Re = 100$.

Drag coefficient

The last step in the study of drag force computation, using a third order Aslam extension, is devoted to the drag coefficient, given by the Eq(6.5) and extracted from PR-DNS. It is compared to Schiller and Naumann [97] correlation for a wide range of Reynolds number ($Re = 0.1 - 290$). This comparison was conducted in [24] when the drag force was computed using Lagrange extrapolation.

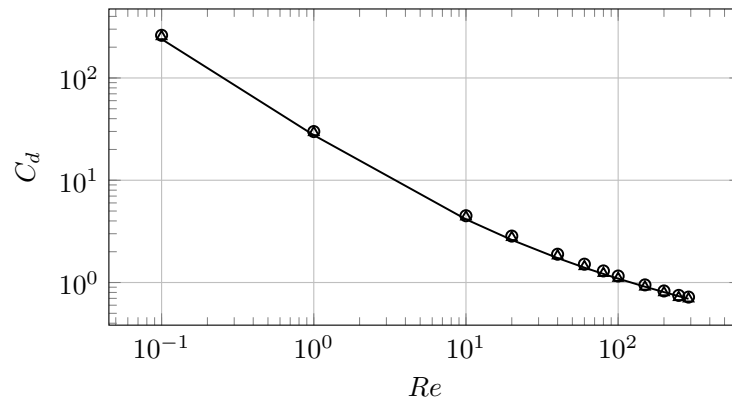


Figure 6.17: Drag coefficient for uniform flow past sphere at different Reynolds number: (—) Schiller and Naumann [97], (○) present work using Aslam extension and (△) using Lagrange extrapolation.

Figure 6.17 shows the good agreement of our results with Schiller and Naumann [97]. It also shows that, at least for this particular case, the drag force computed using Aslam extension is quite the same than the one computed using Lagrange extrapolation. Indeed, as it has been discussed earlier, Aslam extension improvement was the reduction of the distance δ to go away from the particle to get accurate drag force, and the correction of the few inaccurate values of the pressure on the particle surface. In the case of an isolated sphere the distance δ does not affect

the outcome of the drag force as soon as the accurate value is found whatever the force calculation method used (Lagrange extrapolation or Aslam extension). On the contrary, in the case of arrangement of spheres which will be discussed in the section 6.4, the distance δ will be an important parameter especially for high solid volume fraction. Moreover, the number of inaccurate pressure values in the pressure coefficient distribution is not important enough to really influence the total drag force in the present case of an isolated sphere.

6.3.2 Heat transfer computation

The effect of choosing δ is now considered with respect to the heat transfer computation. This effect is estimated using the local Nusselt number computed using a third order Aslam extension [9] coupled to a third order Taylor interpolation, followed by a comparison of this local Nusselt number distribution to the one computed using Lagrange extrapolation [23]. Once the parameter δ is set, the global Nusselt number for the problem of a uniform flow past a hot sphere is compared to the correlations given by Ranz and Marshall [88], Feng and Michaelides [43] and Whitaker [115].

Effect of the extrapolation distance δ

To study the δ effect, the local Nusselt number distribution was compared to the one provided by Massol [70] thanks to body-fitted PR-DNS results at $Re = 100$. As previously explained for the pressure coefficients, this distribution is also expected to be symmetric with respect to the flow direction, as illustrated in Figure 6.16.

The local Nusselt number computed for $\delta = 0$ does not reflect the flow symmetry neither for the one computed using Lagrange extrapolation (see Figure 6.18 a) nor the one computed using Aslam extension (see Figure 6.18 b), even if the latest improved sensibly the result with lower amplitude of Nusselt oscillations. Indeed, the error between our result (Nu_{loc}) and Massol's ($Nu_{locMassol}$) given by $\frac{\sum_{i=1}^N |(Nu_{loc})_i - (Nu_{locMassol})_i|}{\sum_{i=1}^N |(Nu_{locMassol})_i|}$ (illustrated in Figure 6.19) is about 25% for Lagrange extrapolation and less than 15% for the Aslam extension. This error decreases as the distance δ increases until being lower than 10% for $\delta \geq 1$ in case of Lagrange extrapolation use, and about 5% in the case of Aslam extension use for $\delta = 1$ as illustrated in Figure 6.19. Moreover, Figures (6.18 c) and (6.18 d) show the distribution of the local Nusselt number for $\delta = 1$ with respectively Lagrange and Aslam extrapolations and they show also that Aslam extension improves the Heat transfer computation with an almost symmetrical distribution of the local Nusselt number for $\delta = 1$. Therefore, the extrapolation distance will always be $\delta = 1$ in the rest of the present work.

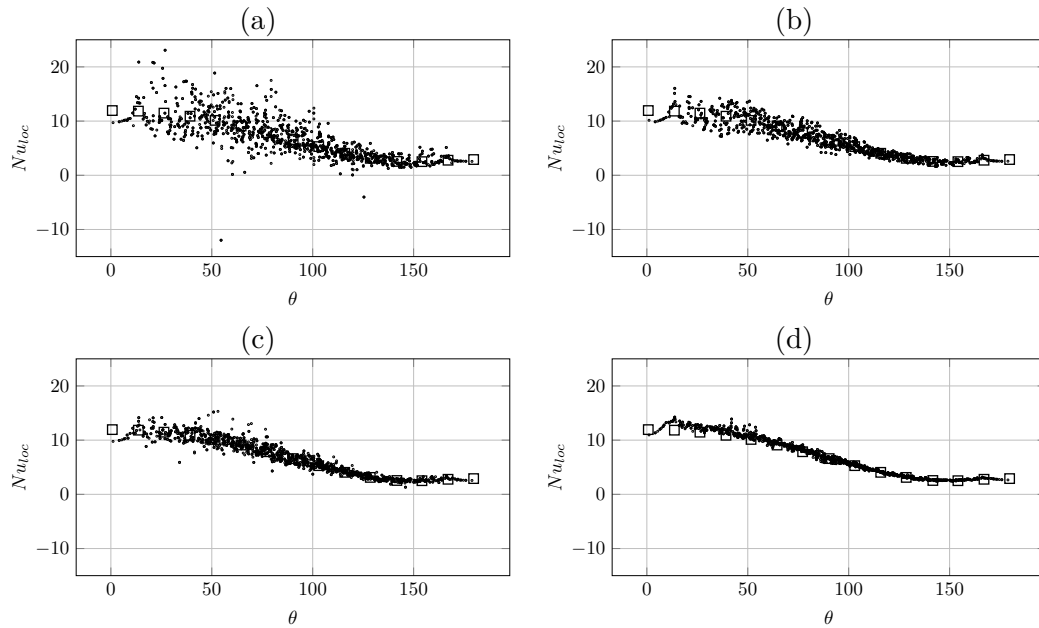


Figure 6.18: Local Nusselt coefficient for a uniform flow past an isolated sphere at $Re = 100$, as function of the azimuthal angle θ at $\delta = 0$: (a) for Lagrange extrapolation, (b) for Aslam extrapolation, $\delta = 1$: (c) for Lagrange extrapolation, (d) for Aslam extrapolation. (.) present work, (\square) Massol [70].

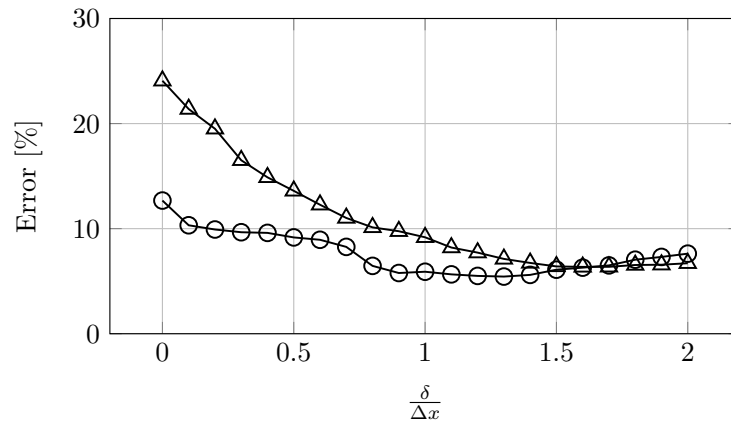


Figure 6.19: Local Nusselt number relative error compared to Massol's result [70] as a function of the extrapolation distance δ : (\circ) using Aslam extension and (Δ) using Lagrange extrapolation.

Nusselt number

After setting up the numerical parameter for the heat transfer computation, the Nusselt number obtained when considering a uniform flow past a hot fixed sphere is computed using Aslam extension and compared to the values computed using Lagrange extrapolation [23] and to some of the existing correlations of the literature.

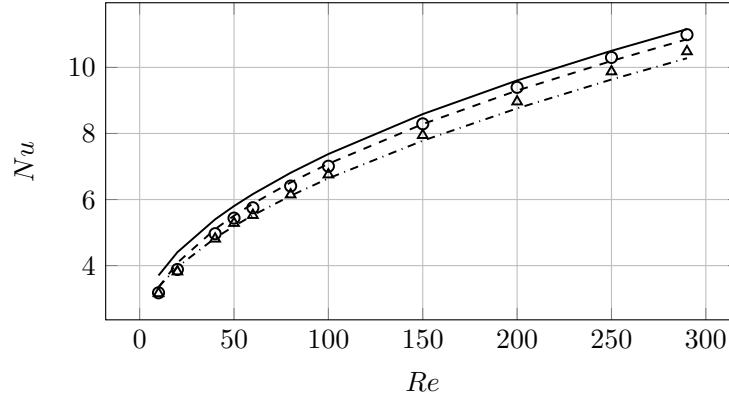


Figure 6.20: Nusselt coefficient for the uniform flow past a hot sphere at various Reynolds numbers: (—) Ranz and Marshall [88], (---) Feng and Michaelides [43], (-.-) Whitaker *et al.* [115], (\circ) present work using Aslam extension and (\triangle) using Lagrange extrapolation.

Figure 6.20 shows the good agreement of our results to correlations, with clear improvement when Aslam extension is used to compute the Nusselt number. Indeed, unlike the drag force computation and as it was discussed in the previous subsection 6.3.1, the Aslam extension has an effect on the obtained local Nusselt number values. This naturally improves the global Nusselt number that converges toward the well-known Ranz and Marshall correlation [88] (see Figure 6.20), which is expected to be the reference law used in the literature.

6.4 Face-Centered Cubic arrangement of stationary sphere past by a uniform flow

As explained in subsection 6.3.1, Aslam extension does not improve the drag force computation of an isolated sphere. Indeed, Aslam extension reduced the distance δ to go far from the particle to reach accurate drag value, going from $\delta = 1$ for Lagrange to $\delta = 0.5$ for Aslam. Moreover, for an isolated sphere, this distance does not affect the computed value of the drag as long as an accurate value is reached whatever the extrapolation technique used (see Figure 6.14). However, it is obvious that for an assembly of spheres, the distance δ would affect the drag force computed on each sphere as the distance between the spheres reduces when the solid volume fraction increases. Two configuration of sphere assemblies, mono- and bi-dispersed arrangements of spheres, are studied in this section following in that the work done in [23, 24] when Lagrange extrapolation was used in the drag force and heat transfer computation in order to compare the two extrapolation method outcomes.

6.4.1 Monodispersed Face-Centred Cubic periodic arrangement of spheres

The first case considered here is a uniform flow past a Face-Centered Cubic (FCC) array of spheres. We wish to study whether or not Aslam extension improves the drag force and the heat transfer computations, when a sphere is surrounded by other particles, in comparison to those computed using Lagrange extrapolation. FCC arrangement of spheres consists in a cube where three spheres are placed on the faces centers, and one sphere is located on the vertices with periodic boundary conditions, as illustrated in the figure 6.21. This case was fully detailed in [23, 24].

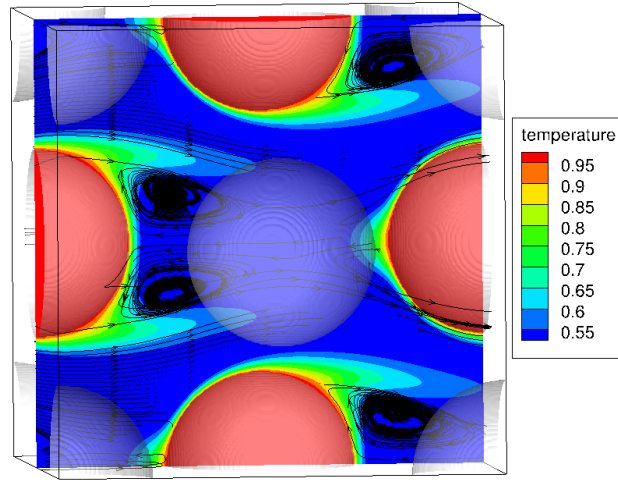


Figure 6.21: Streamlines and temperature field for a steady flow along the x-axis of a Face-Centered Cubic array of spheres at $Re = 300$, $\alpha_d = 0.15$

Drag force

When the flow steady state is reached at the desired Reynolds number, as explained in [24], the mean non-dimensional drag force F for all the particles is then deduced from the drag forces computed over each particle by:

$$F = \frac{|\langle \mathbf{F}^D \rangle|}{3\pi\mu d(1 - \alpha_d)|\langle \mathbf{u}_f \rangle|} \quad (6.11)$$

with $\langle \mathbf{F}^D \rangle = \frac{1}{N_p} \sum_i^{N_p} \mathbf{F}_i^D$, \mathbf{F}_i^D being the drag force computed over the i^{th} particle.

The non-dimensional drag force F normalized by the isolated sphere non-dimensional drag force (given by Schiller and Naumann [97]) $F_s = \frac{1 + 0.15Re^{0.687}}{(1 - \alpha_d)^2}$, noted as $\frac{F}{F_s}$, is compared to Massol's results [70] extracted from body-fitted simulations and

taken here as reference results, and to the drag force results computed using Lagrange extrapolation in order to assess the Aslam extension effect on the drag force computation.

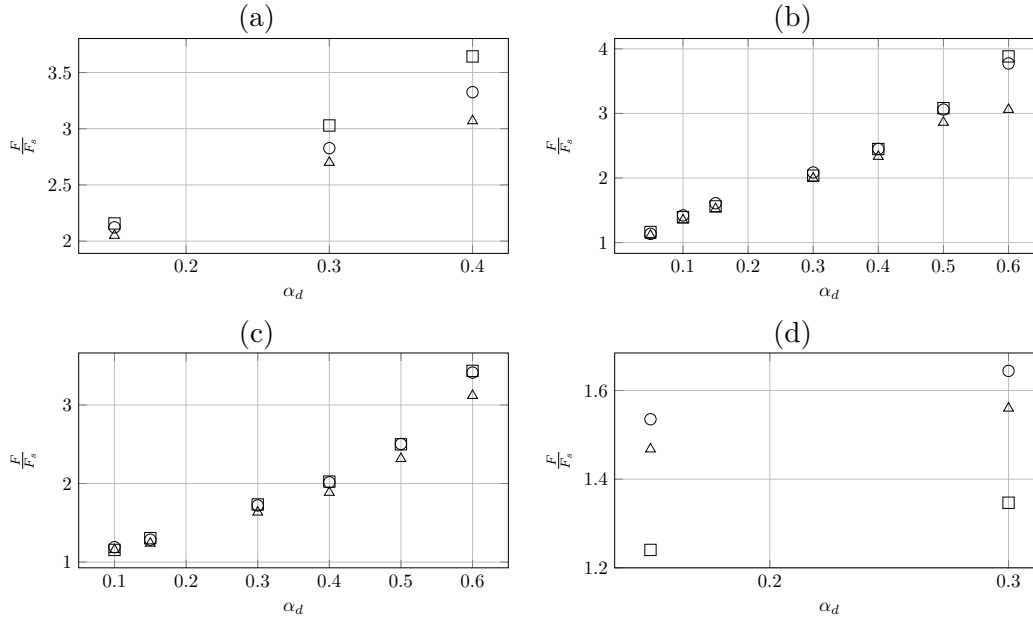


Figure 6.22: Drag force for a uniform flow past a FCC, normalized by Schiller and Naumann [97] drag force for a uniform flow past an isolated sphere. Results are presented as a function of the solid volume fraction α_d and Reynolds number (a) $Re = 10$, (b) $Re = 50$, (c) $Re = 100$, (d) $Re = 300$: (\square) Massol [70], (\circ) present work using Aslam extension and (\triangle) present work using Lagrange extrapolation.

Figure 6.22 shows the non-dimensional normalized drag force $\frac{F}{F_s}$ computed using Aslam extension, the one computed using Lagrange extrapolation and finally the Massol's results [70] used here as a reference to illustrate the possible improvement brought by the Aslam extension applied to the drag force computation. One can observe that for $Re = 10, 50, 100$ the drag force computed using Aslam extension converge toward the reference body fitted values provided by Massol [70]. Aslam simulations match Massol results better than the values computed using Lagrange extrapolation. This shows clearly the positive effect of the reduction, by Aslam extension, of the extrapolation distance δ on the drag force computation. It is worth noting that Massol simulations were under resolved for $Re = 300$ which could explain the discrepancies with our results.

Nusselt coefficient

Although Aslam extension improvement was observed for an isolated sphere on the Nusselt number results (unlike for the drag force), a study of its effect is conducted here for a FCC array of spheres in order to test its efficiency for the heat transfer

computation in an assembly of spheres. The global Nusselt coefficient for a uniform flow past a FCC array of spheres is deduced from the Nusselt computed on each sphere by:

$$\langle Nu \rangle = \frac{1}{4} \sum_i^{N_p} Nu_i \quad (6.12)$$

where Nu_i is the Nusselt number computed over the i^{th} particle.

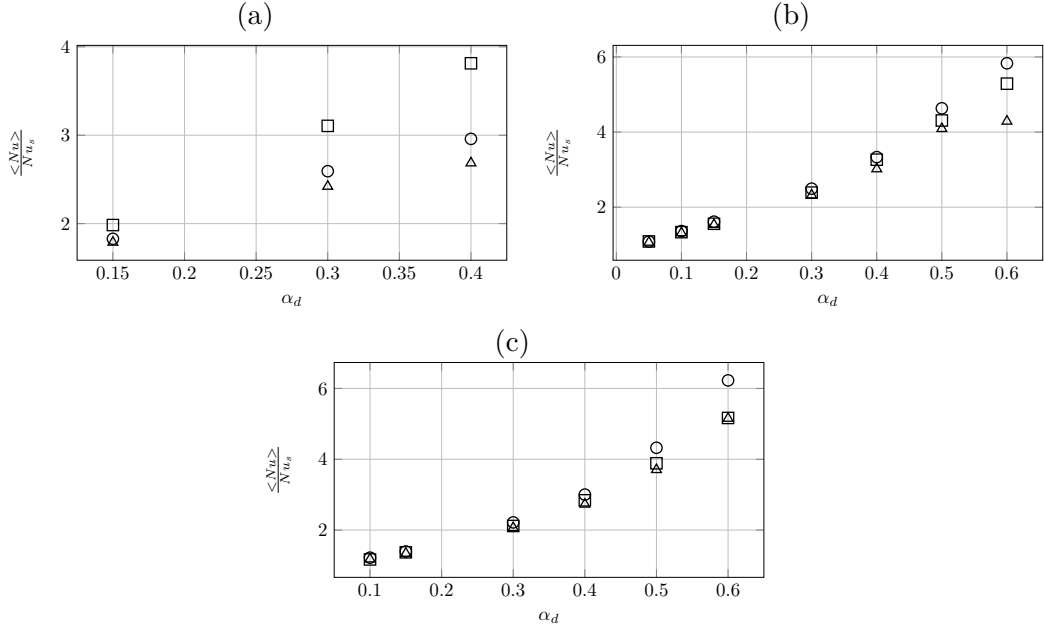


Figure 6.23: Global Nusselt coefficient for a uniform flow past a FCC, normalized by Ranz and Marshall [88] Nusselt coefficient for a uniform flow past an isolated sphere. Evolution as a function of the solid volume fraction α_d at Reynolds numbers (a) $Re = 10$, (b) $Re = 50$, (c) $Re = 100$: (\square) Massol [70], (\circ) present work using Aslam extension and (\triangle) present work using Lagrange extrapolation.

Figure 6.23 shows the normalized Global Nusselt coefficient $\frac{Nu}{Nu_s}$ for a uniform flow past a FCC array of spheres, computed using on one hand Aslam extension and on the other hand Lagrange extrapolation. It also shows $\frac{Nu}{Nu_s}$ extracted from Massol's body fitted simulations [70]. One can observe that Aslam extension improves the heat transfer computation for a packed spheres even if it seems to overestimate it with respect to Massol's results for high solid volume fraction.

Bidisperse Face-Centred Cubic periodic arrangement of spheres

The last case investigated in this work to assess the possible improvement brought when Aslam extension is used for the drag force computation is a bidisperse Face-Centred Cubic periodic arrangement for two species of spheres: the larger particles are distributed in the same configuration as the one previously presented for

monodisperse arrangements while the smaller particles are located at the center of the vertices and at the center of the cubic simulation domain as illustrated in figure 6.24. The parameter to set up this case were fully detailed in [24].

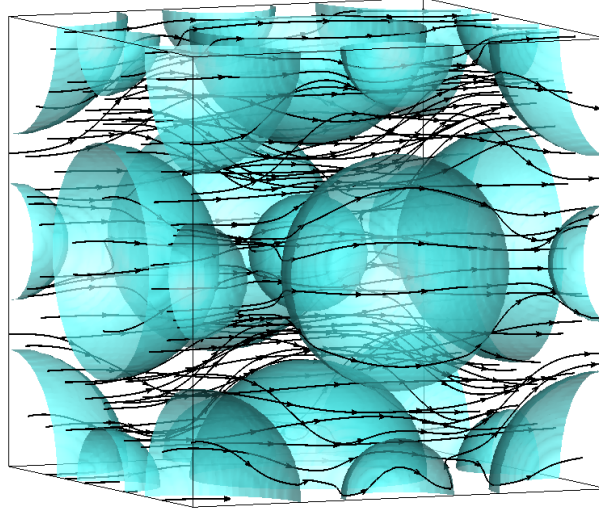


Figure 6.24: FCC/FCC bidisperse arrangement of spheres for $Re = 50$ and $\alpha_d = 0.3$ - the particle shape is plotted in blue and the black lines are the streamlines.

The two species are characterized by the following dimensionless parameters:

$$x_i = \frac{\alpha_i}{\alpha_d} \quad , \quad y_i = \frac{d_i}{d_s} \quad (6.13)$$

where d_i and α_i are the particle diameter and the solid volume fraction of the specie i respectively. The Sauter mean diameter d_s is given by:

$$d_s = \left[\sum_i \frac{2 x_i}{d_i} \right]^{-1}$$

Figure 6.25 shows the non-dimensional drag force F for a uniform flow past a FCC/FCC packed spheres computed using Aslam extension as well as the one computed using Lagrange extrapolation [24]. Those results are compared to the body fitted Massol drag force taken as a reference results. It can be observed that drag forces computed using Aslam extension are closer to Massol's results than those computed using Lagrange extrapolation, and that for both species y_1 and y_2 at $Re = 50, 100$.

6.5 Conclusions

An original method has been designed for estimating forces and heat transfer in Particle-resolved Direct Numerical Simulations. It is based on Aslam extension

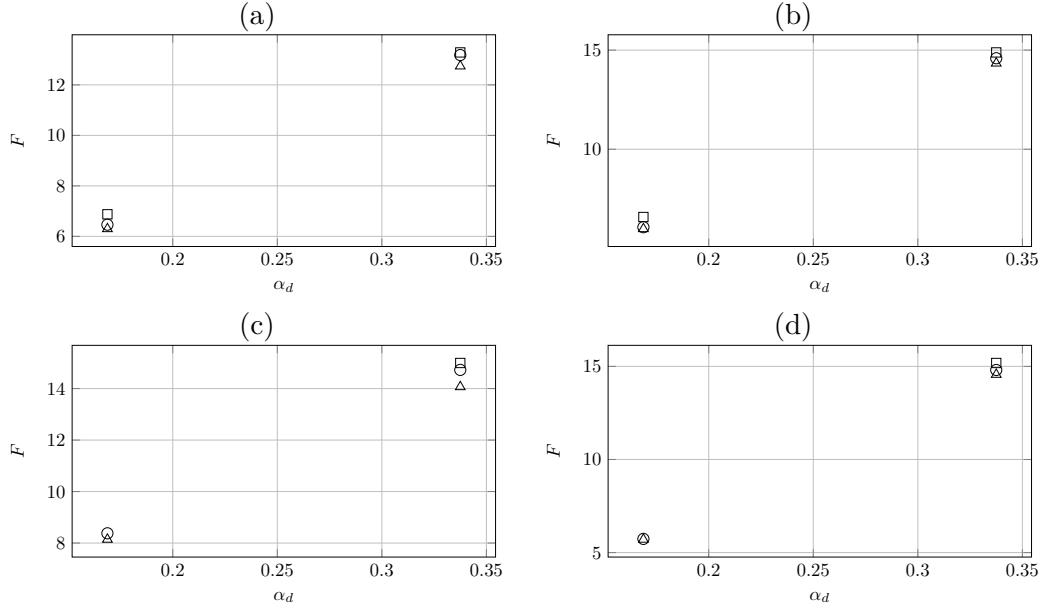


Figure 6.25: Non-dimensional drag force F for a uniform flow past a FCC/FCC packed spheres as function of the solid volume fraction α_d (a) : ($Re = 50, y1$), (b) : ($Re = 50, y2$), (c) : ($Re = 100, y1$), (d) : ($Re = 100, y2$), : (□) Massol [70], (○) present work using Aslam extension and (△) present work using Lagrange extrapolation.

coupled with Taylor interpolation both of third order. This method was first validated without flow resolution for various particle shapes (spherical, ellipsoidal and cubical particles) and a numerical study has been conducted in both two- and three-dimensions. The expected convergence orders were obtained for spherical and ellipsoidal particles. This method is constructed to be a better alternative to the approach proposed for drag force and heat transfer estimates published in [24] and [23] respectively. This improvement was shown by comparing the results of both techniques applied to multiple test cases. First, in a uniform flow past an isolated hot sphere, Aslam extension use reduces significantly the extrapolation distance. It also correct some inaccurate local pressure values on the sphere. The Aslam extension effect on the drag and Nusselt coefficients was more significant in more complex flows as mono- and bi-disperse Faced-Centered Cubic arrangement of spheres.

The general conclusion that we have obtained is that drag force and heat transfer calculation using Aslam extensions fits to body fitted simulations of Massol *et al.* [70] better than the computation using Lagrange extrapolations.

Future works will be devoted to applying our hydrodynamic force and heat transfer calculation method to random arrangements of spherical and ellipsoidal particles and extracting correlation laws for these configurations.

Chapter 7

Conclusions and perspectives

Multiphase flows are plentifully met in both natural and industrial process. Therefore studying them in order to accurately predict their behaviour is crucial. The CFD simulations of these applications are based on statistical approaches, where the fluid-solid interactions (hydrodynamic forces, heat transfers ...) appears as unclosed terms. Particle-Resolved Direct Numerical Simulations (PR-DNS) is often utilized to model these terms. This work aims at providing a reliable tool for investigating and ultimately model the particle-fluid interactions in the framework of finite-size particle motions.

Improvement of Viscous Penalty Method [109], used in this work to perform PR-DNS, has been proposed and extensive numerical study of its most important parameters has been conducted: the viscosity ratio between the fluid and the penalty viscosity μ_s inside the particle, the augmented Lagrangian parameter r , the viscous law used to defined μ in the cells cut by the fluid/solid interface, the solid fraction estimate C_μ at the viscous nodes and the numerical radius of the particle. The best set of these parameters has been established in order to obtain lower errors as possible when the simulations are compared to the analytical solution for the Stokes flow around a cylinder. For the first time, we have been able to demonstrate that if C_μ is directly calculated by projecting the real shape of the particle on the viscous nodes, the numerical radius of the particle does not have to be adapted compared to its real physical value. A convergence study was conducted with respect to mesh refinement. An order of 1.67 was obtained for all velocities inside the fluid. It is worth noting that the major part of the error is concentrated in the Eulerian cells cut by the fluid-solid interface because the equivalent fluid properties are not physical (they are an average of those of fluid and solid in the cell).

Moreover, simulations of uniform flow past a square arrangement of cylinders at larger particle Reynolds number have been carried out in order to assess this new set of VPM parameters abroad the Stokes regime. comparisons of these simulations results with reference correlations of Ergun allowed us to demonstrate that for various solid fractions ranging from 0.2 to 0.6, the simulations were in very good agreement with the expected values.

After having improved the VPM method used to perform PR-DNS simulations,

a new method has been designed for estimating hydrodynamic forces and heat transfer in these finite-size particle simulations. It is based on a third order Lagrange extrapolation coupled with a third order Taylor interpolation, utilized to avoid the inaccurate velocity, pressure and temperature values on the Eulerian cells cut by the interface. Various parameters of the method have been tested and set up through the study of the effect of interpolation and extrapolation orders or the size of the particle surface elements on the error observed on forces and Nusselt numbers. Afterwards, we have simulated various particulate flow motions ranging from incompressible flows around an isolated particle (sphere and ellipsoid) at various Reynolds numbers to flows across packed spheres under Faced-Centered Cubic, random and bi-disperse arrangements. In all configurations, the hydrodynamic forces and the Nusselt numbers have been compared to reference results of the literature for various Reynolds numbers, solid fractions for packed spheres and attack angle for ellipsoids. The general conclusion that we have obtained is that our force and heat transfer calculation method results are in a very good agreement with the reference correlations in the literature and that for obtaining a correct force calculation in finite-size particle simulations, the most important parameter is not the number of Eulerian cells along a particle diameter but the number of mesh cells belonging to the boundary layer surrounding the particle. A new Nusselt correlation has been proposed for an isolated ellipsoid. This work has to be completed and extended to various flow configurations, Reynolds numbers and attack angle in order to generalize the Nusselt correlation.

Although force and heat transfer computation method based on Lagrange extrapolation gave good results in several configurations, the local distribution of pressure coefficient and Nusselt number over the particles computed using this method showed some inaccurate results. Thus, an original method has been designed for estimating forces and heat transfer in Particle-resolved Direct Numerical Simulations in order to prevent these errors. This new approach is based on third order Aslam extension rather than Lagrange extrapolation. It is also coupled with a third order Taylor interpolation. The improvements of the local distribution of the pressure coefficient and the local Nusselt number and hence of the hydrodynamic forces and the global Nusselt numbers were highlighted by comparing the results of both approaches in multiple cases.

future work

Following the work of Ozel *et. al.* [77], simulations of liquid–solid fluidized bed will be conducted by applying our force and heat transfer calculation method to better understand the phenomena taking place in the bed and hydrodynamic of a particle with respect to its position in the bed. Obtaining drag, lift or Nusselt correlations in fluidized beds for a moderate Stokes number is still a challenging task for macroscopic models used in industrial codes.

Giving the lack of correlation of an isolated ellipsoid Nusselt number, a more

detailed study of a uniform flow past a spheroid can be conducted for a wider range of Reynolds number, aspect ratio, attack angle and Prandtl number. Thus, a more general correlation of Nusselt number than the one extracted from this work would be proposed.

A campaign of simulations of a random fixed arrangements of ellipsoidal particles could be carried out in order to extract correlation laws for drag, lift and heat transfer.

Ellipsoid motion in the code should be implemented as well as ellipsoids collision in order to study fluid-particle and particle-particle interactions in a fluidized bed of non-spherical particles.

Bibliography

- [1] A. Acrivos, E. J. Hinch, and D. J. Jeffrey. Heat transfer to a slowly moving fluid from a dilute fixed bed of heated spheres. *Journal of Fluid Mechanics*, 101(2):403–421, 1980.
- [2] J. Adanez, A. Abad, F. Garcia-Labiano, P. Gayan, and L. F. de Diego. Progress in Chemical-Looping Combustion and Reforming technologies. *Progress in Energy and Combustion Science*, 38(2):215–282, April 2012.
- [3] H. Ali and S. Rohani. Dynamic modeling and simulation of a riser-type fluid catalytic cracking unit. *Chemical Engineering and Science*, 20:118–130, 1997.
- [4] P. R. Amestoy, I. S. Duff, J. Koster, and J.-Y. L’Excellent. A fully asynchronous multifrontal solver using distributed dynamic scheduling. *SIAM Journal on Matrix Analysis and Applications*, 23(1):15–41, 2001.
- [5] P. R. Amestoy, A. Guermouche, J.-Y. L’Excellent, and S. Pralet. Hybrid scheduling for the parallel solution of linear systems. *Parallel Computing*, 32(2):136–156, 2006.
- [6] Ph. Angot, Ch.-H. Bruneau, and P. Fabrie. A penalization method to take into account obstacles in incompressible viscous flows. *Numerische Mathematik*, 81:497–552, 1999.
- [7] B. Arcen, R. Ouchene, M. Khalij, and A. Tanière. Prolate spheroidal particles’ behavior in a vertical wall-bounded turbulent flow. *Physics of Fluids*, 29(9):093301, sep 2017.
- [8] T. Aslam. A partial differential equation approach to multidimensional extrapolation. *Journal of Computational Physics*, (193):349–355, 2004.
- [9] T. D. Aslam. A partial differential equation approach to multidimensional extrapolation. *Journal of Computational Physics*, 193(1):349–355, jan 2004.
- [10] G.H. Bagheri, C. Bonadonna, I. Manzella, and P. Vonlanthen. On the characterization of size and shape of irregular particles. *Powder Technology*, 270:141–153, jan 2015.
- [11] G. K. Batchelor. *An introduction to fluid dynamics*. Cambridge mathematical library. Cambridge Univ. Press, Cambridge, 1. cambridge mathematical ed., 14. print edition, 1967. OCLC: 838184093.

-
- [12] R. Beetstra, van M. A. der Hoef, and J. A. M. Kuipers. Drag force of intermediate Reynolds number flow past mono- and bidisperse arrays of spheres. *AIChE Journal*, 53(2):489–501, February 2007.
- [13] W. Bizid. *Development of penalty methods for the simulation of turbulent flows around obstacles*. PhD thesis, Bordeaux University, 2017.
- [14] W. Bizid, A. Etcheverlepo, S. Vincent, J.-P. Caltagironeand, D. MONFORT, and M. Hassine. Penalty methods for turbulent flows interacting with obstacles. *Notes On Numerical Fluid Mech. And Multidisciplinary Design*, 125:13–22, 2014.
- [15] D. R. Breach. Slow flow past ellipsoids of revolution. *Journal of Fluid Mechanics*, 10(02):306–314, 1961.
- [16] H. Brenner. The stokes resistance of an arbitrary particle. *Chem. Eng. Sci.*, 18(1):1–25, 1963.
- [17] W.-P. Breugem. A Combined Soft-Sphere Collision for Immersed Boundary Method for Resolved Simulations of Particulate Flows. In *Proceedings of the ASME 2010 3rd Joint US-European Fluids Engineering Summer Meeting and*, Montréal, 2010.
- [18] W. P. Breugem. A second-order accurate immersed boundary method for fully resolved simulations of particle-laden flows. *Journal of Computational Physics*, 231:4469–4498, 2012.
- [19] J.-P. Caltagirone. *Physics of continuous flows*. Springer Verlag, Berlin Heidelberg, 2013.
- [20] J.-P. Caltagirone and S. Vincent. Tensorial penalisation method for solving Navier–Stokes equations. *Comptes Rendus de l’Académie des Sciences Paris, Série Iib*, 329:607–613, 2001.
- [21] J.-P. Caltagirone and S. Vincent. Tensorial penalty method for solving navier-stokes equations. *Comptes Rendus de l’Académie des Sciences Série II b Mécanique*, (329):607–613, 2001.
- [22] C. S. Campbell and C. E. Brennen. Computer simulation of granular shear flows. *Journal of Fluid Mechanics*, 151:167–188, 1985.
- [23] M.-A. Chadil, S. Vincent, and J.-L. Estivalezes. Accurate calculation of heat transfer coefficients for motions around particles with a finite-size particle approach. In *5th Turbulence and Interactions TI 2018 conference, to be submitted in Notes in Numerical Fluid Mechanics and Multidisciplinary Design*, Springer, Les Trois-Ilets, French West Indies, France, 2018.
- [24] M.-A. Chadil, S. Vincent, and J.-L. Estivalezes. Accurate estimate of drag forces usingparticle-resolved direct numerical simulations. *Accepted in Acta Mechanica*, 2018.

- [25] M.-A. Chadil, S. Vincent, and J.-L. Estivalezes. Drag, lift and Nusselt coefficients for ellipsoidal particles using particle-resolved direct numerical simulations. In *5th Turbulence and Interactions TI 2018 conference, to be submitted in Notes in Numerical Fluid Mechanics and Multidisciplinary Design*, Springer, Les Trois-Ilets, French West Indies, France, 2018.
- [26] M.-A. Chadil, S. Vincent, and J.-L. Estivalezes. Improvement of the viscous penalty method for particle-resolved simulations. *Accepted in Open Journal of Fluid Dynamics*, 2018.
- [27] M.-A. Chadil, S. Vincent, and J.-L. Estivalezes. Novel method to compute drag force and heat transfer for motions around spheres. *Submitted in Thermodynamics of Interfaces and Fluid Mechanics*, 2018.
- [28] R. Chhabra, L. Agarwal, and N. K. Sinha. Drag on non-spherical particles: an evaluation of available methods. *Powder Technol*, 101:288–295, 1999.
- [29] S.H. Cho, H.G. Choi, and J.Y. Yoo. Direct numerical simulation of fluid flow laden with many particles. *International Journal of Multiphase Flow*, 31:435–451, 2005.
- [30] B. P. Le Clair, A. E. Hamielec, and H. R. Pruppacher. A numerical study of the drag on a sphere at low and intermediate reynolds numbers. *Journal of the Atmospheric Sciences*, 27(2):308–315, 1970.
- [31] R. Clift, J.R. Grace, and M.E. Weber. *Bubbles, Drops, and Particles*. Academic Press, 1978.
- [32] H. Darcy. *Les fontaines publiques de la ville de Dijon*. Dalmont, Paris, 1856.
- [33] S. Dartevelle. From model conception to verification and validation, a global approach to multiphase navier-stokes models with an emphasis on volcanic explosive phenomenology. Technical Report LA-14346, 948564, oct 2007.
- [34] J. C. Brändle de Motta, W.P. Breugem, B. Gazanion, J.-L. Estivalezes, S. Vincent, and E. Climent. Numerical modelling of finite-size particle collisions in a viscous fluid. *Physics of Fluids*, 25:083302, 2013.
- [35] J. C. Brändle de Motta, J.-L. Estivalezes, E. Climent, and S. Vincent. Local dissipation properties and collision dynamics in a sustained homogeneous turbulent suspension composed of finite size particles. *International Journal of Multiphase Flow*, 85:369–379, 2016.
- [36] N. G. Deen, S. H.L. Kriebitzsch, M. A. van der Hoef, and J.A.M. Kuipers. Direct numerical simulation of flow and heat transfer in dense fluid–particle systems. *Chemical Engineering Science*, 81:329–344, October 2012.
- [37] N. G. Deen, E. A. J. F. Peters, J. T. Padding, and J. A. M. Kuipers. Review of direct numerical simulation of fluid-particle mass, momentum and heat transfer in dense gas-solid flows. *Chemical Engineering Science*, 116:710–724, September 2014.

- [38] S. C. R. Dennis and J. D. A. Walker. Calculation of the steady flow past a sphere at low and moderate reynolds numbers. *Journal of Fluid Mechanics*, 48(4):771–789, 1971.
- [39] H. Van der Vost. Bi-CGSTAB: a fast and smoothly converging variant of Bi-CG for the solution of non-symmetric systems. *SIAM Journal of Scientific Computing*, 33:631–644, 1992.
- [40] C. Dobrzynski and P. Frey. Anisotropic Delaunay Mesh Adaptation for Unsteady Simulations . In *Proceedings of the 17th International Meshing Roundtable*, 2008.
- [41] David Eberly. Quaternion algebra and calculus. Technical report, 1999.
- [42] S. Ergun. Fluid flow through packed columns. *Chemical Engineering Progress*, (48):89–94, 1952.
- [43] Z.-G. Feng and E. E. Michaelides. A numerical study on the transient heat transfer from a sphere at high Reynolds and Peclet numbers. *International Journal of Heat and Mass Transfer*, 43(2):219–229, 2000.
- [44] P. Forchheimer. Wasserbewegung durch boden. *Z. Ver. Deutsch. Ing.*, (45):1782–1788, 1901.
- [45] M. Fortin and R. Glowinski. *Méthodes de lagrangien augmenté. Application à la résolution numérique de problèmes aux limites*. Dunod, Paris, 1982.
- [46] A. Gobin, H. Neau, O. Simonin, J.-R. Llinas, V. Reiling, and J.-L. Sélo. Fluid dynamic numerical simulation of a gas phase polymerization reactor. *International Journal for Numerical Methods in Fluids*, 43(10-11):1199–1220, 2003.
- [47] D.J. Gunn. Transfer of heat or mass to particles in fixed and fluidized beds. *International Journal of Heat and Mass Transfer*, 21(4):467 – 476, 1978.
- [48] I. Gustafsson. *On first- and second-order symmetric factorisation methods for the solution of elliptic difference equations*. Chalmers University of Technology, 1978.
- [49] W.R Hamilton. On quaternions, or on a new system of imaginaries in algebra. *Lond. Edinburgh Dublin Philos. Mag. J. Sci.*, pages 1–306, 1844.
- [50] L. He, D. K. Tafti, and K. Nagendra. Evaluation of drag correlations using particle resolved simulations of spheres and ellipsoids in assembly. *Powder Technology*, 313:332–343, May 2017.
- [51] R. J. Hill, D. L. Koch, and A. J. C. Ladd. Moderate-Reynolds-number flows in ordered and random arrays of spheres. *Journal of Fluid Mechanics*, 448:243–278, December 2001.

- [52] D. Hoag. Apollo Guidance and Navigation : Considerations of Apollo IMU Gimbal Lock. Technical Report E-1344, MIT Instrumentation Laboratory, April 1963.
- [53] M. A. Van Der Hoef, R. Beetstra, and J. A. M. Kuipers. Lattice-Boltzmann simulations of low-Reynolds-number flow past mono- and bidisperse arrays of spheres: results for the permeability and drag force. *Journal of Fluid Mechanics*, 528:233–254, April 2005.
- [54] A. Hölzer and M. Sommerfeld. Lattice boltzmann simulations to determine forces acting on non-spherical particles. *Fluid Mechanics and its Applications*, 81:99–108, 2006.
- [55] A. Hölzer and M. Sommerfeld. New simple correlation formula for the drag coefficient of non-spherical particles. *Powder Technol*, 184:361–365, 2008.
- [56] H. H. Hu, D. D. Joseph, and M. J. Crochet. Direct Simulation of Fluid Particle Motions. *Theoretical and Computational Fluid Mechanics*, 3:285–306, 1992.
- [57] H. H. Hu, N. A. Patankar, and M. Y. Zhu. Direct Numerical Simulations of Fluid-Solid Systems Using the Arbitrary Lagrangian-Eulerian Technique. *Journal of Computational Physics*, 169:427–462, 2001.
- [58] B. Jeffery. The motion of ellipsoidal particles immersed in a viscous fluid. *Proc. R. Soc. London Ser. A*, 102:161–179, 1922.
- [59] I. Kataoka. Local instant formulation of two-phase flow. *International Journal of Multiphase Flow*, 12:745–758, 1986.
- [60] K. Khadra, Ph. Angot, S. Parneix, and J.P. Caltagirone. Fictitious domain approach for numerical modelling of Navier-Stokes equations. *International Journal for Numerical Methods in Fluids*, 34:651–684, 2000.
- [61] N. Kishore and S. Gu. Momentum and heat transfer phenomena of spheroid particles at moderate Reynolds and Prandtl numbers. *International Journal of Heat and Mass Transfer*, 54(11–12):2595–2601, May 2011.
- [62] S. Krishnan, E. S. G. Shaqfeh, and G. Iaccarino. Fully resolved viscoelastic particulate simulations using unstructured grids. *Journal of Computational Physics*, 338:313–338, 2017.
- [63] D. Lacanette, S. Vincent, A. Sarthou, P. Malaurent, and J.-P. Caltagirone. An eulerian/lagrangian method for the numerical simulation of incompressible convection flows interacting with complex obstacles: Application to the natural convection in the lascaux cave. *International Journal of Heat and Mass Transfer*, 52:2528–2542, 2009.
- [64] A. J. C. Ladd. Numerical simulations of particulate suspensions via a discretized Boltzmann equation. Part 1. Theoretical foundation. *Journal of Fluid Mechanics*, 271:285, July 1994.

- [65] A. J. C. Ladd. Numerical simulations of particulate suspensions via a discretized Boltzmann equation. Part 2. Numerical results. *Journal of Fluid Mechanics*, 271:311, July 1994.
- [66] Z. Li and M.-C. Lai. The Immersed Interface Method for the Navier–Stokes Equations with Singular Forces. *Journal of Computational Physics*, 171(2):822–842, August 2001.
- [67] A. Lyngfelt, B. Leckner, and T. Mattisson. A fluidized-bed combustion process with inherent CO₂ separation; application of chemical-looping combustion. *Chemical Engineering Science*, page 13, 2001.
- [68] J. Magnaudet, M. Rivero, and J. Fabre. Accelerated flows past a rigid sphere or a spherical bubble. Part 1. Steady straining flow. *Journal of Fluid Mechanics*, 284(-1):97, February 1995.
- [69] C. Marchioli, M. Fantoni, and A. Soldati. Orientation, distribution, and deposition of elongated, inertial fibers in turbulent channel flow. *Physics of fluids*, 22:033301, 2010.
- [70] A. Massol. *Simulations numériques d'écoulements à travers des réseaux fixes de sphères monodisperses et bidisperses, pour des nombres de Reynolds modérés*. PhD thesis, 2004.
- [71] T. Mattisson, M. Keller, C. Linderholm, P. Moldenhauer, M. Rydan, H. Leion, and A. Lyngfelt. Chemical-looping technologies using circulating fluidized bed systems: Status of development. *Fuel Processing Technology*, 172:1–12, apr 2018.
- [72] B. Maury. Direct simulations of 2D fluid-particle flows in bi-periodic domains. *Journal of Computational Physics*, 156:325–351, 1999.
- [73] M. Mehrabadi, S. Tenneti, and S. Subramaniam. Importance of the fluid-particle drag model in predicting segregation in bidisperse gas-solid flow. *International Journal of Multiphase Flow*, 86:99–114, November 2016.
- [74] J. C. Brändle De Motta, S. Vincent, J.-L. Estivalezes, and E. Climent. Fictitious Domain Methods and Penalty Techniques for the Simulation of Turbulent Particulate Flows. *ASME Fluid Summer Meeting, Montreal, August 4-7*, 2010.
- [75] Oberbeck. Ueber stationäre flüssigkeitsbewegungen mit berücksichtigung der inneren reibung. 1876.
- [76] R. Ouchene, M. Khaliq, B. Arcen, and A. Tanière. A new set of correlations of drag, lift and torque coefficients for non-spherical particles and large Reynolds numbers. *Powder Technology*, 303:33–43, dec 2016.

- [77] A. Ozel, J.C. Brändle de Motta, M. Abbas, P. Fede, O. Masbernat, S. Vincent, J.-L. Estivalezes, and O. Simonin. Particle resolved direct numerical simulation of a liquid-solid fluidized bed: Comparison with experimental data. *International Journal of Multiphase Flow*, 89:228–240, 2017.
- [78] R. Glowinski T. W. Pan, T. I. Hesla, D.D. Joseph, and J. Périaux. A fictitious domain approach to the direct numerical simulation of incompressible viscous flow past moving rigid bodies: application to particulate flow. *Journal of Computational Physics*, 169:363–426, 2001.
- [79] T. W. Pan, D.D. Joseph, R. Bai, R. Glowinski, and V. Sarin. Fluidization of 1204 spheres: simulation and experiment. *Journal of Fluid Mechanics*, 451:169–191, 2002.
- [80] C. Peskin. The immersed boundary method. *Acta Numerica*, 11:1–39, 2002.
- [81] R. Pfeffer and J. Happel. An analytical study of heat and mass transfer in multiparticle systems at low reynolds numbers. *AIChE Journal*, 10(5):605–611, sep 1964.
- [82] S. B. Pope. Algorithms for ellipsoids. *Cornell University Report No. FDA*, pages 08–01, 2008.
- [83] A. Prosperetti and H.N. Oguz. Physalis: A New $o(N)$ Method for the Numerical Simulation of Disperse Systems: Potential Flow of Spheres. *Journal of Computational Physics*, 167(1):196–216, February 2001.
- [84] T. N. Randrianarivelo. *Etude numérique des interactions hydrodynamiques fluides/solides : application aux lits fluidisés*. PhD thesis, Université Bordeaux 1, 2005.
- [85] T. N. Randrianarivelo, S. Vincent, O. Simonin, and J.-P. Caltagirone. A DNS approach dedicated to the analysis of fluidized beds. *Fluid Mechanics Applications*, 81:207–214, 2007.
- [86] T.N. Randrianarivelo, G. Pianet, S. Vincent, and J.-P. Caltagirone. Numerical modelling of solid particle motion using a new penalty method. *International Journal for Numerical MEhods in Fluids*, (47):1245–1251, 2005.
- [87] T.N. Randrianarivelo, G. Pianet, S. Vincent, and J.-P. Caltagirone. Numerical modelling of the solid particle motion using a new penalty method. *International Journal for Numerical Methods in Fluids*, 47:1245–1251, 2005.
- [88] W. E. Ranz and W. R. Marshall. Evaporation from drops. Parts I & II. *Chem. Eng. Progr.*, pages 48:141–6; 173–80, 1952.
- [89] A. Richter and P. A. Nikrityuk. Drag forces and heat transfer coefficients for spherical, cuboidal and ellipsoidal particles in cross flow at sub-critical Reynolds numbers. *International Journal of Heat and Mass Transfer*, 55(4):1343–1354, January 2012.

-
- [90] A. Richter and P. A. Nikrityuk. New correlations for heat and fluid flow past ellipsoidal and cubic particles at different angles of attack. *Powder Technology*, 249:463–474, November 2013.
- [91] J.-B. Ritz and J.P. Caltagirone. A numerical continuous model for the hydrodynamics of fluid particle systems. *International Journal for Numerical Methods in Fluids*, 30:1067–1090, 1999.
- [92] S. K. P. Sanjeevi, J.A.M. Kuipers, and J. T. Padding. Drag, lift and torque correlations for non-spherical particles from Stokes limit to high Reynolds numbers. *International Journal of Multiphase Flow*, May 2018.
- [93] S. K. P. Sanjeevi and J. T. Padding. On the orientational dependence of drag experienced by spheroids. *Journal of Fluid Mechanics*, 820, jun 2017.
- [94] A. Sarthou, S. Vincent, P. Angot, J.-P. Caltagirone, and others. The sub-mesh penalty method. *Finite Volumes for Complex Applications V*, 2009.
- [95] A. Sarthou, S. Vincent, and J.-P. Caltagirone. A second-order curvilinear to cartesian transformation of immersed interfaces and boundaries. application to fictitious domains and multiphase flows. *Computers and Fluids*, 46:422–428, 2014.
- [96] V.K. Saulev. On the solution of some boundary value problems on high performance computers by fictitious domain method. *Siberian Mathematical Journal*, 4:912–925, 1963.
- [97] L. Schiller and A. Z. Naumann. Über die grundlegenden Berechnungen bei der Schwerkraftaufbereitung. *Ver. Deut. Ing.*, 77:318–320, 1933.
- [98] T. Schönfeld and M. Rudgyard. Steady and Unsteady Flow Simulations Using the Hybrid Flow Solver AVBP. *AIAA Journal*, 37(11):1378–1385, November 1999.
- [99] B. Sun, S. Tenneti, and S. Subramaniam. Modeling average gas–solid heat transfer using particle-resolved direct numerical simulation. *International Journal of Heat and Mass Transfer*, 86:898–913, July 2015.
- [100] P. K. Sweby. High Resolution Schemes Using Flux Limiters for Hyperbolic Conservation Laws. *SIAM Journal on Numerical Analysis*, 21(5):995–1011, October 1984.
- [101] S. Takagi, H.N. Oguz, Z. Zhang, and A. Prosperetti. Physalis: a new method for particle simulation. *Journal of Computational Physics*, 187(2):371–390, May 2003.
- [102] H. Tavassoli, S.H.L. Kriebitzsch, M.A. van der Hoef, E.A.J.F. Peters, and J.A.M. Kuipers. Direct numerical simulation of particulate flow with heat transfer. *International Journal of Multiphase Flow*, 57:29–37, dec 2013.

- [103] S. Tenneti, R. Garg, and S. Subramaniam. Drag law for monodisperse gas-solid systems using particle-resolved direct numerical simulation of flow past fixed assemblies of spheres. *International Journal of Multiphase Flow*, 37(9):1072–1092, November 2011.
- [104] S. Tenneti, B. Sun, R. Garg, and S. Subramaniam. Role of fluid heating in dense gas-solid flow as revealed by particle-resolved direct numerical simulation. *International Journal of Heat and Mass Transfer*, 58(1-2):471–479, mar 2013.
- [105] M. Uhlmann. An immersed boundary method with direct forcing for the simulation of particulate flows. *Journal of Computational Physics*, 209(2):448–476, 2005.
- [106] M. Uhlmann. Interface-resolved direct numerical simulation of vertical particulate channel flow in the turbulent regime. *Physics of Fluids*, 20(5):053305, 2008.
- [107] H. G. Venkates. Motion of a Viscous Liquid Past an Ellipsoid. *Physics of Fluids*, 4(1):33, 1961.
- [108] S. Vincent, J.-P. Caltagirone, P. Lubin, and N. Randrianarivelo. An adaptive augmented Lagrangian method for three-dimensional multi-material flows. *Computers and Fluids*, 33:1273–1289, 2004.
- [109] S. Vincent, J. C. Brändle de Motta, A. Sarthou, J.-L. Estivalezes, O. Simonin, and E. Climent. A lagrangian vof tensorial penalty method for the dns of resolved particle-laden flows. *Journal of Computational Physics*, 256:582–614, 2014.
- [110] S. Vincent, T. Randrianarivelo, G. Pianet, and J.P. Caltagirone. Local penalty methods for flows interacting with moving solids at high Reynolds numbers. *Computers and Fluids*, 36:902–913, 2007.
- [111] S. Vincent, A. Sarthou, J.-P. Caltagirone, F. Sonilhac, P. Février, C. Mignot, and G. Pianet. Augmented Lagrangian and penalty methods for the simulation of two-phase flows interacting with moving solids. Application to hydroplaning flows interacting with real tire tread patterns. *Journal of Computational Physics*, 230:956–983, 2011.
- [112] N. Wakao and S. Kaguei. *Heat and mass transfer in packed beds Volume 1*. Gordon and Breach Science Publishers Inc, 1983.
- [113] Z. Wang, J. Fan, and K. Luo. Combined multi-direct forcing and immersed boundary method for simulating flows with moving particles. *International Journal of Multiphase Flow*, 34(3):283–302, 2008.
- [114] C.-Y. Wen and Y. H. Yu. Mechanics of fluidization. *Chemical Engineering Progress Symposium Series*, (62):100–111, 1966.

-
- [115] S. Whitaker. Forced convection heat transfer correlations for flow in pipes, past flat plates, single cylinders, single spheres, and for flow in packed beds and tube bundles. *AIChE Journal*, 18(2):361–371, 1972.
- [116] M. Zastawny, G. Mallouppas, F. Zhao, and B. van Wachem. Derivation of drag and lift force and torque coefficients for non-spherical particles in flows. *International journal of Multiphase Flow*, (39):227–239, 2012.
- [117] Y. Zhang, Z. Chao, and H. A. Jakobsen. Modelling and simulation of chemical looping combustion process in a double loop circulating fluidized bed reactor. *Chemical Engineering Journal*, 320:271–282, 2017.
- [118] Z. Zhang and A. Prosperetti. A second-order method for three-dimensional particle simulation. *Journal of Computational Physics*, 210:292–324, 2005.

